

## NEW INFRARED SPECTRAL INDICES OF LUMINOUS COLD STARS: FROM EARLY K TO M-TYPES.

MARIA MESSINEO<sup>1</sup>, DONALD F. FIGER<sup>2</sup>, ROLF-PETER KUDRITZKI<sup>3</sup>,  
QINGFENG ZHU<sup>1</sup>, KARL M. MENTEN<sup>4</sup>, VALENTIN D. IVANOV<sup>5</sup>, C.-H. ROSIE CHEN<sup>4</sup>

Draft version July 9, 2021

### ABSTRACT

We present infrared spectral indices (1.0-2.3  $\mu\text{m}$ ) of Galactic late-type giants and red supergiants (RSGs). We used existing and new spectra obtained at resolution power  $R=2000$  with SpeX on the IRTF telescope. While a large CO equivalent width (EW), at 2.29  $\mu\text{m}$  ( $[\text{CO}, 2.29] \geq 45 \text{ \AA}$ ) is a typical signature of RSGs later than spectral type M0,  $[\text{CO}]$  of K-type RSGs and giants are similar. In the  $[\text{CO}, 2.29]$  versus  $[\text{Mg I}, 1.71]$  diagram, RSGs of all spectral types can be distinguished from red giants, because the Mg I line weakens with increasing temperature and decreasing gravity. We find several lines that vary with luminosity, but not temperature: Si I (1.59  $\mu\text{m}$ ), Sr (1.033  $\mu\text{m}$ ), Fe+Cr+Si+CN (1.16  $\mu\text{m}$ ), Fe+Ti (1.185  $\mu\text{m}$ ), Fe+Ti (1.196  $\mu\text{m}$ ), Ti+Ca (1.28  $\mu\text{m}$ ), and Mn (1.29  $\mu\text{m}$ ). Good markers of CN enhancement are the Fe+Si+CN line at 1.087  $\mu\text{m}$  and CN line at 1.093  $\mu\text{m}$ . Using these lines, at the resolution of SpeX, it is possible to separate RSGs and giants. Contaminant O-rich Mira and S-type AGBs are recognized by strong molecular features due to water vapor features, TiO band heads, and/or ZrO absorption. Among the 42 candidate RSGs that we observed, all but one were found to be late-types. 21 have EWs consistent with those of RSGs, 16 with those of O-rich Mira AGBs, and one with an S-type AGB. These infrared results open new, unexplored, potential for searches at low-resolution of RSGs in the highly obscured innermost regions of the Milky Way.

*Keywords:* stars: evolution — infrared: stars — stars: supergiants — stars: massive — stars: abundances

### 1. INTRODUCTION

Stars with initial masses from 8 to 35  $M_{\odot}$  evolve through the red supergiant (RSG) phase (e.g. Chieffi & Limongi 2013).

Stellar evolution models suggest that the upper mass limit for RSGs is 25  $M_{\odot}$  for rotating stars and 40  $M_{\odot}$  for non-rotating stars (e.g., Limongi 2017). Massive stars with luminosities from 10,000 to 400,000  $L_{\odot}$  enter this phase when their envelopes expand and their effective temperatures drop below 4500 K. Because of their intrinsically high luminosity and red colors, they can be seen at large distances and through large columns of dust, making them good tracers of galactic disk morphology and kinematics. The spectra of RSGs are rich in molecular absorptions and atomic lines; for example, Mg, Fe, Al, Si, Ti, Cr, Mn, and Sr lines. These lines may serve to map metallicity in galactic disks at large extragalactic distances (Davies et al. 2017; Lardo et al. 2015), and to constrain the uncertain upper part of the stellar mass function (poorly populated because these stars are short-lived). Detections of Galactic RSGs are hampered by our position in the disk, the patchiness of interstellar extinction, unknown distances, and the difficulty of separating giants from supergiants (e.g. Messineo et al. 2017).

About 500 spectroscopic RSGs are listed in optical catalogs, and 300 in infrared catalogs, see for example, Messineo & Brown (2019), Skiff (2014), Humphreys (1978), Elias et al. (1985), Jura & Kleinmann (1990),

Figier et al. (2006), Davies et al. (2007), Clark et al. (2009), Negueruela et al. (2011).

It appears that we know only about 10% of this important Galactic population. Gehrz (1989) estimated the existence of 5000 RSGs in the Milky Way and this number is well consistent with the numbers of RSGs recently discovered in the M31 (> 6412) and M33 (> 2858) spiral galaxies (Massey et al. 2021).

Improved searches are of primary importance for Galactic studies, The narrow range of ages spanned by RSGs (4-30 Myr) and their youth may help to trace Galactic structure (Massey et al. 2021), as RSGs are useful for tracing the spiral structure, to estimate the star formation rate at the epoch of their formation, and to model the history of Galactic chemical enrichment with their yields.

We are living in a golden age of Galactic astronomy. Gaia is scanning the entire Galaxy, measuring parallaxes, radial velocities, and spectral types for 1.3 billion stars (Gaia Collaboration et al. 2020). Galactic multi-wavelength photometric surveys with sub-arcsec spatial resolution are already available and several high-resolution spectroscopic atlases are expected soon. Park et al. (2018) presented an atlas of  $\approx 80$  spectra covering  $H$ - and  $K$ -bands at  $R=45,000$ , containing dwarfs, giants, and supergiants with spectral types from O to M. More recently, an ESO/Xshooter Atlas of 754 stars at  $R=10,000$  covering 300 nm to 2480 nm has been released by Gonneau et al. (2020). The atlas includes hot and cool stars spanning a wide range of gravity. The ongoing GALAH survey with the HERMES instrument on the Anglo-Australian Telescope will release more than 1 million spectra of Galactic southern stars at  $R=28,000$  in the 4700 to 7600 nm range for chemically tagging the Milky Way (e.g. Sharma et al. 2020). Starting in 2023, 4MOST on the ESO/Vista telescope will release 20 million spectra at  $R \approx 5000$  (from 390 to 1000 nm) and  $R \approx 20,000$  (from 395 to 456.5 nm & from 587 to 673 nm) of southern stars (e.g.,

<sup>1</sup> Key Laboratory for Researches in Galaxies and Cosmology, University of Science and Technology of China, Chinese Academy of Sciences, Hefei, Anhui, 230026, China messineo@ustc.edu.cn

<sup>2</sup> Center for Detectors, Rochester Institute of Technology, 54 Memorial Drive, Rochester, NY 14623, USA

<sup>3</sup> Institute for Astronomy, University of Hawaii, 2680 Woodlawn Drive, Honolulu, HI 96822

<sup>4</sup> Max-Planck-Institut für Radioastronomie, Auf dem Hügel 69, D-53121 Bonn, Germany

<sup>5</sup> European Southern Observatory, Karl Schwarzschild-Strasse 2, D-85748 Garching bei München, Germany

de Jong et al. 2012).

The high-resolution spectra already available have allowed us to better characterize RSG stars with chemical features, abundance and temperature determinations. New spectral modeling identifies bands and lines suitable for parameter determinations. Many recent studies use infrared lines to accurately estimate temperature, gravity, and metallicity (Taniguchi et al. 2020; Park et al. 2018; Patrick et al. 2017; Davies et al. 2017, 2015; Patrick et al. 2015; Lardo et al. 2015; Gazak et al. 2015, 2014b,a). Despite ongoing revision of the temperature scale, based on the TiO molecular bands (Levesque et al. 2005), temperatures can already be inferred with an accuracy of about 150 K. Spectroscopic monitoring for detecting binary RSGs has also been started (e.g. Maíz Apellániz et al. 2019), while Gaia data allow us to identify binary RSGs with proper motion studies (Kervella et al. 2019).

Low-resolution infrared spectroscopy is also important for i) efficiently identifying good targets for high-resolution follow-up, achieved by separating rare RSGs from the bulk of giant stars; ii) estimating parameters; and iii) delineating the morphology of the inner regions of the Galaxy. The first quantitative analysis of infrared spectra was reported by Kleinmann & Hall (1986, *K*-band), Origlia et al. (1993, *H*-band), Blum et al. (1996, *K*-band) and Joyce et al. (1998, *J*-band), with line identifications, index definitions, and relationships between line strengths and stellar physical parameters. These early studies used infrared spectra to estimate luminosity classes and spectral types within a few subtypes. Low resolution spectroscopic libraries have been available since the beginning of this new millennium, e.g. Meyer et al. (1998, *H*-band), Lançon & Wood (2000, 0.5-2.5  $\mu\text{m}$ , at  $R=1100$ ), of Ivanov et al. (*H*- and *K*-bands at  $R \approx 2000-3000$ , 2004). Unfortunately, indices were only sufficient to separate dwarfs from giants/supergiants. The library of cool stars of Rayner et al. (2009) made with SpeX (Rayner et al. 2003) on the NASA InfraRed Telescope Facility (IRTF) covers 0.8 to 2.4  $\mu\text{m}$  at  $R \approx 2000$  with an unprecedented high throughput. The 210 IRTF spectra have extensively been used as an empirical library for building indices useful for simple stellar population models (e.g. Morelli et al. 2020; Cesetti et al. 2013); Davies et al. (2010) analyzed the *J*-band portion of the spectra of RSGs as a metallicity diagnostic. We use the library to confirm the detection of new RSGs, and how to more precisely distinguish them from other Galactic cool stars.

Usually, obscured RSGs are classified by their broad CO band heads at 2.293  $\mu\text{m}$  and by the shape of their stellar continuum. The equivalent width (EW) of the CO bands is an estimator of stellar temperature; however, the EWs of CO of giants and supergiants follow two different relations, with the supergiants spanning a larger range (Blum et al. 2003). Unfortunately, this infrared technique allows us only to identify RSGs with spectral types later than M0.

Infrared spectra from the IRTF library suggest that RSGs and giants occupy different regions in [CO, 2.29] (thereafter we refer to the EW of a specific line by enclosing the element or molecule name and wavelength within brackets) versus [Mg I, 1.71] diagram down to early K-type stars (Messineo et al. 2017). However, only five RSGs of early K-type were available in the IRTF library. In this paper, we report observations with SpeX of known K- and M-type RSGs and candidate RSGs, and use them to define infrared diagnostics for assigning spectral types and luminosity classes. Only

empirical quantities are presented. Quantities to be inferred with a comparison to synthetic spectra, e.g. metallicities, will be presented elsewhere. In Sect. 2, we describe the spectroscopic data, in Sect. 3 the adopted infrared spectral indices. In Sect. 4 we focus on the stellar luminosity of RSGs and infrared indices that correlate with it. In Sect. 5, we describe the [CO, 2.29] versus [Mg I, 1.71] diagram to separate giants and RSGs, while in Sect. 6 we derive temperature estimates from *HK* indices. In Sect. 7 we briefly describe what is known on metallicity of galactic RSGs. A few comments on specific sources are given in Sect. 8. The new targets are spectroscopically classified in Sect. 9. Finally, in Sect. 10, we provide a summary and remarks on the usefulness of these indices as a luminosity diagnostic to identify RSGs from K0 to late M-types and to spectroscopically distinguish them from giants.

## 2. SPECTROSCOPIC INFRARED DATA WITH SPEX

In this work, we present new spectra taken with SpeX of 72 bright late-type stars. To increase the statistical significance, we analyse the new SpeX spectra along with those spectra of bright late-type stars included in the SpeX libraries of Rayner et al. (2009) and Villaume et al. (2017). These two libraries include 24 K-M stars of class I.

### 2.1. New observations and data reduction

Two half-nights of observations with the 3-m IRTF telescope were awarded to this program (number 047) in Period 19A, allocated on 2019 June 23 and 24. We observed for about 2.5h (out of the 9h awarded) due to poor weather. The observational program was continued in Period 20A (number 045, 24 h allocated) from 2020 May 22 to June 25.

We used the upgraded SpeX spectrograph in cross-dispersed mode (SXD; Rayner et al. 2003). The 0'3 slit (the plate scale is 0'1 per pixel) was used, providing a resolving power,  $R$ , of  $\sim 2000$ . The observations covered from 0.7 to 2.55  $\mu\text{m}$ . For comparison, the IRTF library of Rayner et al. (2009) was performed with the pre-upgraded SpeX in SXD mode, having the same resolution ( $R=2000$ ), but slightly smaller wavelength range of 0.80-2.55  $\mu\text{m}$ .

The classical nodding technique was used to obtain a good sky-subtracted frame. Frames were taken in the A and B positions, with the telescope nodding between the two positions from 3 to 10 times (AB cycles). The rotator angle was synchronized to the parallactic angle and the AB distance optimized in order to secure the target in the slit while nodding. For each position, the number of non-destructive reads (NDR) was set to a maximum of 32, and from 1 to 8 coadds were taken with a basic integration time from 0.4 to 90 s. Our targets were bright enough to use as guide stars in the SpeX slit viewer. Flats and arcs were taken during the night, every two to four targets.

Data were processed with the SpeXtool software (Cushing et al. 2004)<sup>6</sup>.

For each pair, the B image was subtracted from the A image, and the resulting image was flat-fielded and checked for non-linearity. Wavelength calibration was performed using arc lamps. Two aperture positions per frame were marked (the positive and the negative), and the corresponding stellar traces defined. Each optimally extracted spectrum was background-subtracted using a constant value from nearby pixels (same width as the aperture). Typically, for each target and each order 10 spectra were extracted and combined.

<sup>6</sup> see the IRTF webpage: [http://irtfweb.ifa.hawaii.edu/~sim\\$speX/observer](http://irtfweb.ifa.hawaii.edu/~sim$speX/observer)



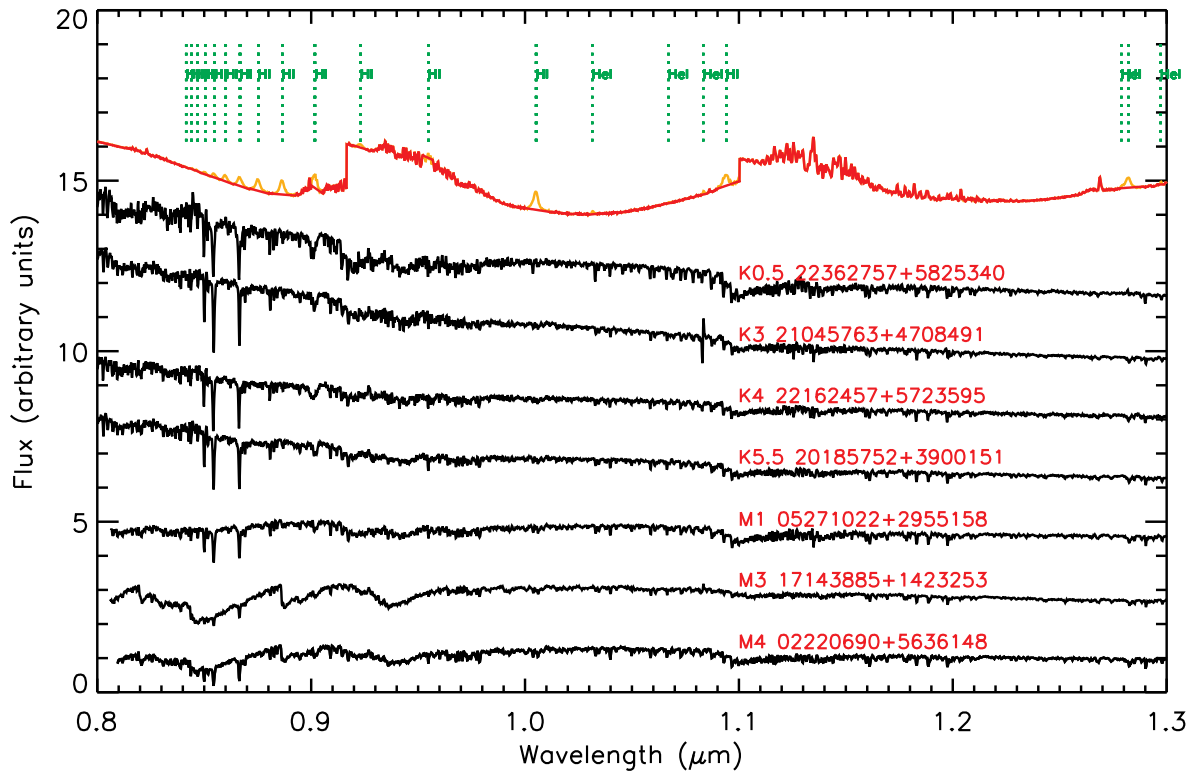


**Figure 1.** Some examples of spectra of RSGs taken with SpeX (in black). Over-plotted in red (clean) and orange (with H and He I lines still not subtracted) is an example of the instrumental response and atmospheric transmission curve. The locations of the *H I* and *He I* lines are marked with the green dotted-vertical lines. The spectra are corrected for reddening and normalized to the mean flux density within the range from 1.1  $\mu\text{m}$  to 1.25  $\mu\text{m}$ . The SpeX spectra of stars in Tables 1, 2, and 3 are displayed in Appendix Fig. C.

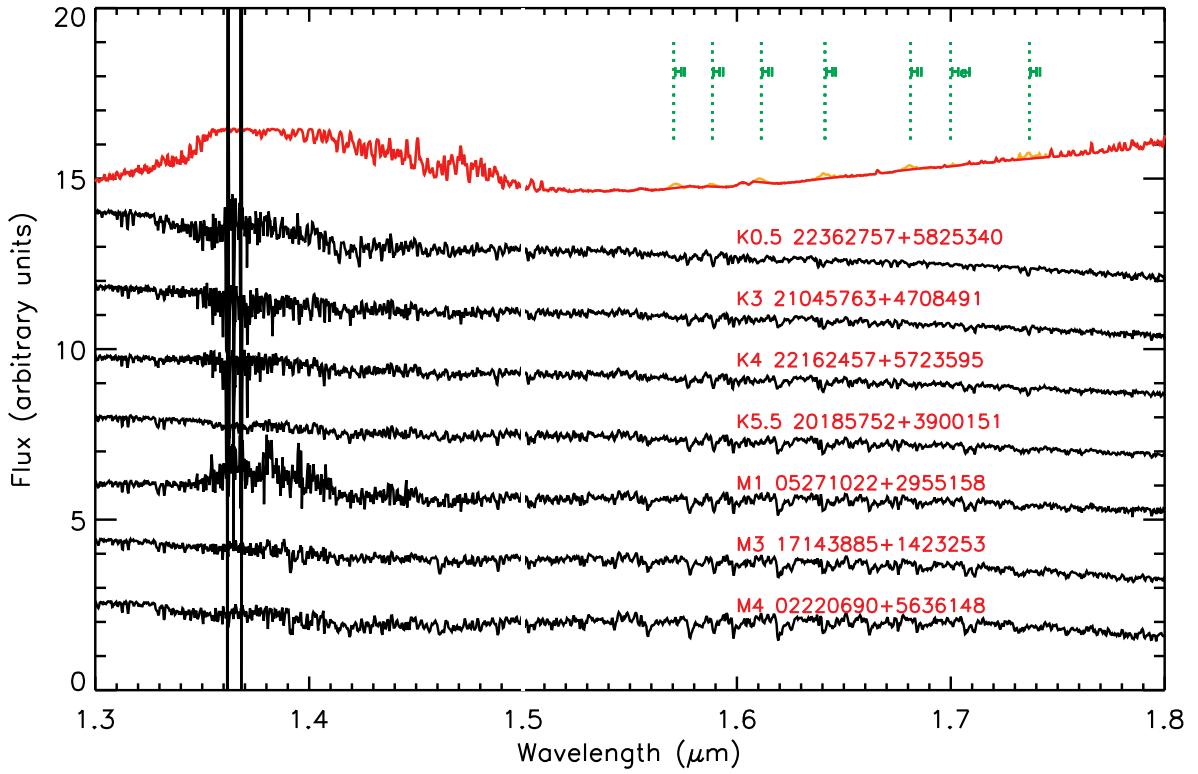


Figure 1. Continuation of Fig. 1. Here, the spectra are normalized to the mean flux density from 1.5  $\mu\text{m}$  to 1.6  $\mu\text{m}$ .

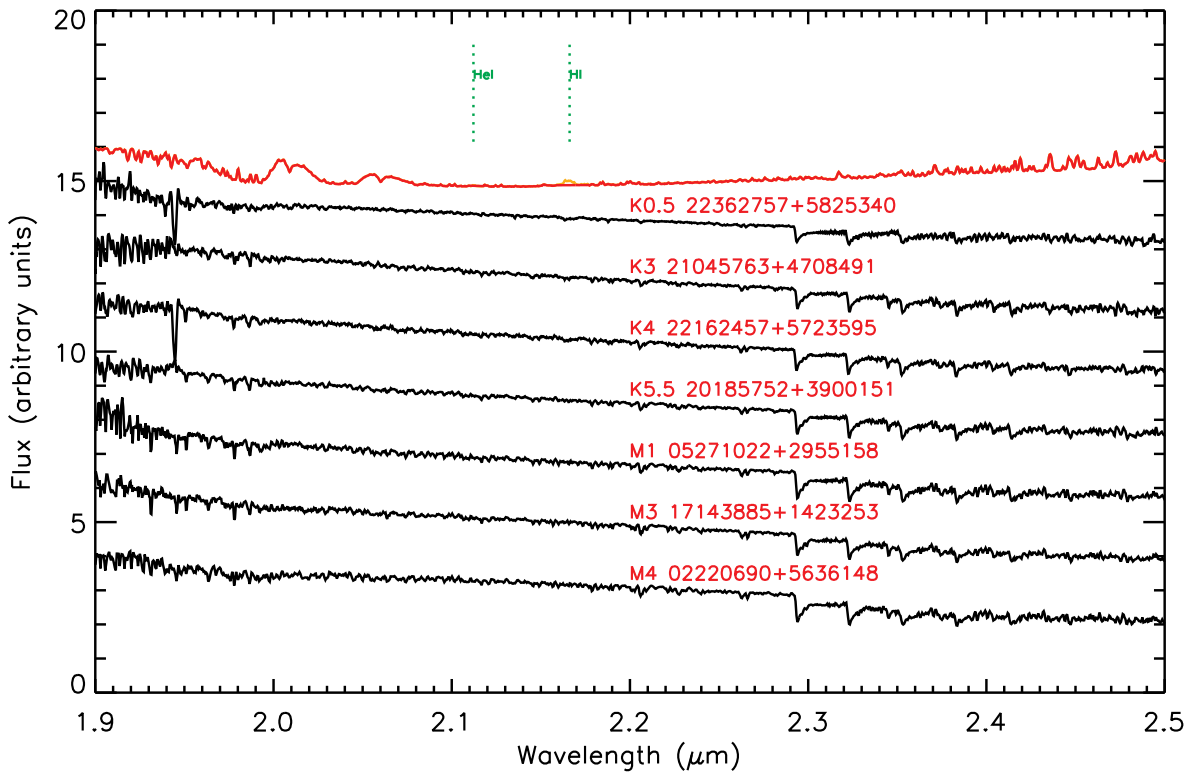


Figure 1. Continuation of Fig. 1. Here, the spectra are normalized to the mean flux density at 2.2-2.25  $\mu\text{m}$ .



Telluric standard stars were selected with B or A0 types and observed at an airmass within 0.2 from that of the target. The H lines were removed with Gaussian fits and linear interpolations. After having removed the H I lines, we inspected the spectra of the early B telluric stars and removed the detected He I lines at 7065.0 Å, 10141.2 Å, 10314.2 Å, 10670.7 Å, 10833.2 Å, 12788.4 Å, 12972.0 Å, 17007.3 Å, and 21123.8 Å. Eventually, to obtain the final instrumental response and atmospheric transmission, the standard spectrum extracted from each order was divided by a normalized black body with temperature as that of the standard star.

The observed spectrum, order by order, was divided by the instrumental response and atmospheric transmission curve. The target and standard spectra were checked for small shifts in wavelength by cross-correlating spectral regions of high atmospheric absorption. The final spectrum was obtained by merging the segments extracted from the various orders. Eventually, the spectra were corrected for interstellar extinction with the  $A_{K_s}$  from Sect. 4.1 and the extinction curve of Messineo et al. (2005) (basically the law of Cardelli et al. (1989) with an infrared power law of index = -1.9).<sup>7</sup>

A few SpeX spectra are shown in Fig. 1. We obtained spectra for 72 objects (one object was observed twice).

Table 1 lists the 21 known RSGs which we observed (marked with the column Library=1) and which are not included in the IRTF library, as well as other known class I stars from the IRTF libraries (marked with the column Library=2 and 3).

Table 2 lists the 42 new candidate RSGs, and Table 3 the 9 known giants (with three of them 2MASS J23300740+4907592/HD 221246, 2MASS J20224530+4101338/HD 194193, 2MASS J13492867+1547523/HD 120477 already listed in the IRTF library).

In Sect. 3 to 7, we analyze the spectral properties of the previously known RSGs. The analysis of the candidate RSGs is presented later in Sect. 9, i.e., after having established a set of appropriate indices for assigning spectral types and classes.

### 2.2. Spectra from the IRTF libraries

The IRTF spectral library of cold stars consists of data taken with the old SpeX instrument, covering from 0.8  $\mu\text{m}$  to 5.0  $\mu\text{m}$  at a resolution  $R=2000$  (Rayner et al. 2009). 22 stars of class I are included in the IRTF library of Rayner et al. (2009) and also listed in our Table 1. They consist of 21 RSGs, plus 2MASS J17143885+1423253/HD 156014 (M5 Ib-II, a likely Asymptotic Giant Branch star, AGB, Moravveji et al. 2013). The number of early K-type I stars included in the library is scarce, with two K0 I stars and three K2 I stars.

A comparison sample of 43 stars of class III from the same library is used in the plots. The sample includes normal giants and AGB stars.

Villaume et al. (2017) have created an extended IRTF spectral library using the new SpeX detector. The library contains 38 cold stars listed as class III and two of class I; 2MASS J06121911+2254305/HD 042543 is an M1-M2 I star and 2MASS J06300229+0755159/HD 045829 is a K2 I star.

<sup>7</sup> We used average colors ( $J-K_s$ )=1.05 mag and ( $H-K_s$ )=0.235 mag to initially correct the spectra for interstellar extinction, corresponding to an initial uncertainty  $\Delta A_{K_s}$  within 0.17 mag. After having measured the EWs and determined the individual spectral types (Sect. 6), we recomputed the  $A_{K_s}$  values (Sect. 4.1). The initial  $\Delta A_{K_s}$  causes fluctuations of 2-3 % in the EWs and 10 K in the stellar temperatures.

### 2.3. Contaminants

The spectra of AGBs can appear similar to those of RSGs, despite their lower initial masses ( $< 8 - 9 M_{\odot}$ ). In the MK system of Keenan & McNeil (1989), AGB stars are reported with classes III, II, Ib, and even Iab, which depends on initial masses and number of thermal pulses (Messineo & Brown 2019; Moravveji et al. 2013). On the basis of their surface abundances, AGBs divide in C-rich ( $C/O > 1$ ), O-rich ( $C/O < 1$ ), and S-types. S-type stars have a mixed chemistry, in most of the cases indicating an intrinsic transition from O- to C-rich of AGB stars with masses from 1 to 5  $M_{\odot}$ ; S-type stars are rich in s-process elements such as Zr (Shetye et al. 2020). At infrared light, spectroscopically, C-rich stars are easily identified by their strong CN and CO bands; O-rich AGBs and S-type stars may be mistaken for RSGs depending on spectral coverage, for example when covering only the *K*-band. Throughout the manuscript, in each of the presented figures, we mark also the distributions of quantities measured in the spectra of O-rich AGB stars and S-type stars from the IRTF library. This allows us to locate a few new diagrams that are useful for quantitative decontamination and that open new direction for theoretical investigations.

## 3. DEFINITIONS OF SPECTRAL INDICES

We determine spectral class using apparent single line profiles in both K- and M- type stars. For *HK*-band indices, we adopt the indices defined by Messineo et al. (2017), Origlia et al. (1993), and Ivanov et al. (2004). For *YJ* bands, we use 25 lines, seven of which are included in the work of Morelli et al. (2020). The adopted lines and continua are displayed in Fig. 2 along with the spectra of a K2 RSG and an M3.5 RSG.

The definitions of the measured spectral indices (line bands, and continua), are given in Table 4.  $EW = \text{bin} \times \sum_j (1 - \frac{F_{\lambda}[j]}{F_{\text{continuum}}[j]})$ , where  $F_{\lambda}$  is the observed flux density in the line region,  $F_{\text{continuum}}$  is the estimated flux density of the continuum in the line region, and bin is the wavelength size of one bin. Continuum estimates are done with a linear interpolation of nearby spectral regions. Generally, the two continuum regions are located on each side of the line, when it is possible. For line J10 (CN head band), the two continua are both at wavelengths shorter than that of the line, so to avoid the continuum depression due to CN absorption. For the Na I line, the two continua are both at wavelengths longer than that of the line to avoid possible continuum depression due to water absorption. For the CO head-band at 2.29  $\mu\text{m}$ , a constant continuum is assumed, as in Messineo et al. (2017) and Figer et al. (2006). Positive values are for absorption lines.

Measurements were performed on spectra corrected for Doppler shift. A linear dispersion in wavelengths was applied. For each star, Doppler shifts were measured in *K*-band and also in *H*-band and applied to the wavelength solution. The differences between the velocities obtained from the *H*-band and *K*-band have a sigma of 7  $\text{km s}^{-1}$ . For 20 stars velocity measurements are available in the Gaia DR2 release, there is a good agreement with our measurements with a sigma of 23  $\text{km s}^{-1}$ . The velocities,  $V_{\text{LSR}}$ , are listed in Table 1.

The following describes the spectral indices, and measurements are in Appendix Table C.

### CO band heads

It is well established that the temperature of late-type stars can be estimated at infrared wavelengths by using the CO

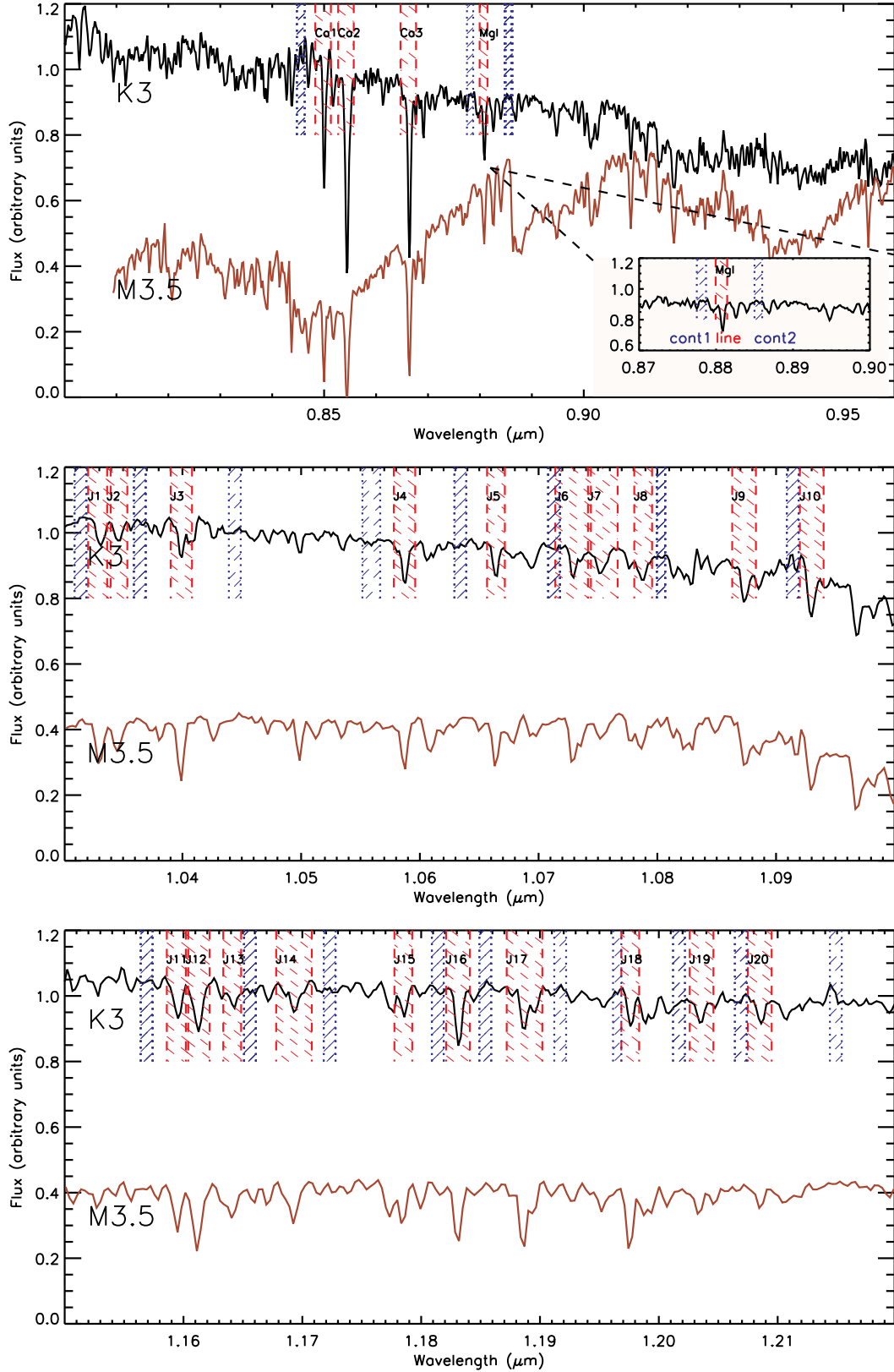


**Figure 2.** Each panel displays a region of the stellar spectrum of 2MASS J19461557+1036475 ( $\gamma$  Aqlilae) (top curve in black), which is a K3 II star in the Morgan & Keenan system (Keenan & McNeil 1989). Below it, in brown the spectrum of 2MASS J02220690+5636148/HD 14469 is shown (M3.5lab, Keenan & McNeil 1989). On the stellar spectrum (top of the figure), red dashed-vertical lines mark the two edges of each index defined in Table 4, while blue dotted lines mark the adjacent continua.



**Table 3**  
List of observed known giants.

| 2MASS-ID         | Library | Sp<br>(adopt) | T <sub>eff</sub> <sup>a</sup><br>[K] | A <sub>Ks</sub><br>[mag] | dist(cl) <sup>aa</sup><br>[kpc] | Ref<br>(cl) | dist(EDR3) <sup>b</sup><br>[kpc]      | V <sub>LSR</sub> <sup>c</sup><br>[km s <sup>-1</sup> ] | dist(Kin) <sup>d</sup><br>[kpc]       | m <sub>bol</sub> <sup>int e</sup><br>[mag] | m <sub>bol</sub> <sup>BC<sub>K</sub>f</sup><br>[mag] | Sp <sup>g</sup> | Ref   | Sp<br>(giant) | Temp<br>(CO)<br>(2.29) | Temp<br>(Ca)<br>(2.26) | Temp<br>(Na)<br>(2.21) | Temp<br>(Mg I)<br>(1.71) | Temp<br>(Si I)<br>(1.64) | Temp<br>(CO)<br>(1.62) | Comments <sup>h</sup> |
|------------------|---------|---------------|--------------------------------------|--------------------------|---------------------------------|-------------|---------------------------------------|--|---------------------------------------|--|--|-----------------|-------|---------------|------------------------|------------------------|------------------------|--------------------------|--------------------------|------------------------|-----------------------|
| 00403044+5632145 | 1       | K1            | 4120.00± 33.00                       | -0.00 ± 0.14             | ..                              | ..          | 0.07 <sup>0.00</sup> <sub>-0.00</sub> | 2.51± 0.02   | ..                                    | ..   | 2.14± 0.23   | K0IIIa          | 2     | K2            | 4216                   | 4141                   | 4101                   | 4185                     | 4034                     | 4159                   |                       |
| 13492867+1547523 | 1       | K4.5          | 3886.00± 38.00                       | -0.05 ± 0.17             | ..                              | ..          | ..                                    | 4.27± 0.19   | ..                                    | ..   | 3.06± 0.26   | K5.5III         | 2     | M2            | 4033                   | 3920                   | 3959                   | 3852                     | 3793                     | 3940                   |                       |
| 15005772+3122384 | 1       | M1.5          | 3726.00± 95.00                       | 0.08 ± 0.16              | ..                              | ..          | 0.89 <sup>0.02</sup> <sub>-0.02</sub> | 2.30± 0.88   | 0.23 <sup>0.06</sup> <sub>-0.06</sub> | 6.05± 0.77                                 | 6.19± 0.26   | M2-4III         | 19,20 | M4            | 3963                   | 3897                   | 3961                   | 3519                     | 3641                     | 3782                   | TiO0.88 ZrO0.93       |
| 15061509+1521575 | 1       | K4.5          | 3884.00± 67.00                       | 0.08 ± 0.01              | ..                              | ..          | 1.23 <sup>0.03</sup> <sub>-0.03</sub> | -80.75± 0.25   | ..                                    | 7.90± 0.76                                 | 8.03± 0.06   | K5III           | 24    | M2            | 4025                   | 3959                   | 4055                   | 3735                     | 3835                     | 3910                   |                       |
| 15062101+2626136 | 1       | K2            | 4035.00± 28.00                       | 0.09 ± 0.02              | ..                              | ..          | 0.38 <sup>0.00</sup> <sub>-0.00</sub> | 18.59± 0.14  | 1.27 <sup>0.01</sup> <sub>-0.01</sub> | 6.89± 0.77                                 | 7.11± 0.07   | K4III           | 22,7  | K4            | 4148                   | 4009                   | 4087                   | 4023                     | 3960                     | 4071                   |                       |
| 16112324+2458016 | 1       | M0            | 3784.00± 68.00                       | 0.01 ± 0.18              | ..                              | ..          | 0.76 <sup>0.01</sup> <sub>-0.01</sub> | -40.39± 0.22   | ..                                    | 6.43± 0.77                                 | 6.53± 0.38   | M1III           | 7     | M2.5          | 4013                   | 3863                   | 3944                   | 3621                     | 3739                     | 3831                   | TiO0.88               |
| 16120838+1432561 | 1       | K3            | 3992.00± 34.00                       | 0.11 ± 0.01              | ..                              | ..          | 0.48 <sup>0.01</sup> <sub>-0.01</sub> | 52.45± 0.14  | 3.23 <sup>0.01</sup> <sub>-0.01</sub> | 7.16± 0.77                                 | 7.35± 0.06   | K4III           | 25    | K5.5          | 4112                   | 3988                   | 4069                   | 3946                     | 3923                     | 4031                   |                       |
| 20224530+4101338 | 1       | K4.5          | 3897.00± 20.00                       | 0.15 ± 0.19              | ..                              | ..          | 0.30 <sup>0.00</sup> <sub>-0.00</sub> | 19.67± 0.19  | 1.61 <sup>0.41</sup> <sub>-0.41</sub> | 4.31± 0.79                                 | 4.43± 0.33   | K7III           | 2     | M0.5          | 4076                   | 3856                   | 3920                   | 3835                     | 3917                     | 3915                   | CN                    |
| 23300740+4907592 | 1       | K2.5          | 4018.00± 14.00                       | 0.19 ± 0.23              | ..                              | ..          | 0.31 <sup>0.00</sup> <sub>-0.00</sub> | 1.20± 0.20   | ..                                    | 5.07± 0.80                                 | 5.28± 0.41   | K3III           | 2     | K4.5          | 4133                   | 3999                   | 4024                   | 3997                     | 3992                     | 4057                   | CN                    |

Columns are as described in Table 1.

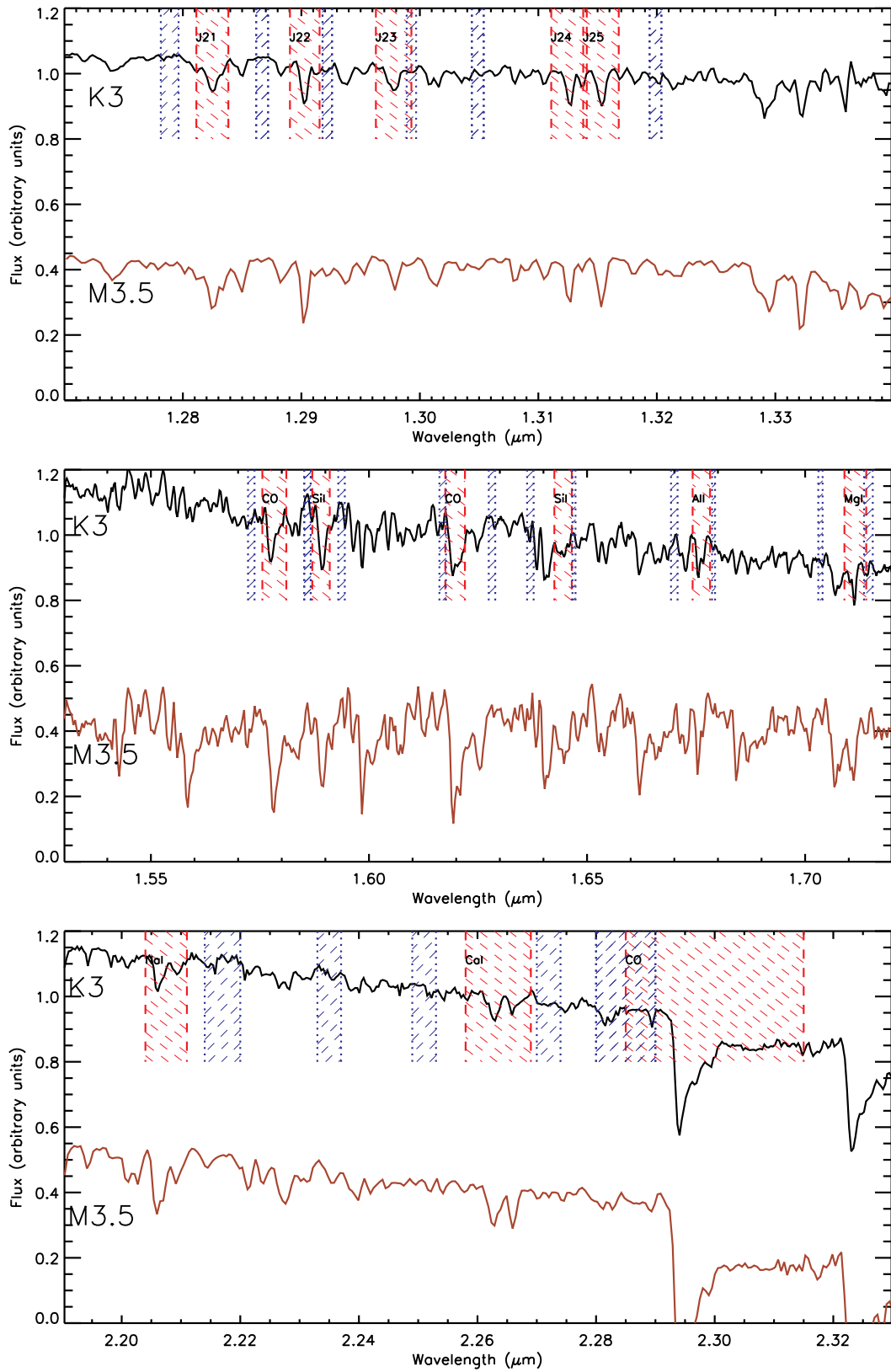


Figure 2. Continuation of Fig. 2

**Table 4**  
Definitions of used indices

| ID  | center<br>[ $\mu\text{m}$ ] | width<br>[ $\text{\AA}$ ] | continuum1<br>[ $\mu\text{m}$ ] | width1<br>[ $\text{\AA}$ ] | continuum2<br>[ $\mu\text{m}$ ] | width2<br>[ $\text{\AA}$ ] | Comments  |
|-----|-----------------------------|---------------------------|---------------------------------|----------------------------|---------------------------------|----------------------------|---|
| CO  | 2.3000                      | 300                       | 2.2850                          | 100                        | 2.2850                          | 100                        | Messineo et al. (2017)  |
| CaI | 2.2635                      | 110                       | 2.2510                          | 40                         | 2.2720                          | 40                         | as in Messineo et al. (2017)  |
| NaI | 2.2075                      | 70                        | 2.2170                          | 60                         | 2.2350                          | 40                         | as in Messineo et al. (2017) and in Ivanov et al. (2004)  |
| MgI | 1.7115                      | 50                        | 1.7035                          | 10                         | 1.7145                          | 20                         | as in Messineo et al. (2017) and center as in Ivanov et al. (2004)                              |
| AlI | 1.6762                      | 40                        | 1.6700                          | 15                         | 1.6790                          | 7                          | Messineo et al. (2017)  |
| SiI | 1.6445                      | 40                        | 1.6370                          | 15                         | 1.6470                          | 7                          | Messineo et al. (2017)  |
| CO  | 1.6198                      | 45                        | 1.6169                          | 15                         | 1.6282                          | 15                         | as in Messineo et al. (2017) and center as in Origlia et al. (1993)                             |
| SiI | 1.5890                      | 40                        | 1.5859                          | 15                         | 1.5937                          | 15                         | as in Messineo et al. (2017), center as in Ivanov et al. (2004)                                 |
| CO  | 1.5783                      | 55                        | 1.5730                          | 15                         | 1.5859                          | 15                         | Origlia et al. (1993)   |
| J25 | 1.3153                      | 30                        | 1.3049                          | 10                         | 1.3199                          | 10                         | Al at 1.315438 $\mu\text{m}$ +Fe+Si   |
| J24 | 1.3126                      | 30                        | 1.3049                          | 10                         | 1.3199                          | 10                         | Al at 1.312703 $\mu\text{m}$ +Ca  |
| J23 | 1.2978                      | 30                        | 1.2922                          | 8                          | 1.2993                          | 8                          | Mn at 1.2979500 $\mu\text{m}$   |
| J22 | 1.2903                      | 25                        | 1.2867                          | 10                         | 1.2922                          | 8                          | Mn at 1.290336 $\mu\text{m}$  |
| J21 | 1.2825                      | 27                        | 1.2789                          | 15                         | 1.2867                          | 10                         | Ti at 1.281499 $\mu\text{m}$ , Ca at 1.281955 $\mu\text{m}$                                     |
| J20 | 1.2085                      | 20                        | 1.2069                          | 10                         | 1.2149                          | 10                         | Mg at 1.2086 $\mu\text{m}$ , Si at 1.2085 $\mu\text{m}$ , CN                                    |
| J19 | 1.2036                      | 20                        | 1.2017                          | 10                         | 1.2069                          | 10                         | Si at 1.2034809 $\mu\text{m}$ , Mg 1.2086, CN   |
| J18 | 1.1976                      | 15                        | 1.1965                          | 7                          | 1.2017                          | 10                         | Fe at 1.1973771 & 1.1976325 $\mu\text{m}$ , Ti at 1.1977134 $\mu\text{m}$                       |
| J17 | 1.1887                      | 30                        | 1.1854                          | 10                         | 1.1917                          | 10                         | Fe at 1.1886096 and 1.1887336 $\mu\text{m}$ , Ti at 1.1896127 $\mu\text{m}$ , CN                |
| J16 | 1.1831                      | 20                        | 1.1814                          | 10                         | 1.1854                          | 10                         | Mg at 1.183141 $\mu\text{m}$  |
| J15 | 1.1785                      | 15                        | 1.1723                          | 10                         | 1.1814                          | 10                         | Ti, Fe, CN  |
| J14 | 1.1693                      | 30                        | 1.1656                          | 10                         | 1.1723                          | 10                         | Fe at 1.1693174 $\mu\text{m}$   |
| J13 | 1.1641                      | 15                        | 1.1569                          | 10                         | 1.1656                          | 10                         | Fe, Si, Ti, CN  |
| J12 | 1.1612                      | 20                        | 1.1569                          | 10                         | 1.1656                          | 10                         | Fe at 1.161075 $\mu\text{m}$ , Cr at 1.161374 $\mu\text{m}$ , Si at 1.161428 $\mu\text{m}$ , CN |
| J11 | 1.1595                      | 18                        | 1.1569                          | 10                         | 1.1656                          | 10                         | Fe at 1.1596762 $\mu\text{m}$ , CN  |
| J10 | 1.0930                      | 20                        | 1.0803                          | 7                          | 1.0914                          | 10                         | CN  |
| J9  | 1.0873                      | 20                        | 1.0803                          | 7                          | 1.0914                          | 10                         | Fe at 1.0866494 $\mu\text{m}$ and Si at 1.0871763 and 1.0872520 $\mu\text{m}$                   |
| J8  | 1.0788                      | 15                        | 1.0713                          | 10                         | 1.0803                          | 7                          | Si at 1.0787510 and 1.0789814 $\mu\text{m}$ and Fe at 1.0786009 $\mu\text{m}$                   |
| J7  | 1.0754                      | 25                        | 1.0713                          | 10                         | 1.0803                          | 7                          | Si at 1.0752330 $\mu\text{m}$ , Fe 1.0755950 $\mu\text{m}$                                      |
| J6  | 1.0729                      | 30                        | 1.0713                          | 10                         | 1.0803                          | 7                          | Ti at 1.0729326 and 1.0735811, Si at 1.0730351, Fe at 1.0728129 $\mu\text{m}$                   |
| J5  | 1.0664                      | 15                        | 1.0634                          | 10                         | 1.0713                          | 10                         | Si at 1.0663891 $\mu\text{m}$ and Ti at 1.0664551 $\mu\text{m}$                                 |
| J4  | 1.0587                      | 18                        | 1.0559                          | 15                         | 1.0634                          | 10                         | Fe at 1.0580 $\mu\text{m}$ , Ti at 1.05875 $\mu\text{m}$ , and Si 1.0588 $\mu\text{m}$ , VO     |
| J3  | 1.0399                      | 18                        | 1.0364                          | 10                         | 1.0444                          | 10                         | Fe at 1.03986 $\mu\text{m}$ and Ti at 1.03996 $\mu\text{m}$                                     |
| J2  | 1.0345                      | 17                        | 1.0314                          | 10                         | 1.0364                          | 10                         | Fe at 1.0343722 $\mu\text{m}$ and Ca at 1.0346644 $\mu\text{m}$                                 |
| J1  | 1.0330                      | 19                        | 1.0314                          | 10                         | 1.0364                          | 10                         | Sr at 1.0330141 $\mu\text{m}$   |
| MgI | 0.8807                      | 15                        | 0.8781                          | 12                         | 0.8855                          | 10                         | as in Diaz et al. (1989)  |
| Ca3 | 0.8662                      | 30                        | 0.8455                          | 15                         | 0.8855                          | 15                         | as in Diaz et al. (1989)  |
| Ca2 | 0.8542                      | 30                        | 0.8455                          | 15                         | 0.8855                          | 15                         | as in Diaz et al. (1989)  |
| Ca1 | 0.8498                      | 30                        | 0.8455                          | 15                         | 0.8855                          | 15                         | as in Diaz et al. (1989)  |

**Notes.** The lines listed in the comments are from high-resolution spectra of Hinkle et al. (1995).

The FeI-1.1611, FeI-1.641, FeI-1.1887, FeI-1.976 lines of Davies et al. (2010) are included in the J12, J13, J17, and J18 indices, respectively.

Our indices contain only two of the best four iron lines for temperature determination of Taniguchi et al. (2020). Fe I at 1.0395794  $\mu\text{m}$  (pair 8) is contained in the J3 index, and the Fe I line at 1.0754753  $\mu\text{m}$  (pair 9) in J7.

These are the correspondences between the lines of Morelli et al. (2020) and those in this work: FeTi (Morelli et al.)  $\approx$  J3 (this work), CN  $\approx$  J9, FeCr  $\approx$  J12 Mg I  $\approx$  J16, Al  $\approx$  J24+J25, SiMg  $\approx$  J20, Si I  $\approx$  Si I (1.59  $\mu\text{m}$ ), CO 1.62  $\approx$  CO 1.62, Al  $\approx$  Al (1.67  $\mu\text{m}$ ), Mg I  $\approx$  Mg I (1.71  $\mu\text{m}$ )+CO. Generally, we have used closer continua. The COMg index around 1.71  $\mu\text{m}$  of Morelli et al. (2020) includes both the CO band head and Mg I line at 1.71  $\mu\text{m}$ . We have measured the Mg I line only.

band head at  $2.29 \mu\text{m}$ . Giants and RSGs, because of their different ranges of gravity, fall in two different CO versus  $T_{\text{eff}}$  relations. Since RSGs span a larger range of  $[\text{CO}, 2.29]$ , late-type RSGs with types later than an M0 can be unambiguously identified at infrared wavelengths. Giants and RSGs overlap in this measurement for types earlier than M0. The  $[\text{CO}]$  values at  $1.62 \mu\text{m}$  are plotted versus the  $[\text{CO}]$  values at  $2.29 \mu\text{m}$  in Fig. 3; the  $[\text{CO}]$  at  $1.62 \mu\text{m}$  is another indicator of temperature.

#### CO band heads and $\text{H}_2\text{O}$ index

Large amplitude variable (LAV or Mira) AGBs stars do not follow the CO relations found for giants, or RSGs (see, e.g. Blum et al. 2003). Usually, at infrared wavelengths, astronomers distinguish RSG stars and O-rich Mira AGBs by measuring the depth of the  $\text{H}_2\text{O}$  absorption at the edges of the  $H$ -band (see, e.g. Blum et al. 2003; Comerón et al. 2004). O-rich Mira AGB stars have generally strong continuum absorption due to water in their envelopes.

Measurements of water vapour absorptions were performed as described in Blum et al. (2003) and Messineo et al. (2017).

#### Ca I at $2.26 \mu\text{m}$

The Ca I and the Na I lines are the two strongest atomic lines in the  $K$ -band. The  $[\text{Ca I}, 2.26]$  and  $[\text{Na I}, 2.21]$  well correlate with temperature and with the EW of the CO band head at  $2.29 \mu\text{m}$  (e.g., Ramirez et al. 1997). At the resolution of the SpeX library, the Ca I line is a good temperature indicator (Cesetti et al. 2013; Rayner et al. 2009).

#### Na I at $2.21 \mu\text{m}$

is a temperature indicator (e.g. Ramirez et al. 1997; Cesetti et al. 2013; Rayner et al. 2009; Park et al. 2018).

#### Mg I at $1.71 \mu\text{m}$

The Mg I line at  $1.71 \mu\text{m}$  is prominent (Origlia et al. 1993) and correlates with temperature for evolved late-type stars (Rayner et al. 2009). Messineo et al. (2017) inspected various correlations between this Mg I line and other lines. The  $[\text{Mg I}, 1.71]$  value, in combination with the  $[\text{CO}]$  value, is a powerful diagnostic for luminosity class. Indeed, a given value of  $[\text{CO}]$ , the  $[\text{Mg I}, 1.71]$  value appears weaker in the spectra of RSGs than in those of normal giants, see Fig. 3. Sec. 5 outlines the importance of this line for classifying evolved cool stars.

#### Si I line at $1.59 \mu\text{m}$

The Si I line at  $1.59 \mu\text{m}$  was reported as one of the most prominent metal lines in  $H$ -band by Origlia et al. (1993). In the  $[\text{Si I}, 1.59]$  versus  $[\text{CO}, 2.29]$  plot, this Si I line appears stronger in the spectra of RSGs than in those of giants; when the EW of the CO band heads at  $2.29 \mu\text{m}$  are larger than  $\approx 42 \text{ \AA}$ , i.e., outside the range of red giants, RSGs can be distinguished from Mira AGBs by their larger  $[\text{Si I}, 1.59]$  ( $\geq 3.25 \text{ \AA}$ , see Fig. 3). Its strength does not appear to depend on the stellar temperature of the RSGs and it breaks the degeneracy between giants and supergiants. This line may serve, therefore, as an empirical gravity indicator, to locate the youngest population of evolved late-type stars, the RSGs. Recently, Thorsbro et al. (2020) has outlined the importance to study Si I lines to determine the history of Galactic  $\alpha$ -elements, which are found to be enhanced in the metal rich population of the central nuclear Disk.

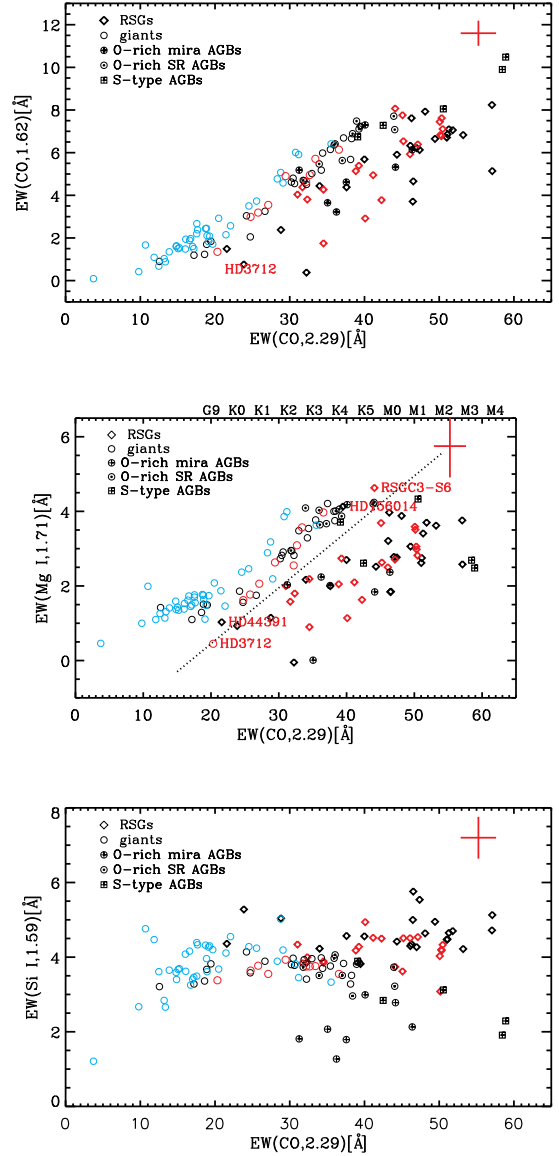


**Figure 3.** *Top panel:* The  $[\text{CO}, 1.62]$  vs. the  $[\text{CO}, 2.29]$  values. Data from the IRTF library of Rayner et al. (2009, black) and extended IRTF library of Villaume et al. (2017, cyan). Known O-rich Mira AGBs are marked with an encircled plus and O-rich SR AGBs with dotted circles; S-type AGBs with squared plus signs. The median of errors in both axes are plotted with red segments (length=  $2 \times$  error) at the top-left corner. Newly observed, but already known, RSGs from Table 1 are marked with red diamonds (2MASS J18345133–0713162 and 2MASS J18345840–0714247 from Table 1 with  $\text{ind}_{\text{H}_2\text{O}} > 6.6\%$  are not plotted). Giants from Table 3 are indicated with red circles. *Middle panel:* The  $[\text{Mg I}, 1.71]$  values vs. the  $[\text{CO}, 2.29]$  values. Symbols are as in the top panel. The dotted curve is as in Messineo et al. (2017) and separate giants and RSGs. The locations of 2MASS J17143885+1423253/HD 156014 (AGB) and 2MASS J18451939–0324483/RSGC3-S6 (RSG), 2MASS J06224788+2759118/HD 44391 (K0 Ib), and 2MASS J00403044+5632145/HD 3712 (K0 IIIa) are indicated with labels. *Bottom panel:* The  $[\text{Si I}, 1.59]$  values vs. the  $[\text{CO}, 2.29]$  values.

#### Si I line at $1.64 \mu\text{m}$

The Si I line at  $1.64 \mu\text{m}$  appears as the second Si I line in strength present in the  $H$ -band models of Origlia et al. (1993), but it is much fainter than the line at  $1.59 \mu\text{m}$ . We defined an index for it in Messineo et al. (2017). The  $[\text{Si I}, 1.64]$  is here

found to correlate with the stellar  $T_{\text{eff}}$  values.

### Al I

Origlia et al. (1993) also identified the Al I line at  $1.67 \mu\text{m}$ . In the work of Park et al. (2018), it does not appear to be a temperature indicator for bright giants. We did not find correlations with luminosities.

### Y and J-bands indices

The Y-band ( $0.95\text{-}1.13 \mu\text{m}$ ) and J-band ( $1.13\text{-}1.35 \mu\text{m}$ ) contain prominent Ti I, Si I, Al I, Mg I, Mn I, Cr I, Sr I, and Fe I lines, and a variety of molecular bands (e.g. Joyce et al. 1998; Hinkle et al. 1995; Rayner et al. 2009; Davies et al. 2010; Morelli et al. 2020). The 25 lines are listed in Table 4, and along the text are shortly named as J1, J2, ... J25 as most of the lines considered are blends of several atomic lines. Among them, ten lines have been already analysed in the work of Davies et al. (2010) and Morelli et al. (2020) – J3 (FeTi), J9 (CN), J12 (FeCr), J13 (Fe+Si+Ti+CN), J16 (Mg I), J17 (Fe+Ti+CN), J18 (Fe+Ti), J20 (SiMg), and J24+J25 (Al). Their centerings and bandwidths are similar to those of Morelli et al. (2020), but generally, we have adopted closer and narrower continua. Indeed, the indexes of Morelli et al. (2020) were defined with the goal of studying integrated stellar populations, and the continua had to be placed away from H and He lines.

The dominant atomic elements or molecules contributing to these lines in the early K-type star Arcturus were identified by Hinkle et al. (1995) and are annotated in the comments of Table 4. The J9 (CN) is a good marker of CN enhancement, while J12 (FeCr) is a marker of gravity (Morelli et al. 2020). The J12, J13, J17, and J18 lines are useful for metallicity determination (Davies et al. 2010) (see Sect. 7). We anticipate that only eight (out of 25) lines were found to be extremely useful for spectroscopically confirming RSGs: 3 for CN enhancement (J8, J9, J10) and 5 for luminosity estimates (J12, J17, J18, J21, and J22) (see Sect. 4).

### Ca II triplet (CaT)

The SpeX detector in the chosen configuration covers the region of the Ca II triplet (CaT). Three prominent lines were detected at the expected wavelengths; 8498 (Ca1), 8542 (Ca2), 8666 (Ca3) Å. This well-studied region was also chosen for the Gaia spectrograph, as it allows us to classify spectral types and to assign luminosity classes. The CaT feature is useful to classify stars earlier than M3, as the spectra of stars with later types have strong TiO bands at this wavelength (see also López-Corredoira et al. 1999).

As shown in Diaz et al. (1989), the [CaT] defined as the sum of the EWs of the Ca2 and Ca3 lines is  $> 9 \text{ \AA}$  in RSGs for spectral types earlier than M2.5. [CaT] is larger than  $9 \text{ \AA}$  in 19 stars out of the 24 class I stars of the IRTF libraries (Rayner et al. 2009; Villaume et al. 2017). The remaining five stars have spectral types later than M2.5 and 2MASS J17143885+1423253/HD 156014 (M5 Ib-II) is an AGB (Moravveji et al. 2013). In our observations, the [CaT] could be measured only in 33% of the 72 observed spectra, with  $15 [\text{CaT}] > 9 \text{ \AA}$  for 13 previously known RSGs and two candidate RSGs.

### Mg I at $0.88 \mu\text{m}$

This line is a temperature indicator, discovered by Diaz et al.

(1989).

### 3.1. Homogeneity of the spectral library

Following Messineo et al. (2017), we measured the EW measurements after rebinning and smoothing the IRTF data. After rebinning, the EWs were smaller by a variable factor from a few percent up to 35% depending on the line and its signal-to-noise. This partly explains the large scatter among EWs of giants and RSGs observed when using different libraries. Among the lines, we note that the band and continua used for the Mg I at  $1.71 \mu\text{m}$  yield stable results; Mg I at  $1.71 \mu\text{m}$  is the strongest line in H-band after the CO at  $1.62 \mu\text{m}$ . It is recommended to quantitatively compare low-resolution spectra from the same instrument to build a reference frame that allows us to separate late-type giants and RSGs. Cesetti et al. (2013) and Morelli et al. (2020) have selected sensitive lines across the entire SpeX coverage for integrated-light stellar population studies with signal-to-noise as low as 30. Beside the already well studied lines in H (CO, Si, Mg, Al) and in K-band (Na, Ca, CO) and in Z-band (CaT), we explore 25 other lines in Y and J-bands which characterize the spectra of RSGs. For our EW measurements we required a minimum signal to noise of 50. Six of these lines correspond to spectral indices selected also by Morelli et al. (2020) (see footnote of 4).

Data with the new SpeX yield EWs consistent within errors with those obtained with the old SpeX. Indeed, we re-observed three giants from the IRTF library, as shown in Table 5.

## 4. LUMINOSITIES OF SUPERGIANTS

In this section, we analyze the correlation between line strength and luminosities, with the aim of locating spectral lines suitable for determining luminosity classes, or even of predicting luminosities from EWs. Luminosities and EWs are independently obtained.

The luminosities of Galactic RSGs range from  $\log(L/L_{\odot})=3.5$  to 5.6 (Levesque et al. 2005; Messineo & Brown 2019). Evolutionary tracks predict that gravity linearly correlates with  $L$  and  $T_{\text{eff}}$  (Limongi 2017; Bertelli et al. 2009), and an estimate of the stellar gravity can be obtained as described in Appendix A.

### 4.1. Measurements of luminosity and $T_{\text{eff}}$ of RSGs

We collected a total of 45 spectra of 44 known RSGs observed with the SpeX detector on the IRTF telescope. 21 of these spectra are from the IRTF library (i.e., all those inherent class I stars without counting  $\alpha$  Her, which is an AGB), two from the extended library, and 21 others were observed during our runs.

Their luminosities were estimated by using parallactic distances from Gaia EDR3<sup>8</sup> (Gaia Collaboration et al. 2020) and infrared magnitudes from  $1 \mu\text{m}$  to  $21 \mu\text{m}$ , as well as with the  $BC_K$  of Levesque et al. (2005) and Neugent et al. (2020),

<sup>8</sup> The quasar median zero point of  $-0.017 \text{ mas}$  was applied to the parallaxes. The use of the provided “tentative recipe” (Gaia Collaboration et al. 2020) for obtaining more precise individual corrections as a function of magnitudes, colors, and positions would yield a mean correction of  $-0.043 \text{ mas}$  with a  $\sigma$  of  $0.019 \text{ mas}$ . The effect on the luminosity would be a mean decrease of  $-0.048$  with a  $\sigma$  of  $0.054$ . Brightness fluctuations characterize the surface of RSGs (Chiavassa et al. 2011). However, this does not yield systematic parallax errors, but only degrades the quality of the fit (Messineo & Brown 2019).

**Table 5**

Ratios between the EWs from the newly observed spectra and those in the IRTF library for the giants 2MASS J23300740+4907592/HD 221246, 2MASS J20224530+4101338/HD 194193, and 2MASS J13492867+1547523/HD 120477.

| EW(line)     | Ratio      | (EW(Lib.)-EW(New obs))<br>[Å] | <EW(RSG)e>*<br>[Å] |
|--------------|------------|-------------------------------|--------------------|
| [CO, 2.29]   | 0.98± 0.05 | 0.55± 1.51                    | 2.28               |
| [Na I, 2.21] | 1.20± 0.08 | -0.54± 0.20                   | 0.42               |
| [Ca I, 2.26] | 1.02± 0.07 | -0.04± 0.20                   | 0.89               |
| [Si I, 1.59] | 0.97± 0.02 | 0.11± 0.08                    | 0.59               |
| [CO, 1.62]   | 1.00± 0.03 | 0.00± 0.14                    | 0.62               |
| [Si I, 1.64] | 1.63± 0.21 | -0.89± 0.31                   | 0.68               |
| [Mg I, 1.71] | 0.94± 0.05 | 0.19± 0.13                    | 0.77               |
| [Al I, 1.67] | 0.69± 0.12 | 0.38± 0.15                    | 0.67               |
| [J1]         | 1.05± 0.19 | -0.03± 0.09                   | 0.08               |
| [J2]         | 1.03± 0.11 | -0.01± 0.06                   | 0.06               |
| [J3]         | 1.01± 0.09 | -0.00± 0.05                   | 0.09               |
| [J4]         | 0.94± 0.09 | 0.03± 0.05                    | 0.09               |
| [J5]         | 1.00± 0.04 | -0.00± 0.02                   | 0.11               |
| [J6]         | 1.01± 0.09 | -0.01± 0.06                   | 0.31               |
| [J7]         | 0.91± 0.09 | 0.04± 0.05                    | 0.24               |
| [J8]         | 0.99± 0.07 | 0.01± 0.03                    | 0.11               |
| [J9]         | 1.70± 0.91 | -0.32± 0.39                   | 0.70               |
| [J10]        | 2.92± 1.95 | -0.81± 0.65                   | 0.76               |
| [J11]        | 1.23± 0.18 | -0.09± 0.06                   | 0.18               |
| [J12]        | 1.02± 0.03 | -0.02± 0.03                   | 0.22               |
| [J13]        | 1.14± 0.27 | -0.04± 0.10                   | 0.14               |
| [J14]        | 1.15± 0.34 | -0.05± 0.13                   | 0.34               |
| [J15]        | 1.05± 0.19 | -0.02± 0.09                   | 0.10               |
| [J16]        | 0.99± 0.06 | 0.01± 0.07                    | 0.14               |
| [J17]        | 0.92± 0.12 | 0.11± 0.15                    | 0.22               |
| [J18]        | 0.66± 0.36 | 0.30± 0.31                    | 0.07               |
| [J19]        | 0.86± 0.09 | 0.09± 0.06                    | 0.10               |
| [J20]        | 0.84± 0.15 | 0.08± 0.08                    | 0.09               |
| [J21]        | 0.92± 0.16 | 0.13± 0.23                    | 0.07               |
| [J22]        | 1.12± 0.14 | -0.07± 0.08                   | 0.33               |
| [J23]        | 3.02± 1.89 | -0.11± 0.18                   | 0.30               |
| [J24]        | 1.03± 0.12 | -0.01± 0.08                   | 0.25               |
| [J25]        | 0.94± 0.25 | 0.04± 0.14                    | 0.25               |

(\*) Average errors on the measured EWs of RSGs in the IRTF library (Rayner et al. 2009).

as in the catalog of Messineo & Brown (2019). Interstellar extinction  $A_{K_s}$  was estimated using the 2MASS  $JHK_s$  photometry (Skrutskie et al. 2006), the intrinsic colors from the work of Koornneef (1983), and the extinction power law described in Messineo et al. (2005) (see also, Messineo et al. 2017; Messineo & Brown 2019).  $T_{\text{eff}}$  values were estimated using the temperature scale of Levesque et al. (2005) and the adopted spectral types (see also, Messineo & Brown 2019). Estimated luminosities are listed in Table 1. As the spectral types adopted by Messineo & Brown (2019) were often the average of historical records listed in Skiff (2014), the original references to the spectroscopic works are also provided in Table 1.

For the comparison sample of spectra of giants from the extended IRTF library, luminosity estimates are given in the catalog of Villeneuve et al. (2017). Their luminosities were estimated with direct integration under the stellar energy distributions, which were built with observed flux densities from UV to infrared light and with the Gaia DR2 parallactic distances. For these giants, in the plots we use the  $T_{\text{eff}}$  listed in the catalog of Prugniel et al. (2011). The  $T_{\text{eff}}$  values of the MILES spectra were determined by comparison with the tem-

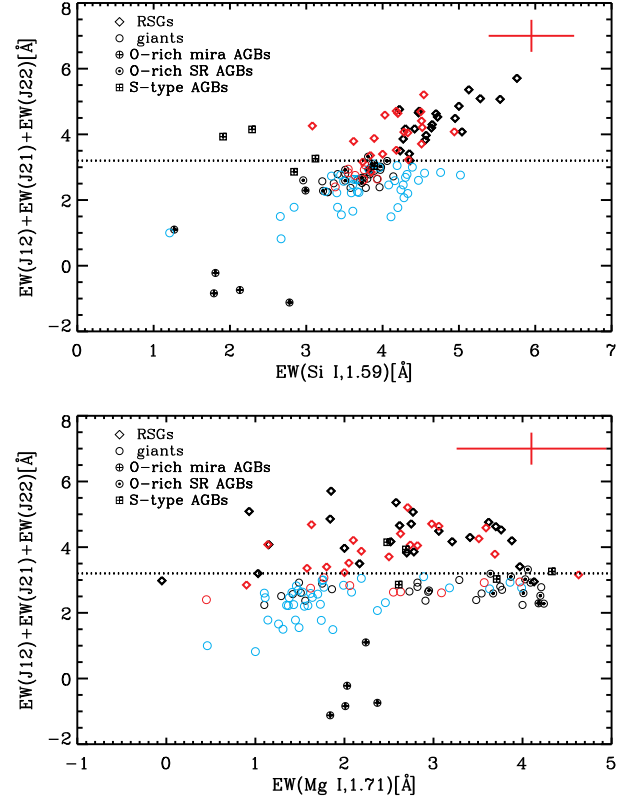


**Figure 4.** *Top panel:* [J12+J21+J22] values are plotted vs. the [Si I, 1.59] values. Stars above the dashed line at 3.2 Å are RSGs. *Bottom panel:* [J12+J21+J22] values are plotted vs. the [Mg I, 1.71] values. Stars above the dashed line at 3.2 Å are RSGs. Symbols and colors are as in Fig. 3.

**Table 6**

Infrared luminosity-class indicators for evolved late-type stars

| Line ID          | Center<br>[μm] | Elements        | separator<br>EW(RSG)[Å] |
|------------------|----------------|-----------------|-------------------------|
| J1               | 1.0331         | Sr at 1.0330141 | > 0.7                   |
| J12 <sup>a</sup> | 1.1613         | Fe+Cr+Si        | > 1.0                   |
| J17              | 1.1888         | Fe+Ti           | > 1.5                   |
| J18              | 1.1977         | Fe+Ti           | > 1.0                   |
| J21              | 1.2826         | Ti+Ca           | > 1.7                   |
| J22              | 1.2904         | Mn at 1.290336  | > 0.8                   |

**Notes:** For Galactic RSGs, the above infrared lines have EWs with similar behaviors. They do not correlate with  $T_{\text{eff}}$ , and neither with [Mg I, 1.71]. They do correlate with [Si I, 1.59] and with each other (Fig. 4), and are larger in RSGs than in giants.

<sup>a</sup> J12 corresponds to FeCr gravity indicator of Morelli et al. (2020).

plate spectra of the ELODIE library using an interpolator.

#### 4.2. New indicators of luminosity in $Y$ - and $J$ -bands

The  $Y$ - and  $J$ -bands indices defined in Table 4 were plotted against the [CO, 2.29], [Mg I, 1.71], and [Si I, 1.59] values, respectively. The [CO, 2.29] is very sensitive to temperature, as well as the Mg I line at 1.71 μm. The strengths of the Si I at 1.59 μm and Mg I line at 1.71 μm are uncorrelated; the Si I line tends to be higher in RSGs (e.g. plots in Origlia et al. 1993). The analysis of these plots promptly allowed us to locate other lines with analogous behaviors. We found that the strengths of the J1 (1.033 μm), J12 (1.161

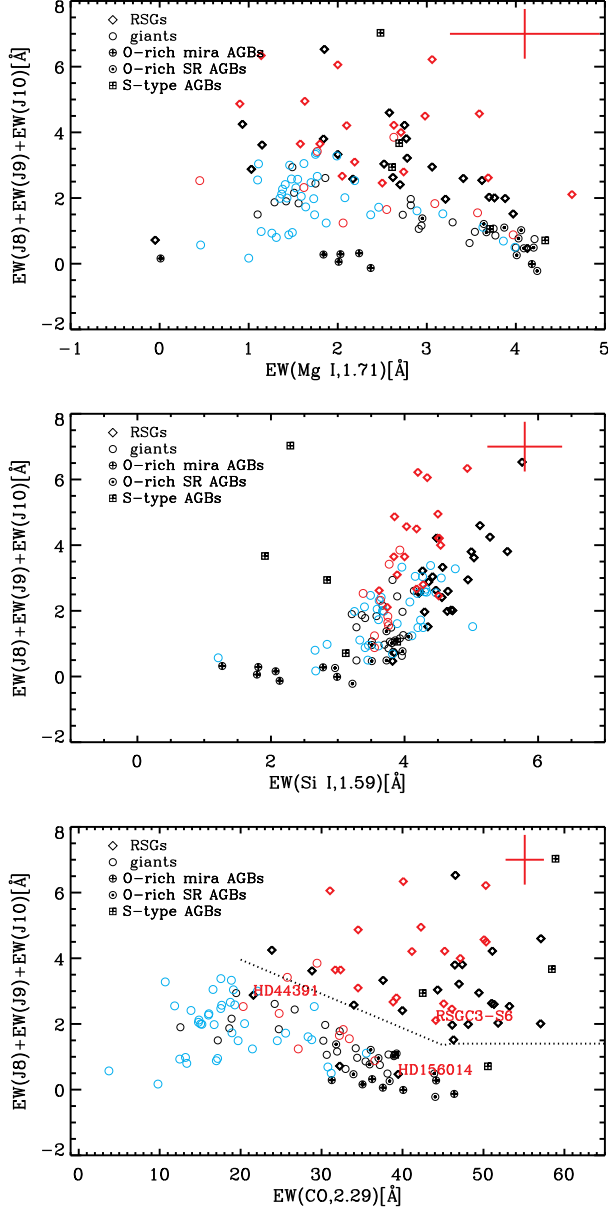


**Figure 5.** *Top panel:* [J8+J9+J10] values are plotted vs. the [Mg I, 1.71] values. *Middle panel:* [J8+J9+J10] values are plotted vs. the [Si I, 1.59] values. *Bottom panel:* [J8+J9+J10] values are plotted vs. the [CO, 2.29] values. Symbols and colors are as in Fig. 3. Typically, RSGs are located above the dotted line.

$\mu\text{m}$ ), J17 (1.188  $\mu\text{m}$ ), J18 (1.198  $\mu\text{m}$ ), J21 (1.282  $\mu\text{m}$ ), and J22 (1.290  $\mu\text{m}$ ) lines remained quite constant with increasing strength of Mg I, i.e. they were independent of temperature, and RSGs were located visibly above a certain threshold, with giants and AGBs below it, as listed in Table 6. Moreover, they would linearly correlate with the strength of the Si I at 1.59  $\mu\text{m}$ . When plotting these  $Y$ - and  $J$ -band indices against each other, a linear correlation is seen. To minimize the observational errors, combined indices were also measured, for example, [J12+J17+J18] and [J21+J22] (see Fig. 4). For these two indices, using the thresholds given in Table 6, we were able to retrieve 82% and 82% of the sample of known RSGs, respectively (or 79% and 74% of the K-type RSG sam-

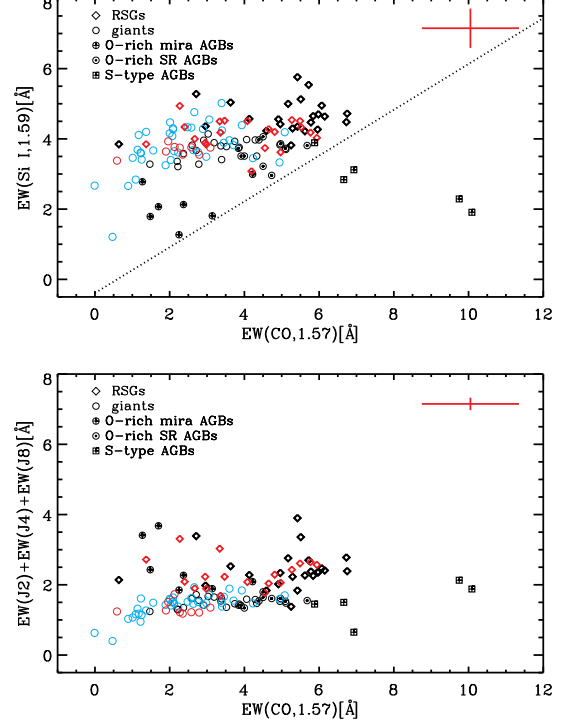


**Figure 6.** *Top panel:* The [CO, 1.57] vs. [Si I, 1.59] diagram. Symbols and colors are as in Fig. 3. Data points lying below the dotted line are typical of S-type stars (Rayner et al. 2009). *Bottom panel:* The [CO, 1.57] vs. [J2+J4+J8] diagram.

ple). The J12 feature at 1.161  $\mu\text{m}$  may contain Fe I, Cr I, and Si I atomic lines, as well as strong CN bands, as seen in the high-resolution spectrum of the K-type giant Arcturus (Hinkle et al. 1995). The J17 and J18 features at 1.189 and 1.198  $\mu\text{m}$  are made up of blended Fe I and Ti I lines. The J21 feature at 1.283  $\mu\text{m}$  is made up of Ti I, Ca I, and possible CN lines. The J1 (1.033  $\mu\text{m}$ ) and J22 (1.290  $\mu\text{m}$ ) lines are unblended lines from Sr I and Mn I, respectively.

In contrast to the  $Y$ - and  $J$ -bands lines above mentioned, the [J8+J9+J10] values appear slightly anti-correlated with those of CO and Mg I in red giants (the J9 and J10 lines at 1.087 and 1.093  $\mu\text{m}$  are CN dominated). The diagrams of [J8+J9+J10] values versus CO or Mg I EWs are useful indicators of luminosity classes, as shown in Fig. 5. The area above the dotted curve encloses 95% of the known RSGs (90% of the known K-type RSGs). Unfortunately, S-type stars occupy the same area as RSGs. However, in the [CO, 1.57] vs. [J2+J4+J8] S-type stars have fainter [J2+J4+J8] and larger [CO, 1.57] than those in RSGs (see Fig. 6). The J4 blend contains the Si I line at 1.0588  $\mu\text{m}$  (J4) and the J8 the Si I line at 1.078  $\mu\text{m}$ .

These indices enable us to separate RSGs from giants using only the  $Y$ - and  $J$ -bands. Figs. 7, and 8 show the relation between these indices and luminosity. The EWs of the J1, J12, J17, J18, J21, and J22 lines mildly correlate with the stellar luminosities, but not with the  $T_{\text{eff}}$  values (Fig. 8).

A direct estimation of luminosities from these spectral indices is possible. For example, [J12+J17+J18] yields luminosities in agreement with those from photometry with a  $\sigma=0.31 \text{ Log}(L/L_{\odot})$ , as elucidated in Fig. 9.

We remark that all findings of this work are based on empirical correlations of observational EWs at infrared wave-

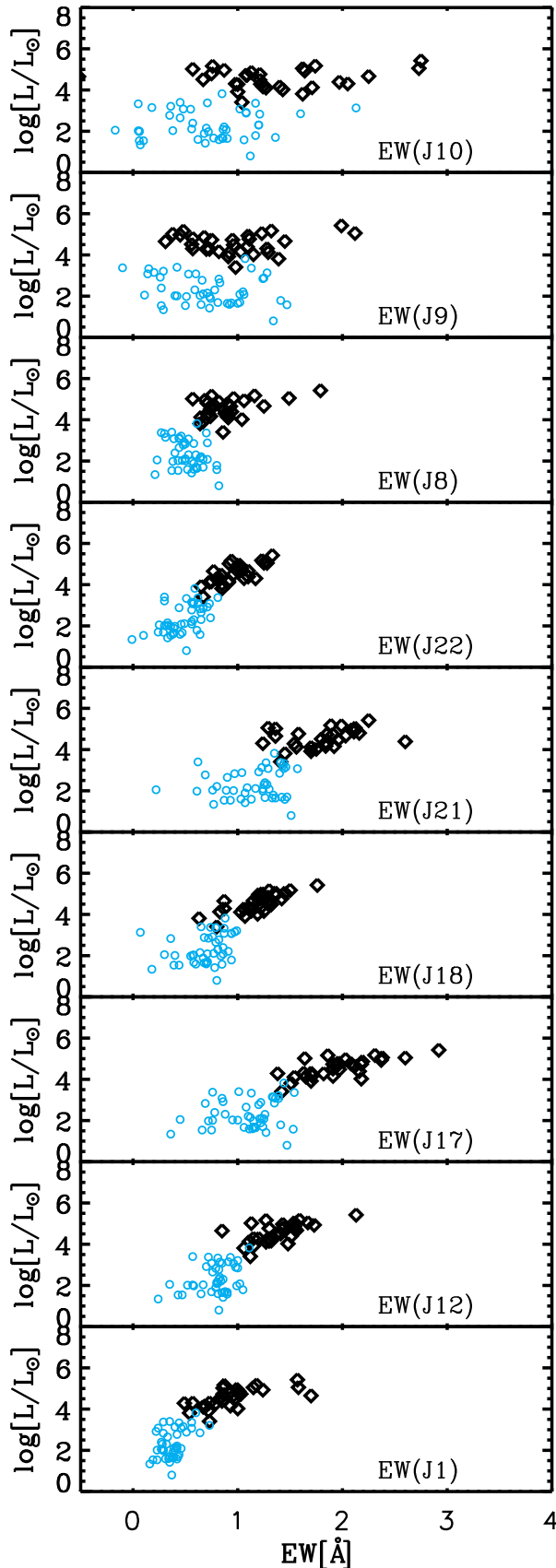


**Figure 7.** The  $\log(L/L_{\odot})$  (with Gaia EDR3 distances with fractional errors  $< 25\%$ ) are plotted vs. EW values of the J1, J12, J17, J18, J21, J22 lines and J8, J9, and J10. Indices of RSGs from Table 1 are marked with black diamonds. The indices of giants with luminosities estimated in Villaume et al. (2017) and the newly observed giants from Table 3 are overplotted with cyan open circles.

lengths. These tools are stable and independent of any modeling.

### 5. MAGNESIUM: THE [CO, 2.29] VERSUS [Mg I, 1.71] DIAGRAM

The Mg I at  $1.71 \mu\text{m}$  is a key infrared line that allows us to separate giants from RSGs.

In the [CO, 2.29] versus [Mg I, 1.71] diagram, giants are located above RSGs (Messineo et al. 2017), as shown in Fig. 3. A linear curve is drawn to roughly mark the two sectors of the diagrams (that occupied by giants, and that of RSGs). More precisely, 95% of the known RSGs listed in Table 1 are located to the right of this curve. This diagram separates well RSGs (with spectral types from K0 to M5) and normal giants, independently of their spectral types. At the two extremes, three data points deviate from the trend: the 2MASS J06224788+2759118/HD 44391 (K0 Ib), which is nevertheless identified by its strong CaT lines and CN head bands, and 2MASS J18451939-0324483/RSGC3-S6 (M4.5 I) and 2MASS J17143885+1423253/HD 156014 (M5 Ib-II), which remain located on the giant sequence of the diagram.

C-rich and S-type AGB stars, as well as the O-rich Mira AGB stars, are distributed similarly to the RSGs.

For stars of 1 and  $15 M_{\odot}$ , a grid of synthetic infrared spectra with solar metallicity covering temperatures from 2900 K to 4500 K and  $\log(g [\text{cm s}^{-2}])$  from  $-1$  to 2 has been published by Lançon et al. (2007). Galactic RSGs have a typical  $\log(g [\text{cm s}^{-2}])$  value ranging from  $-0.5$  to 1 (Davies et al. 2010) (see Appendix A). Giants cover a broader range from  $+3$  (near 5000 K) to  $-0.2$  (near 3000 K) (Bessell et al. 1998). In the panel (a) of Fig. 10, we used the Lançon et al. synthetic spectra to reproduce the theoretical distribution of [Mg I, 1.71] values with temperatures. The Mg I absorption line at  $1.71 \mu\text{m}$  strengthens with decreasing temperature. By lowering the stellar surface gravity, this line notably weakens (panel (e) of Fig. 10). Indeed, as shown in panel (f), observed Galactic giants have a stronger Mg I line than RSGs; The [Mg I, 1.71] values of giants sit on a different sequence above that of RSGs. The Mg I line at  $1.71 \mu\text{m}$  correlates only with the stellar temperature, as shown in panels (c) and (d) of Fig. 10, unlike the CO lines. These behaviors of the EWs are confirmed with the high-resolution spectra of Park et al. (2018).

When plotting the Mg I versus the CO absorption strengths measured from the models of Lançon et al. (2007) (panel (e) of Fig. 10), a luminosity separation is visible, with the giants data points lying on the top of those of supergiants. The diagram of [Mg I, 1.71] values versus [CO, 2.29] values provides an observational tool to separate normal giants and supergiants, because it removes the ambiguity in the relation of [CO, 2.29] and  $T_{\text{eff}}$  diagram.

### 6. TEMPERATURES OF SUPERGIANTS

The  $T_{\text{eff}}$  values of known RSGs range from about 4500 K to 3500 K. At optical wavelengths, spectral types of RSGs and temperatures ( $T_{\text{TiO}}$ ) are usually defined on the basis of the strengths of their TiO bands. In recent literature, this temperature scale has been intensely discussed and even questioned.

Infrared estimates of spectral types have been carried out with the EWs of the CO band head at  $2.29 \mu\text{m}$  (e.g., Figer et al. 2006). At shorter wavelengths, the TiO band heads at  $0.88 \mu\text{m}$  is often used (Dorda et al. 2016b,a). The infrared spectral types are more uncertain than those from optical studies.



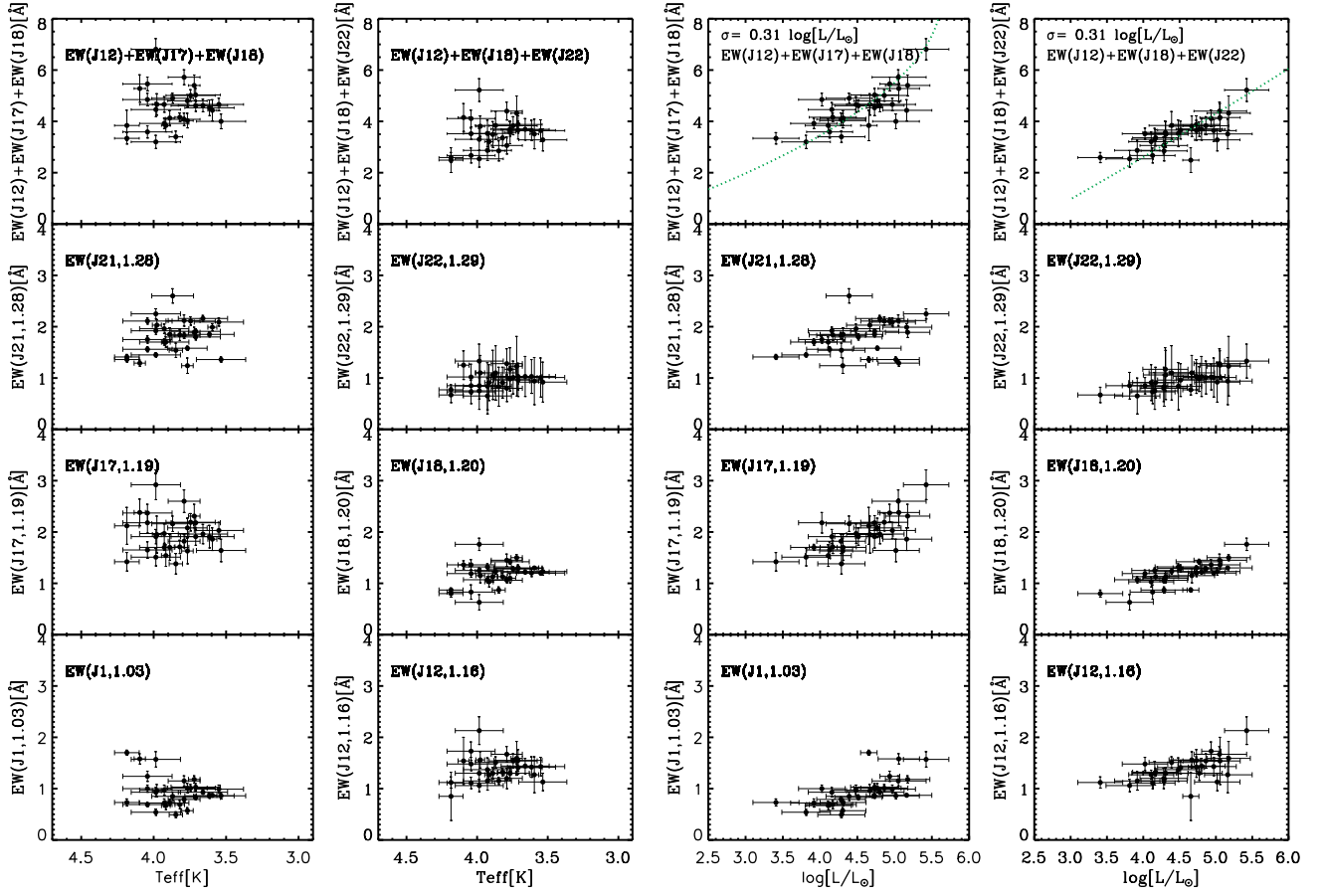


**Figure 8.** EW indicators of luminosity. *Columns 1 and 2:* The EW values of the J1, J12, J17, J18, J21, J22 lines of known RSGs are plotted vs. the  $T_{\text{eff}}$  values. *Columns 3 and 4:* For a direct comparison, their EWs are also plotted vs. the  $\log(L/L_{\text{sun}})$  (Gaia EDR3 distances). These are the same RSG data points displayed in Fig. 7. Symbols are as in Columns 1 and 2. **In the top two panels,  $\text{EW}(J12)+\text{EW}(J17)+\text{EW}(J18)$  and  $\text{EW}(J12)+\text{EW}(J18)+\text{EW}(J22)$  vs.  $\log(L/L_{\odot})$  diagrams, the two green dotted lines are polynomial fits to the data points (used to estimate the spectroscopic  $\log(L/L_{\odot})$ , see text below).**

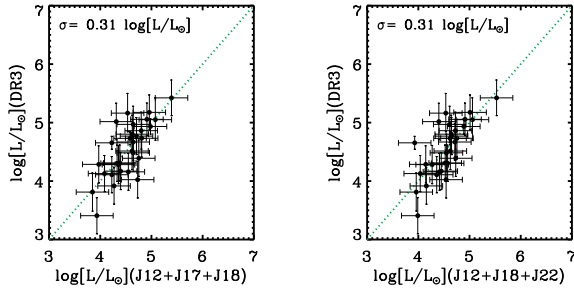


**Figure 9.** Examples of spectroscopic luminosities. Luminosities inferred from the J12, J17, J18 lines of RSGs (*left panel*) and from the J12, J18, J22 lines of RSGs (*right panel*) are compared with the photometric luminosities (based on the Gaia EDR3 distances). Identity is depicted by the green dashed line.

We found that the [CO, 2.29], [Ca I, 2.26], [Na I, 2.21], [Mg I, 1.71], [Si I, 1.64], [CO, 1.62], [J3], and [J6] values correlate with the  $T_{\text{TO}}$  temperatures as shown in Fig. 11. We neglected any dependence on  $Z$ , because the  $Z$  range of Galactic RSGs is small anyway, and we used 2nd order polynomial fittings to estimate the temperatures of RSGs. We used 21 spectra of RSGs from the two IRTF libraries (we excluded the three outliers 2MASS J20285059+3958543

(RW Cyg), 2MASS J17143885+1423253 (HD 156014), and 2MASS J22543171+6049388 (MY Cep), plus 2MASS J19461557+1036475 ( $\gamma$  Aql), 2MASS J21045763+4708491 (HD 200945), and 2MASS J20112810+2201354 (BD+21 4089), which were observed during our runs. The results are listed in Tables 1, 2, and 3. The fits were done with temperatures from 4180 K (K0) to 3535 K (M5). We used extrapolations for temperatures lower than that (i.e. larger EWs) resulting in M5-M6 types (see Table 1).

The [CO, 2.29], [J3], and [J6] show a dependence on both luminosity and  $T_{\text{eff}}$ ; the [Ca I, 2.26], [Na I, 2.21], [Mg I, 1.71], [Si I, 1.64], and the [CO, 1.62] values do not show a clear correlation with the luminosities; so the latter EWs are better indicators of temperature. The high-resolution data of Park et al. (2018) show that the [Ca I, 2.26], [Na I, 2.21], and [Mg I, 1.71] of cold supergiants do not correlate with gravity, and increase with increasing temperatures.

The average temperatures and spectral types were inferred by averaging the [Na I, 2.21], [Mg I, 1.71], [Si I, 1.64], and [CO, 1.62] of our targets with those of reference RSGs, and are indicated as  $T_{\text{combi}}$  and  $\text{Sp}_{\text{combi}}$ , respectively. The average EWs of RSGs per spectral type are listed in Table 8, and three spectral features per spectral type are shown in Fig. 12.

For the reference stars, the differences between the inferred temperatures and those from the optical classification

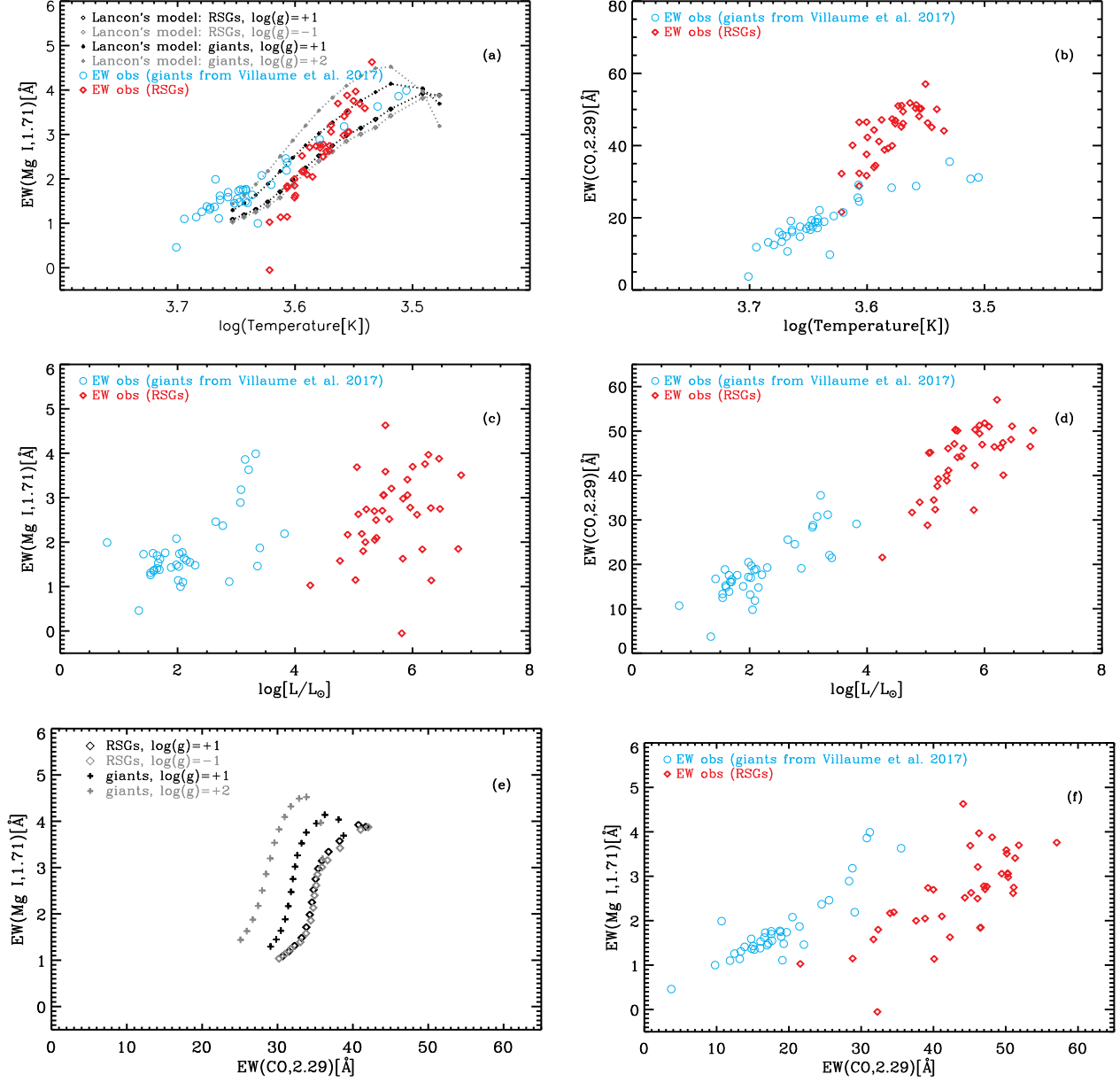


**Figure 10.** *Panel (a):* The [Mg I, 1.71] values vs. stellar  $T_{\text{eff}}$  estimated from the models of Lançon et al. (2007). Connected gray crosses mark the locus of giants with  $\log(g)=+2$ , black crosses the locus of giants with  $\log(g)=+1$ . Connected gray diamonds mark the locus of RSGs with  $\log(g)=-1$ , black diamonds the locus of RSGs with  $\log(g)=+1$ . The observed [Mg I, 1.71] and  $T_{\text{eff}}$  of giants from the work of Villaume et al. (2017) are overplotted with cyan circles; those of known RSGs (IRTF libraries and newly observed) with red diamonds;  $T_{\text{eff}}$  values are taken from Table 1. *Panel (b):* EWs of the CO band head at  $2.29 \mu\text{m}$  vs. stellar  $T_{\text{eff}}$ . Symbols are as in panel (a). *Panel (c):* [Mg I, 1.71] values vs. luminosities. Symbols are as in panel (a). *Panel (d):* The [CO, 2.29] values vs. the stellar luminosities. Symbols are as in panel (a). *Panel (e):* The theoretical [Mg I, 1.71] values vs. the [CO, 2.29] values estimated from the models of Lançon et al. (2007). *Panel (f):* The observed [Mg I, 1.71] values vs. the [CO, 2.29] values; symbols are as in panel (a).

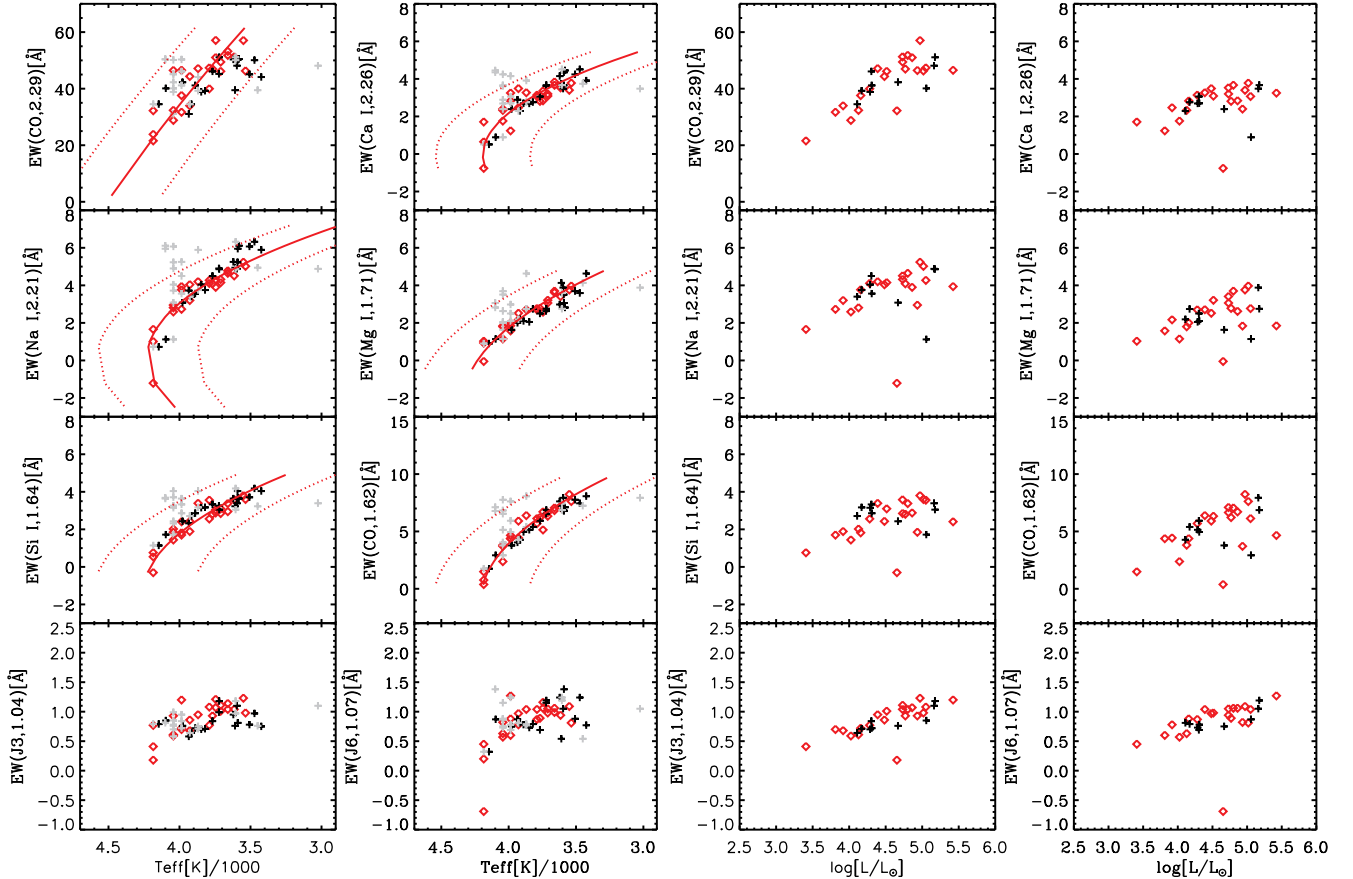


**Figure 11.** EW indicators of temperature. *Columns 1 and 2:* In each panel, red diamonds mark the EWs of reference RSGs with optical spectral type vs. the  $T_{\text{eff}}$ , as estimated by Messineo & Brown (2019) with the scale of Levesque et al. (2005). Most of these stars come from the sample of Keenan & McNeil (1989), as listed in Table 1. From top-left to bottom right, EWs from CO at  $2.29 \mu\text{m}$ , Ca at  $2.26 \mu\text{m}$ , Na at  $2.21 \mu\text{m}$ , Mg at  $1.71 \mu\text{m}$ , Si at  $1.64 \mu\text{m}$ , CO at  $1.62 \mu\text{m}$ , J3 at  $1.04 \mu\text{m}$ , and J6 at  $1.07 \mu\text{m}$ , respectively. Continuous red lines show 2nd order polynomial fits to the EWs of reference RSGs. Dashed red lines show the 2nd order polynomial fits shifted by  $\pm 350 \text{ K}$ . Crosses mark the EWs of other known RSGs, mostly with infrared spectral types (CaT or CO), in gray when using the literature  $T_{\text{eff}}$ , and in black when using the  $T_{\text{eff}}$  estimated in this work,  $T_{\text{combi}}$ . *Columns 3 and 4:* In each panel, the same EWs of RSGs are plotted vs. the stellar luminosities (Gaia EDR3 distances). Symbols are as in Columns 1 and 2.

of Keenan & McNeil (1989) and Levesque et al. (2005) are shown in Fig. 13. The estimated temperatures agree with those based on TiO (Levesque et al. 2005) with a  $\sigma$  of about 100 K. In conclusion, by using infrared EWs it is possible to accurately reproduce temperatures (within 150 K) which are consistent with those optically made. We followed the calibration of Levesque et al. (2005).

Note that the Levesque scale may be offset by 50 to 150 K. In the recent work of Tabernero et al. (2018), the relation between spectral types and stellar temperatures (based on TiO) is confirmed ( $R=10,000$ ), but the authors also confirmed a warmer temperature scale as suggested by Gazak et al. ( $R=3000$ , 2014b) and Davies et al. ( $R=4000-8000$ , 2015). The latter authors used a modeling of atomic lines in the  $J$ -band to infer metallicity and stellar temperatures. The scale of Tabernero et al. linearly correlates with that of Davies et al. (2015), but is 168 K cooler ( $\sigma=72 \text{ K}$ ). The scale of Levesque et al. is about  $220 \pm 100 \text{ K}$  (LTE models) cooler than that given in Gazak et al. (2014b) –  $270 \pm 130 \text{ K}$  with non-LTE models. These offset trends (hotter temperatures) are confirmed by the RSG parameters inferred by Arentsen et al. (2019) with spectra at  $R=10,000$ , though statistics is still poor with only 1 or 2 stars per spectral type (Table 7). The temper-

atures inferred with iron lines in  $Y$ -band by Taniguchi et al. ( $R=28,000$ , 2020) agree better with those of Levesque et al. (2005) with offsets from  $-91$  to  $+37 \text{ K}$ .

Future consistent modeling of atomic lines from the same element in multiple regions of the stellar spectrum (and for several elements) may help to solve the issue about the absolute scale, as well as improve the modeling itself.

For 14 RSGs from the IRTF library, temperatures and metallicities were estimated with a modeling of the  $J$ -band by Davies et al. (2010). But, at the SpeX resolution, temperatures were not well resolved and their estimates were  $153 \pm 167 \text{ K}$  cooler than those of Levesque.

### 6.1. Template temperature sequence for RSGs

We built a template sequence sorting our spectral atlas by increasing  $T_{\text{combi}}$  (see Tables 1, 2, and 3) and fortunately got a nice sequence of molecular absorption, as described in Sec. B. This sequence is useful for spectral typing in heavily obscured regions and for stellar population modeling work.

We have estimated spectroscopic stellar temperatures at infrared wavelengths (using only the  $H$  and  $K_s$  part of the spectrum) using the calibration of optical spectral-types based on TiO bands (Levesque et al. 2005). In Fig. 14, the strengths

**Table 7**  
Mean temperatures of RSGs per spectral type.

| Sp   | T(Lev) <sup>a</sup><br>[K] | T(Xsho) <sup>b</sup><br>[K] | T(Xsho)-T(Lev)<br>[K] | T(WIN) <sup>c</sup><br>[K] | T(WIN)-T(Lev)<br>[K] | T(IGRI) <sup>d</sup><br>[K] |
|------|----------------------------|-----------------------------|-----------------------|----------------------------|----------------------|-----------------------------|
| K0   | 4185                       | 4581 ± 56                   | 396                   | ..                         | ..                   | 4573                        |
| K1   | 4100                       | 4251 ± 46                   | 197                   | ..                         | ..                   | ..                          |
| K1.5 | 4057                       | ..                          | ..                    | 4073 ± 31                  | 15                   | ..                          |
| K2   | 4015                       | 4125 ± 44                   | 110                   | ..                         | ..                   | ..                          |
| K3   | 3956                       | 4024 ± 43                   | 47                    | 3940 ± 29                  | -16                  | ..                          |
| K4.5 | 3869                       | ..                          | ..                    | 3829 ± 61                  | -39                  | 4031                        |
| K5   | 3840                       | 3977 ± 53                   | 137                   | 3749 ± 49                  | -91                  | ..                          |
| M0   | 3790                       | 3868 ± 32                   | 78                    | ..                         | ..                   | ..                          |
| M1   | 3745                       | 3780 ± 62                   | 35                    | 3676 ± 117                 | -69                  | ..                          |
| M1.5 | 3710                       | 3747 ± 51                   | 37                    | 3747 ± 136                 | 37                   | ..                          |
| M2   | 3660                       | 3588 ± 59                   | -72                   | 3651 ± 31                  | -9                   | ..                          |
| M3   | 3605                       | 3768 ± 62                   | 163                   | ..                         | ..                   | ..                          |
| M4.5 | 3506                       | 3460 ± 57                   | -46                   | ..                         | ..                   | ..                          |

<sup>a</sup>=Average temperatures per spectral type Levesque et al. (2005).

<sup>b</sup>=Average temperatures per spectral type made with the XShooter spectral catalog of Arentsen et al. (2019).

<sup>c</sup>=Average temperatures per spectral type made with the WINERED catalog of Taniguchi et al. (2020).

<sup>d</sup>=Average temperatures per spectral type made with the IGRINS catalog of Park et al. (2018).

**Table 8**  
Average EWs per spectral type of the infrared indicators of temperature.

| Sp   | T <sub>eff</sub><br>[K] | [CO, 2.29]<br>[Å] | σ<br>[Å] | [Ca I, 2.26]<br>[Å] | σ<br>[Å] | [Na I, 2.21]<br>[Å] | σ<br>[Å] | [Mg I, 1.71]<br>[Å] | σ<br>[Å] | [Si I, 1.64]<br>[Å] | σ<br>[Å] | [CO, 1.62]<br>[Å] | σ<br>[Å] |
|------|-------------------------|-------------------|----------|---------------------|----------|---------------------|----------|---------------------|----------|---------------------|----------|-------------------|----------|
| K0   | 4185                    | 25.9              | 5.6      | 0.5                 | 1.2      | 0.5                 | 1.5      | 0.6                 | 0.6      | 0.3                 | 0.6      | 0.9               | 0.6      |
| K2   | 4043                    | 35.9              | 9.3      | 2.2                 | 0.4      | 2.8                 | 0.2      | 1.6                 | 0.4      | 1.8                 | 0.3      | 3.3               | 0.8      |
| K4   | 3927                    | 39.2              | 7.3      | 3.0                 | 0.7      | 3.6                 | 0.6      | 2.3                 | 0.2      | 2.2                 | 0.4      | 5.2               | 1.0      |
| M0   | 3790                    | 43.7              | 5.2      | 3.1                 | 0.0      | 4.2                 | 0.1      | 2.7                 | 0.0      | 3.1                 | 0.7      | 5.9               | 0.3      |
| M1   | 3745                    | 54.1              | 4.3      | 3.1                 | 0.4      | 4.1                 | 0.3      | 2.6                 | 0.0      | 3.0                 | 0.1      | 5.9               | 1.1      |
| M1.5 | 3710                    | 47.8              | 2.3      | 3.1                 | 0.1      | 4.2                 | 0.1      | 3.1                 | 0.1      | 3.0                 | 0.2      | 6.5               | 0.2      |
| M2   | 3660                    | 52.5              | 1.0      | 3.8                 | 0.1      | 4.7                 | 0.1      | 3.7                 | 0.1      | 3.2                 | 0.3      | 6.9               | 0.2      |
| M3.5 | 3550                    | 57.1              | ..       | 3.4                 | ..       | 5.2                 | ..       | 3.8                 | ..       | 3.8                 | ..       | 8.2               | ..       |
| M4   | 3535                    | 46.3              | ..       | 3.8                 | ..       | 5.0                 | ..       | 4.0                 | ..       | 3.6                 | ..       | 7.6               | ..       |

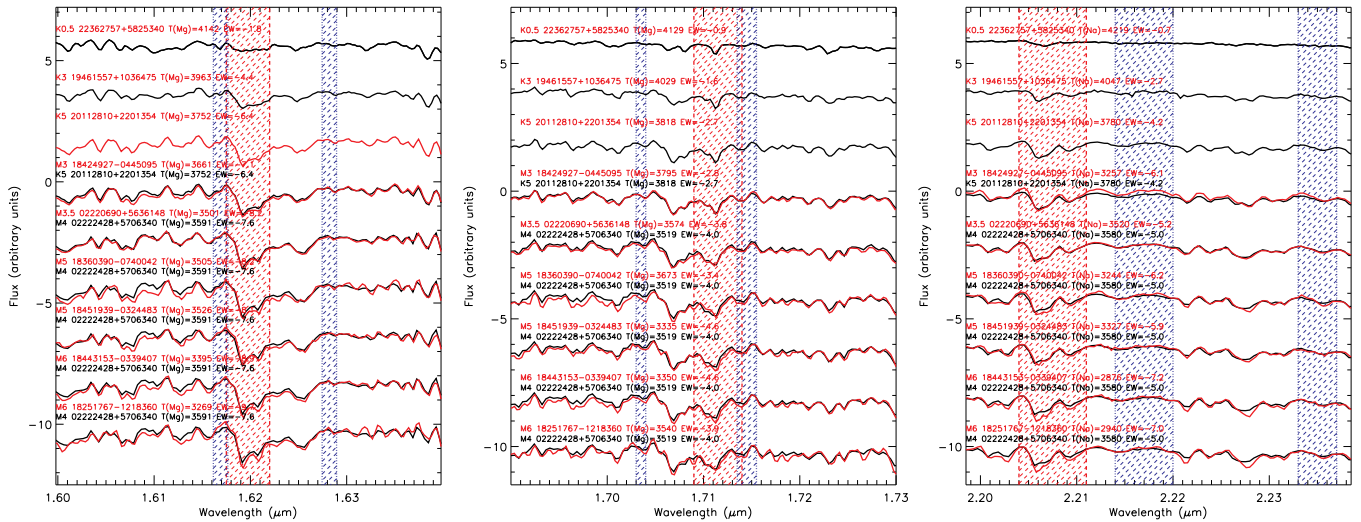


**Figure 12.** Examples of spectral features due to CO at 1.62  $\mu\text{m}$  (left panel), Mg at 1.71  $\mu\text{m}$  (central panel), Na at 2.2  $\mu\text{m}$  (right panel).

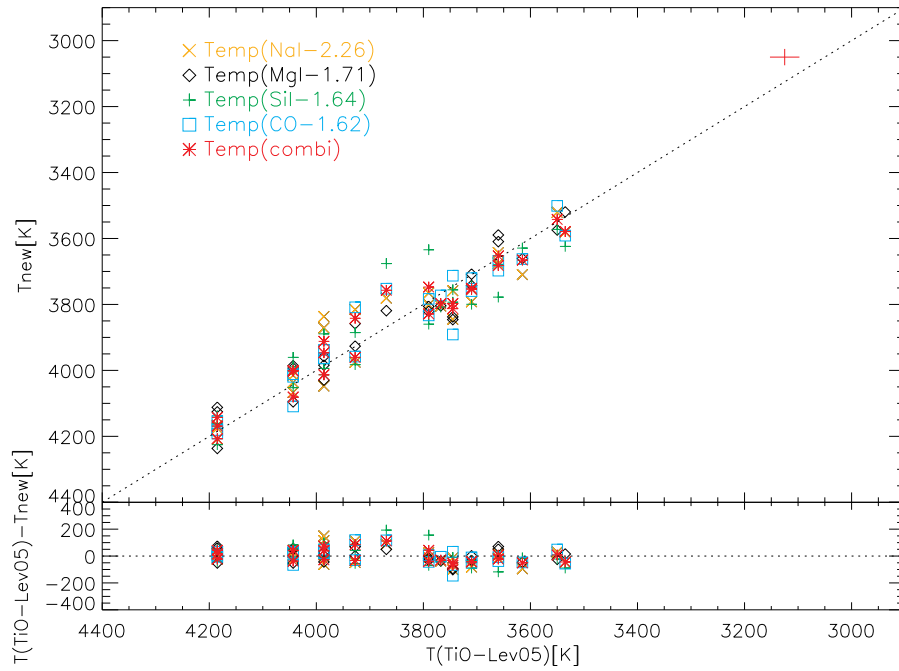


**Figure 13.** In the top panel, the infrared temperatures estimated with a 2nd order polynomial fitting of the EWs are plotted vs. the  $T_{\text{TiO}}$  temperatures (inferred from the optical spectral types and the temperature scale of Levesque et al. (2005)). Orange crosses mark temperature estimates from Na I at  $2.26 \mu\text{m}$ , black diamonds those from Mg I at  $1.71 \mu\text{m}$ , green pluses those from Si I at  $1.64 \mu\text{m}$ , cyan squares those from CO at  $1.62 \mu\text{m}$ , and red asterisks refer to an average temperature ( $T_{\text{combi}}$ ) from NaI, MgI, SiI, and CO at  $1.62 \mu\text{m}$ . The identity line is marked with a dashed line. The vertical segment of the red cross shows the  $\sigma$  of the  $T_{\text{combi}} - T(\text{TiO})$  differences, while the horizontal segment is the average difference between the temperatures of two spectral types, e.g. K4 and K5. In the lower panel, the temperature differences are plotted vs. the  $T_{\text{TiO}}$  temperatures.

of the TiO band heads at  $0.88 \mu\text{m}$  appear to correlate with  $T_{\text{combi}}$ , and with the [Mg I, 1.71] and [CO, 1.62] measured in the SpeX spectra. The TiO strength is estimated by fitting a linear continuum and measuring the depth of the TiO absorption from  $0.8857 \mu\text{m}$  to  $0.9099 \mu\text{m}$ .

In Fig. 15, we plot the temperatures versus the  $(J-K_s)_o$  colors, and it appears that water absorption dominates the colors redder than 1.3 mag. For comparison, we overplot the empirical relation between the  $(J-K_s)_o$  colors and the spectral types by Koornneef (1983) by using the temperature scale of Levesque et al. (2005), as well as by using the temperatures inferred from the work of Arentsen et al. (2019). For K-type stars, the theoretical temperatures obtained with models of atmospheres by Neugent et al. (2020) remain higher, up to about 400 K, than that estimated with the empirical relation of Koornneef (1983); for M-types, the models predict temperatures up to 150 K cooler.

## 7. METALLICITY OF RSGS

RSG stars are a young population of the Galactic disk, which has high metallicity. Metallicity measurements for only 25 of the known RSGs included in this work are reported in the literature (Davies et al. 2010; Gazak et al. 2015; Arentsen et al. 2019; Prugniel et al. 2011; Stevens et al. 2017; Anderson & Francis 2012; Soubiran et al. 2016; Ivanov et al. 2004; Davies et al. 2009). Their values range from  $-0.2$  dex to  $+0.35$  dex (see Appendix A). 16 out of these 25 measurements have been made in  $J$ -band (Davies et al. 2010; Gazak et al. 2015). Davies et al. (2010) used some spectra of RSGs from the IRTF library to study atomic lines in  $J$ -band, from  $1.15 \mu\text{m}$  to  $1.23 \mu\text{m}$ . The authors located several iron-dominated lines that **allowed** the measurement of a global metallicity with an accuracy of 0.1 dex with synthetic spectra. In this paper, we only present the new spectra and empirical quantities. Metallicity determinations with synthetic spectra will be presented elsewhere.

The FeI-1.1611, FeI-1.1641, FeI-1.1887, FeI-1.976 lines of Davies et al. (2010) correspond to the J12, J13, J17, and J18 lines in Table 4, respectively. Theoretically, the strengths of these lines, with the exception of FeI-1.1641 (J17), are expected to increase with increasing metallicity and to be almost independent of temperature; observationally, no clear relation is found between the EWs and the metallicity. This is likely due to the spectral resolution of SpeX and the narrow range of Galactic metallicity of RSGs. When separating the stars in K-type and M-type stars, the EWs of the FeI-1.1641 lines (J17) and FeI-1.976 (J18) appear larger in stars with super-solar metallicity; as shown in Fig. 16, stars with  $[J17] > 2 \text{ \AA}$  are supersolar. We found also an interesting behavior of the EW of the J22 line, which is an unblended line from Mn I at  $1.29 \mu\text{m}$ ; for RSGs below  $\log(Z) < 0.16$ ,  $[J22]$  values appear approximately constant ( $0.96 \pm 0.04 \text{ \AA}$ ); above that  $Z$ , EWs are larger ( $1.15 \pm 0.07 \text{ \AA}$ ), similarly to the findings of Feltzing et al. (2007) for thin Disc stars.

## 8. NOTES ON INDIVIDUAL STARS

Optical spectral types from Keenan & McNeil (1989) are reproduced within one spectral type. EWs from Na I, Mg I, Si I, and CO at  $1.62 \mu\text{m}$  yield spectral types in better agreement with the optical ones than those estimated only from the CO band heads at  $2.29 \mu\text{m}$ . For example, 2MASS J18082651–1833078 (HD 165782) is an optical K0 Ia star; from the CO at  $2.29 \mu\text{m}$ , we estimated a K2.5 type, while

by using Na I, Mg I, Si I, and CO at  $1.62 \mu\text{m}$ , we obtain a K0.5 type. 2MASS J07473853–1559263 (HD 63302) is reported in optical works as a K1-2 supergiant. By using the [CO, 2.29] we infer an M0 type, while by using Na I, Mg I, Si I, and CO at  $1.62 \mu\text{m}$ , we obtain a K2.5 type. 2MASS J17143885+1423253 (HD 156014) is a known M5 Ib-II star, a possible AGB (Moravveji et al. 2013); the CO at  $2.29 \mu\text{m}$  yields a K4.5 type (RSG) or M5.5 (giant); from  $T_{\text{combi}}$  we infer an M3. 2MASS J20285059+3958543/RW Cygn is optically an M3, but its infrared EWs are more typically of an M1.5 star. 2MASSJ 22543171+6049388/MY Cep is reported as an M7.5 I star from Fawley & Cohen (1974), but we estimated an M3.

For stars previously classified via CO band heads or TiO at  $0.8 \mu\text{m}$ , we determined spectral types later than those reported in the literature, up to 5 spectral types, and, therefore, cooler temperatures. For example, 2MASS J18424927–0445095 was classified by Negueruela et al. (2012) and listed as a K1 Iab star. From the CO band heads at  $2.29 \mu\text{m}$  we derived an M1 star, while from the average infrared temperature an M3 type. We observed this star twice to be sure of the acquisition. In Fig. 15, the literature temperatures and  $T_{\text{combi}}$  are plotted versus the dereddened  $J-K_s$  colors,  $(J-K_s)_o$ , which are not affected by TiO bands, putting in evidence those stars with discrepant spectral types in the literature.

2MASS J17143885+1423253/HD 156014/ $\alpha$  Her is an outlier data point in our [Mg I, 1.71] versus [CO, 2.29] diagram in Fig. 3. It is classified as an M5 Ib-II by Keenan & McNeil (1989) and as a M5 I by Levesque et al. (2005). The location on the [CO, 2.29] versus [Mg I, 1.71] giant sequence, weak CN band heads, are suggestive of a lower luminosity class (III-II). The star is variable (SRC) and Yamashita (1967) lists different classes for different epochs (IIIa, IIab, Ib). Moravveji et al. (2013) modeled  $\alpha$  Her as a thermal pulsing AGB of about  $2 M_{\odot}$ .

2MASS J18345133–0713162 and 2MASS J18345840–0714247, listed in Table 1, were marked as possible RSGs in the cluster Alicante 8 near RSGC1 by Negueruela et al. (2010). Because of the strong TiO bands and water absorption, their spectra resemble those of Mira AGBs. Furthermore, these stars have low radial velocity ( $9.37$  and  $-11.79 \text{ km s}^{-1}$ ), while the RSGC clusters are at  $V_{\text{LSR}}$  from  $90$  to  $120 \text{ km s}^{-1}$  (e.g. Davies et al. 2007, 2008; Origlia et al. 2016). For 2MASS J18345133–0713162 we estimated  $M_{\text{bol}} = -1.27$  mag, typical of AGB.

2MASS J00403044+5632145/HD 3712/ $\alpha$  Cas is listed in our Table 3 of known giants; Keenan & McNeil (1989) reported it as a K0 IIIa star. In previous years, from 1938 to 1968, it had been classified as class II-III (e.g., Meisel 1968). The [CaT] is  $\approx 9 \text{ \AA}$ , and in the [CO, 2.29] versus [Mg I, 1.71] diagram it is located near two RSGs, with a Mg I line at  $1.71 \mu\text{m}$  significantly fainter than in other giants. 2MASS J00403044+5632145 has  $\log(L/L_{\odot})$  (Gaia EDR3)=2.83. Stock et al. (2018) estimated a similar luminosity and a 93% probability that it is a star in the horizontal branch phase with  $\log(g)=1.7$  and  $[Fe/H] = -0.1$  dex (e.g., Anderson & Francis 2012), and Kervella et al. (2019) report it as a possible binary system.

## 9. APPLICATIONS OF THE NEW SPECTROSCOPIC DIAGNOSTICS

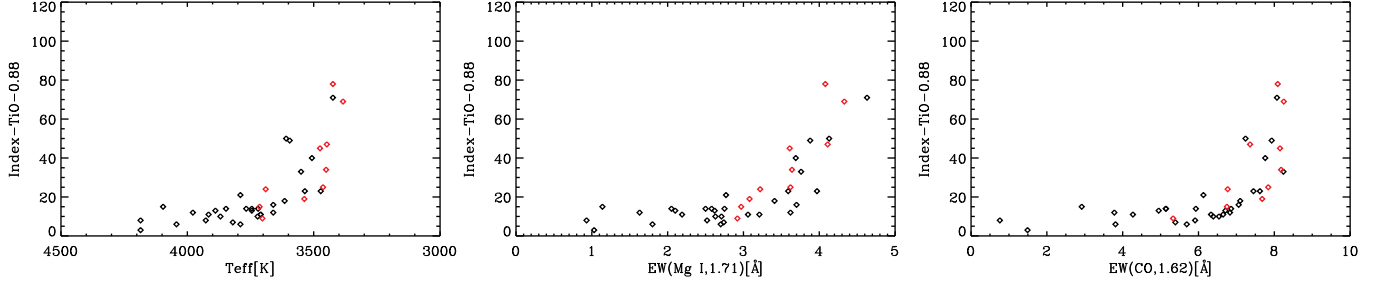


**Figure 14.** *Left panel:* Index for the strengths of the TiO band heads at  $0.88 \mu\text{m}$  vs.  $T_{\text{combi}}$  (the  $T_{\text{eff}}$  estimated from the SpeX spectra with  $H$ - and  $K$ -band lines). *Middle panel:* Index for the strengths of the TiO band heads at  $0.88 \mu\text{m}$  vs.  $[\text{Mg I}, 1.71]$ . *Right panel:* Index for the strengths of the TiO band heads at  $0.88 \mu\text{m}$  vs.  $[\text{CO}, 1.62]$ .

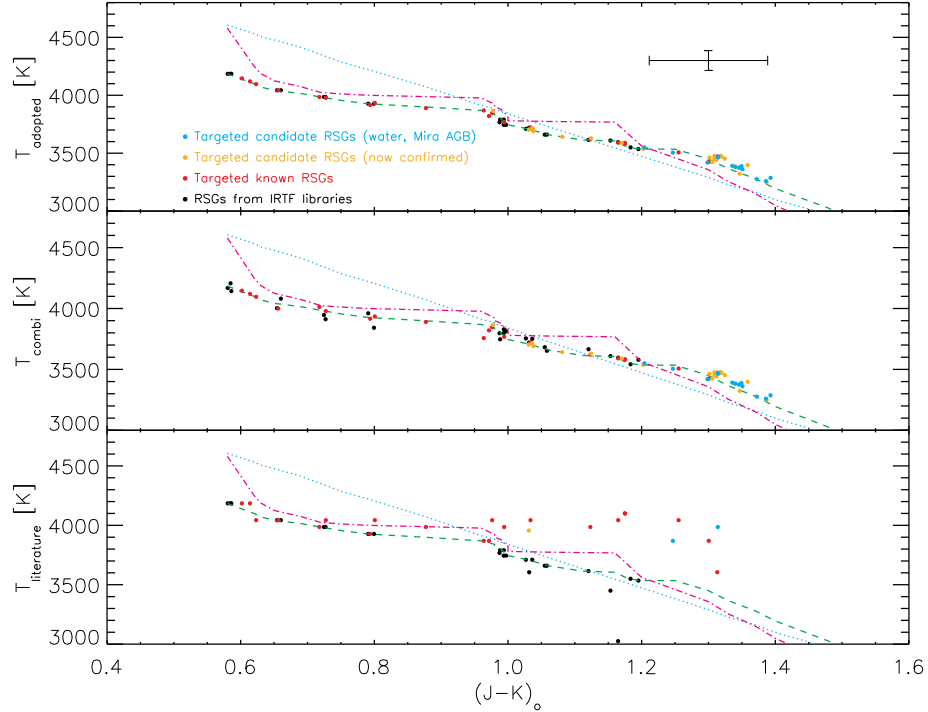


**Figure 15.**  $(J-K_s)_0$  colors vs. stellar temperatures (dereddening was done with the intrinsic colors of Koornneef 1983). *In the bottom panel,* we used the  $T_{\text{eff}}$  estimated from the literature ( $T_{\text{eff}}$  are estimated with collected spectral types and the temperature scale of Levesque et al. 2005). *In the middle panel* the  $T_{\text{combi}}$  estimated with the SpeX spectra. *In the top panel,* we use the literature values for well-known RSGs optically analyzed, e.g., by Keenan & McNeil (1989) and Levesque et al. (2005), and our  $T_{\text{combi}}$  for other stars (mostly infrared classified stars), as listed in Table 1. The average 2MASS  $J-K_s$  error and temperature error is marked on the top-right corner. The data points are colored as described in the legend; black circles indicate data points of RSGs with spectra in the SpeX libraries; red circles mark known RSGs observed during our runs, and orange and cyan circles candidate RSGs with and without water absorption, respectively. The dashed green curve is the relation between spectral-types and  $J-K$  colors of Koornneef (1983) converted to temperatures with the scale of Levesque et al. (2005). The long-dashed magenta curve shows the relation between the  $J-K$  colors of Koornneef (1983) and the average temperatures per spectral type of Arentsen et al. (2019) that are listed in Table 7. The cyan dotted line is the relation between temperatures and  $J-K$  colors predicted with atmosphere models by Levesque et al. (2005) and Neugent et al. (2020).

We observed 42 candidate RSGs, which had been identified with a 2MASS-GLIMPSE color selection, as described in Messineo et al. (2017) and Messineo et al. (2012). In our previous work, low-resolution  $H$ -band and  $K$ -band observations ( $R=1000$ ) enabled us to conclude that at least 50% of this sample was made of RSGs later than M0 type.

One of the targets (2MASS J18355534-0738197) turned out to be of F3-F6 type.

The remaining 41 candidates are late-type stars (K and M). By comparing their spectral features with those of known RSGs in Table 1, we spectroscopically classify the candidate

stars of Table 2, by assigning spectral types and luminosity classes. We used the locations on the Mg I versus CO diagram, the absence of strong water absorption, and, for bluer sources detected from  $0.9$  to  $1.1 \mu\text{m}$ , the strengths of the  $[\text{J}12+\text{J}17+\text{J}18]$ , along with strong  $[\text{J}8+\text{J}9+\text{J}10]$ , and the absence of TiO band heads at  $1.1 \mu\text{m}$ . For sources detected only long ward of  $1.3 \mu\text{m}$ , we used the  $[\text{J}21+\text{J}22]$ , and strength of the Si I line at  $1.59 \mu\text{m}$ . The infrared EWs enable us to spectroscopically classify 50% (21 stars) of the late-type targets as secure M I and one K5 I.

The EWs of the candidate RSGs are shown in Fig. 17.

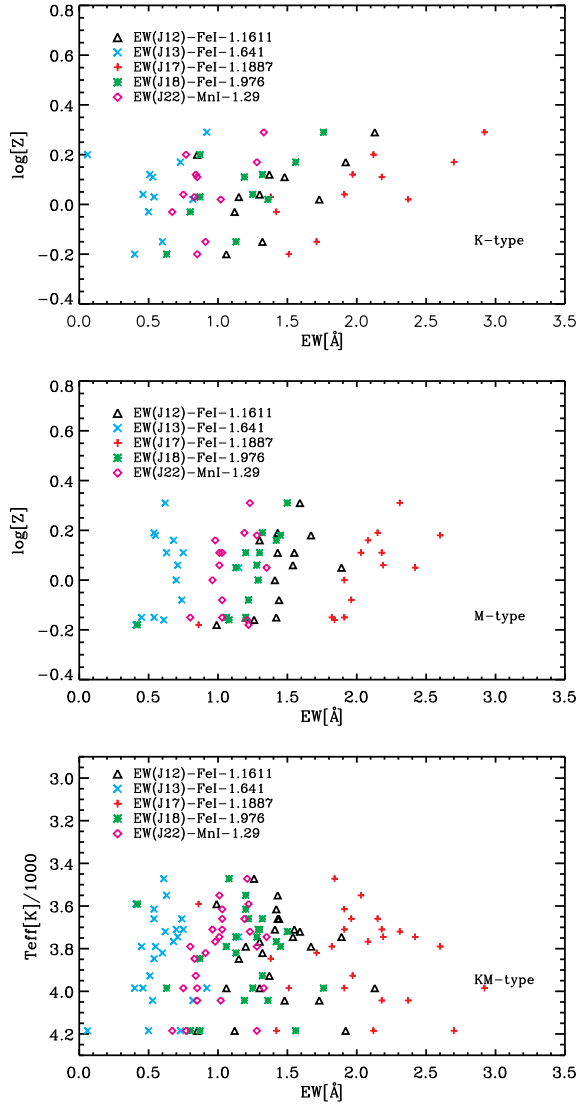


**Figure 16.** *Top Panel* : Log( $Z$ ) values for Galactic RSGs (see text) vs. the measured EWs of possible indicators of metallicity (the J12, J13, J17, J18, and J22 lines), as described in the legend; only known K-type RSGs ( $> 3800$  K) are plotted. *Middle Panel* : as in the top panel, only known M-type RSGs ( $< 3800$  K) are plotted. *Bottom Panel* : Stellar effective temperatures ( $T_{\text{eff}}$  from Table 1) of the RSGs plotted in the above panels vs. EWs.

The spectra of the targets 2MASS J18104421–1929072, 2MASS J18334070–0750531, and 2MASS J18444023–0315329 are anomalous (Fig. B). They have strong TiO band heads at  $1.1 \mu\text{m}$  (like in the spectra of known O-rich Mira AGB stars), but without water absorption. They also have VO absorption. Furthermore, we see strong TiO band heads at  $0.92\text{--}0.94 \mu\text{m}$  and weak ZrO band heads at  $0.930\text{--}0.936 \mu\text{m}$ .

The spectrum of 2MASS J18360390–0740042 displays a small [Mg I, 1.71] and a small [Si I, 1.59], but a strong [CO], resembling the spectrum of an S-type.

32% (13 stars) of the late-type targets have visible water absorption in their spectra. Their features are consistent with being Mira AGBs. For example, they have strong CO at  $2.29 \mu\text{m}$ , a weak Si I line at  $1.59 \mu\text{m}$ , and their [J12+J17+J18] values are below the threshold for RSGs (see Fig. 17). Among

them, eight spectra display TiO band heads at  $1.1 \mu\text{m}$ , and three stars also show strong TiO band heads at  $0.92\text{--}0.94 \mu\text{m}$ . We only cast some doubts on the classification of 2MASS J18105174–1947374, and 2MASS J18251767–1218360 because, besides water and strong TiO band heads at  $1.1 \mu\text{m}$ , they also have visible CN band heads at  $1.09\text{--}1.1 \mu\text{m}$ .

For three stars (2MASS J18341160–0940545, 2MASS J18570375+0152049, and 2MASS J18253811–1306250), the analyzed spectra do not cover the TiO bands at  $1.1 \mu\text{m}$  and  $0.92 \mu\text{m}$ . For the spectra of 2MASS J18391007–0655526 and 2MASS J19293750+1758006, the coverage and signal-to-noise, allow us to detect only VO absorption, which suggests Mira AGBs.

The remaining three unclassified stars are 2MASS J18363595–0718472, 2MASS J18353576–0811451, 2MASS J18153105–1744228 and have late M-types. 2MASS J18363595–0718472 is an O-rich star with strong VO absorption and visible CN band heads, without strong water absorption (the CaT and TiO at  $0.88\text{--}0.92 \mu\text{m}$  spectral regions were not extracted); it has stronger Mg I at  $1.71 \mu\text{m}$  than most RSGs with similar CO band heads at  $2.29 \mu\text{m}$ . In the spectrum of 2MASS J18153105–1744228, there is no visible water absorption, but the plot of Mg I at  $1.71 \mu\text{m}$  versus CO shows strong Mg I at  $1.71 \mu\text{m}$ . In the spectrum of 2MASS J18353576–0811451, the first measured index is J21, there is no water absorption, but, in contrast to the majority of RSGs, it has a weak Si I at  $1.59 \mu\text{m}$  and a weak [J22].

### 9.1. Luminosities and distances of candidate RSGs

In order to check the spectroscopic classification of the 41 candidate RSGs, we estimated their bolometric magnitudes, which are listed in Table 2 (see also Sect. 4.1). In the Gaia EDR3 catalog, parallaxes are available for 19 candidates, with only two data points with fractional errors smaller than 25%. Therefore, we estimated their near-kinematic distances by using the  $V_{\text{LSR}}$  values and the Galactic rotation curve of (Reid et al. 2014). For each star, we adopted the  $V_{\text{LSR}}$  values from the Gaia DR2 catalog Gaia Collaboration et al. (2020), when available, or the values from Kharchenko et al. (2007) otherwise, those measured from our SpeX measurements. We estimated the errors on distances by assuming a SpeX velocity uncertainty of  $22 \text{ km s}^{-1}$ , which is the  $\sigma$  of the differences between the Gaia DR2  $V_{\text{LSR}}$  values and the  $V_{\text{LSR}}$  from SpeX data. Most of the candidates are at distances larger than  $3.5 \text{ kpc}$  from us (near-kinematic distances).

By considering the 18 known RSGs in Table 1 with good Gaia EDR3 distances (parallax fractional error smaller than 25%) and kinematic distance errors  $< 900 \text{ pc}$ , we obtained a mean difference between the Gaia distances and kinematic distances of  $-334 \text{ pc}$  with a  $\sigma$  of  $710 \text{ pc}$ . For RSGs in Table 1 reported in Messineo & Brown (2019) and Levesque et al. (2005) as members of stellar associations, the mean difference between the stellar association distances by Levesque et al. (2005) and the Gaia individual distances is  $-107 \text{ pc}$  with a  $\sigma = 333 \text{ pc}$ ; while the mean difference between the stellar association distances and the kinematic distances is  $176 \text{ pc}$  with  $\sigma = 858 \text{ pc}$ .

20 (out of 21) candidates that spectroscopically meet the properties of supergiants, are shown in the  $M_{\text{bol}}$  versus  $T_{\text{eff}}$  diagram of Fig. 18. Their  $\log(L/L_{\odot})$  estimated from the EWs differs from the photometric estimates by  $+0.18$  with  $\sigma = 0.50$ . While eight have spectral types from K5 to M4, which are typical of RSGs (Messineo & Brown 2019), nine



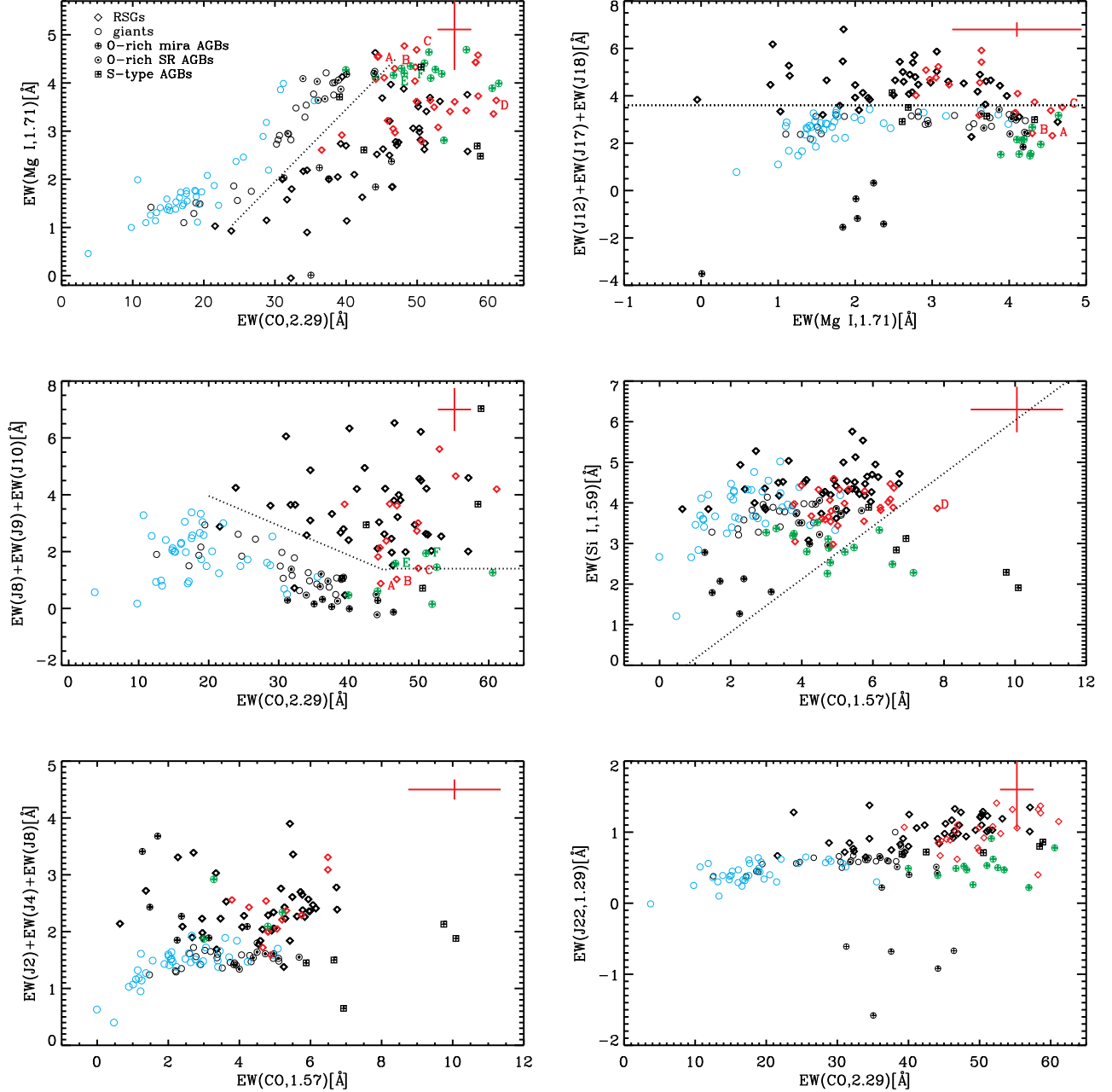


**Figure 17.** Useful diagrams to classify evolved late-type stars as presented in Figs. 3, 4, and 5 (same symbols). The EW values of observed candidate RSGs with no water absorption ( $< 6.6\%$ ) from Table 2 are over-plotted with red diamonds. The locations of the peculiar 2MASS J18444023–0315329 (A), 2MASS J18104421–1929072 (B), 2MASS J18334070–0750531 (C), and 2MASS J18360390–0740042 (D), which are discussed in the text, are marked. The EW values of the targeted late-type stars in Table 2 found to have water absorption ( $> 6.6\%$ ), and 2MASS J18345133–0713162 (E) and 2MASS J18345840–0714247 (F) from Table 1 are over-plotted with green encircled crosses.

have M5 types, but their luminosities are still compatible with that of RSGs within the margin of uncertainty. Three have extremely late types (M5.5–M6) and are located in the area where massive AGBs and super AGBs may reside (5–9  $M_{\odot}$ , e.g., Messineo & Brown 2019; Shetye et al. 2019). Stellar evolution and threshold masses of AGBs and RSGs is another chapter of astronomy still *“in fieri”*. Therefore, detections of these stars are **highly desirable**. Precisely because going from luminosity classes to **physical properties like internal types of nuclear burning and stellar structures, high-resolution investigation of s-process products is required**

(e.g., Shetye et al. 2020), and larger statistics. In 2022, Gaia DR4 will provide improved distances and spectral types for millions of Galactic stars.

## 10. SUMMARY OF ANALYZED INFRARED DIAGNOSTICS FOR RSGS

The spectroscopic issue we have investigated here is the building up of a reference frame of EWs at a medium resolution that allows us to distinguish Galactic giants and RSGs from  $K$ - to  $M$ -types, using the IRTF spectral library.

We have confirmed that with the IRTF/SpEx spectra at

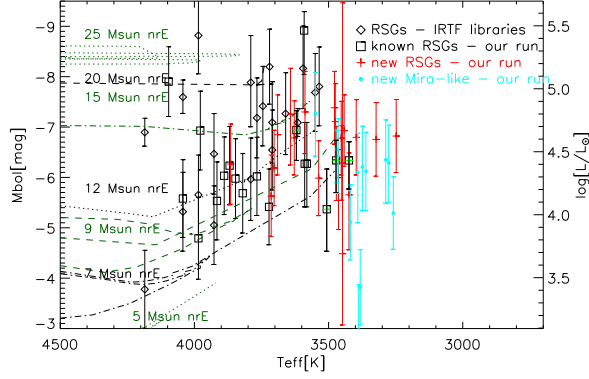


**Figure 18.** *Top panel:* Bolometric magnitudes vs.  $T_{\text{eff}}$ .  $T_{\text{eff}}$  are from previous works if optically derived (see Table 1), or our  $T_{\text{combi}}$ . For comparison, we add some non-rotating stellar tracks with solar metallicity by Ekström et al. (2012). The green dotted line at the bottom indicates a track of a  $5 M_{\odot}$  star (90-110 Myr). the black dotted-dashed curve that of a  $7 M_{\odot}$  star (42-49 Myr); the green long-dashed curve marks a  $9 M_{\odot}$  track (27-30 Myr); the black dotted curve a  $12 M_{\odot}$  track (16-18 Myr); the green dotted-dashed curve shows a  $15 M_{\odot}$  track (14-15 Myr); the black long-dashed curve a  $20 M_{\odot}$  track (8.5 Myr), and the top green dotted line that of a  $25 M_{\odot}$  (6.7 Myr). For known RSGs, the absolute  $M_{\text{bol}}$  magnitudes are obtained with parallactic distances from Gaia EDR3, when their fractional errors are  $< 25\%$ ; in order to include a sample of faraway known late-M supergiants, for larger parallactic errors and  $V_{\text{LSR}} > 70 \text{ km s}^{-1}$ , near-kinematic distances are used. For the newly detected RSGs, which have only one parallax within the desired constraints, we use the near-kinematic distances. Plotted data points and symbols are as explained in the legenda. The four known late-M RSGs 2MASS J18392036+0601426 (RSGC2-14), 2MASS J18391505+0605191 (RSGC2-17) 2MASS J18451939+0324483 (RSGC3-S6), and 2MASS J18333780+0921380 (MMF2014-44) are marked with a green cross.

$R=2000$  it is possible to separate red giants and supergiants in several diagrams and to identify contaminant AGBs.

- By using the  $[\text{CO}, 2.29]$  values and of  $[\text{Mg I}, 1.71]$  values, it is possible to distinguish giants from RSGs down to K0 type ( $[\text{CO}, 2.29] \approx 22 - 30 \text{ \AA}$ , as shown in Fig. 3). About 95% of known RSGs show Mg I lines significantly weaker than those of giants. So far, at medium resolution, the infrared identification of RSGs has been based uniquely on the CO band heads at  $2.29 \mu\text{m}$ , which has allowed us to detect M-type RSGs with  $[\text{CO}, 2.29] \gtrsim 45 \text{ \AA}$  (M0).
- A distinctive feature of Mira AGBs is a strong water vapour absorption in  $H$  and  $K$ -band. This occurs rarely in RSGs. Only 6.5% of the spectra of previously known RSGs is featured with water absorption above  $> 6.6\%$ , mimicking O-rich Mira AGBs (see Appendix Fig. C).
- In addition to the Si I at  $1.59 \mu\text{m}$  already mentioned by Origlia et al. (1993), the J12, J17, J18, J21, J22 are found to be good indicators of luminosity classes (see Figs. 7 and 8). By combining the indices, for example, J12 and J21, stars with  $[\text{J21}+\text{J22}] > \approx 2.4 \text{ \AA}$  are found to be uniquely RSGs. These are undoubtedly optimal indicators of luminosity class capable of identifying supergiants from K to late M-types in  $J$ -band. O-rich Mira AGB stars behave in a similar way to giants.
- The J9 and J10 lines in  $Y$ -band are dominated by CN band heads and are visibly stronger in RSGs than in

giants of similar temperatures (Fig. 5). O-rich Mira AGB stars and normal giants have EWs smaller than RSGs.

- The spectra of contaminant S-type stars have weaker Si I lines at  $1.59 \mu\text{m}$ , Si I lines at  $1.0588 \mu\text{m}$  (J4), and Si I at  $1.078 \mu\text{m}$  (J8) than those of RSGs (Fig. 6).
- Spectral types consistent with those from the optical classification are obtained by comparison with the Na I at  $2.21$ , Mg I at  $1.71 \mu\text{m}$ , Si I at  $1.64 \mu\text{m}$ , CO at  $1.62 \mu\text{m}$  of well-known RSGs (Fig. 11). Typically they are accurate within 1-2 spectral types.
- When sorting the spectra by the estimated spectral types/temperatures, we find a nice sequence of dominant molecules with spectral types. For example, ZrO and VO appear in RSGs with spectral types later than M3 ( Appendix Figs. B and C).
- Only five K0-2 RSGs are in the IRTF library and one in the extended IRTF library. We observed 21 other known RSGs, 20 of which with quoted K-types. Unfortunately, only 11 were found to be K-types. 2MASS J22362757+5825340 (W Cep) is a K0 I, while 2MASS J22495897+6017567 and 2MASS J21440431+5342116 are K1-K2 I.
- We used these RSGs' features to spectroscopically classify 41 newly targeted late-type stars. We found that 28 out of 41 candidates (68%) have a low water content ( $< 6.6\%$ ), and we assigned 21 candidates (51 %) to class I because of their location in the  $[\text{Mg I}, 1.71]$  versus  $[\text{CO}, 2.29]$  diagram, of their  $[\text{J12}+\text{J17}+\text{J18}]$  and  $[\text{J8}+\text{J9}+\text{J10}]$  values, which are typical of RSGs. 13 out of 41 (32%) have water absorption ( $> 6.6\%$ ), of which 23% have also strong TiO features at  $0.93$ , and 62% have TiO features at  $1.1 \mu\text{m}$ . The  $1.1 \mu\text{m}$  band head is always seen in Mira AGBs. Their locations in the diagrams are consistent with those of known O-rich Mira stars.
- In conclusion, our 72 observed targets consist of 9 giants, 21 already known RSGs, and 42 candidate RSGs. Of the 21 previously known RSGs, 19 are reclassified as spectroscopic RSGs, while two stars (2MASS J18345840+0714247, and 2MASS J18345133+0713162) appear to be Mira AGBs. Among the candidate RSGs, we are able to confirm 21 RSGs.

These infrared results are particularly useful for defining new and focused studies of the inner Galaxy, where optical spectroscopy is strongly hampered by dust obscuration, with  $A_V$  extinction up to 40 magnitudes, and where most of the Galactic mass resides.

Furthermore, we have located an unblended line useful to map the Galactic abundance of Mn I at  $1.29 \mu\text{m}$ . Only six stars (out of the 96 in Table 5) are particularly rich in Mn I (three RSGs from the IRTF library, three from our observations).

## REFERENCES

- Adams, W. S., Joy, A. H., Humason, M. L., & Brayton, A. M. 1935, ApJ, 81, 187

- Alexander, M. J., Kobulnicky, H. A., Clemens, D. P., et al. 2009, *AJ*, 137, 4824
- Alvarez, R., Lançon, A., Plez, B., & Wood, P. R. 2000, *A&A*, 353, 322
- Anderson, E. & Francis, C. 2012, *Astronomy Letters*, 38, 331
- Arentsen, A., Prugniel, P., Gonneau, A., et al. 2019, *A&A*, 627, A138
- Bertelli, G., Nasi, E., Girardi, L., & Marigo, P. 2009, *A&A*, 508, 355
- Bessell, M. S., Castelli, F., & Plez, B. 1998, *A&A*, 333, 231
- Bidelman, W. P. 1957, *PASP*, 69, 326
- Blum, R. D., Ramírez, S. V., Sellgren, K., & Olsen, K. 2003, *ApJ*, 597, 323
- Blum, R. D., Sellgren, K., & Depoy, D. L. 1996, *AJ*, 112, 1988
- Boulon, J. 1963, *Journal des Observateurs*, 46, 243
- Cantat-Gaudin, T., Jordi, C., Vallenari, A., et al. 2018, *A&A*, 618, A93
- Cardelli, J. A., Clayton, G. C., & Mathis, J. S. 1989, *ApJ*, 345, 245
- Cesetti, M., Pizzella, A., Ivanov, V. D., et al. 2013, *A&A*, 549, A129
- Chiavassa, A., Pasquato, E., Jorissen, A., et al. 2011, *A&A*, 528, A120
- Chieffi, A. & Limongi, M. 2013, *ApJ*, 764, 21
- Chun, S.-H., Yoon, S.-C., Jung, M.-K., Kim, D. U., & Kim, J. 2018, *ApJ*, 853, 79
- Clark, J. S., Negueruela, I., Davies, B., et al. 2009, *A&A*, 498, 109
- Comerón, F., Torra, J., Chiappini, C., et al. 2004, *A&A*, 425, 489
- Cushing, M. C., Vacca, W. D., & Rayner, J. T. 2004, *PASP*, 116, 362
- Davies, B., Figer, D. F., Kudritzki, R.-P., et al. 2007, *ApJ*, 671, 781
- Davies, B., Figer, D. F., Law, C. J., et al. 2008, *ApJ*, 676, 1016
- Davies, B., Kudritzki, R.-P., & Figer, D. F. 2010, *MNRAS*, 407, 1203
- Davies, B., Kudritzki, R.-P., Gazak, Z., et al. 2015, *ApJ*, 806, 21
- Davies, B., Kudritzki, R.-P., Lardo, C., et al. 2017, *ApJ*, 847, 112
- Davies, B., Origlia, L., Kudritzki, R.-P., et al. 2009, *ApJ*, 696, 2014
- de Burgos, A., Simon-Díaz, S., Lennon, D. J., et al. 2020, *A&A*, 643, A116
- de Jong, R. S., Bellido-Tirado, O., Chiappini, C., et al. 2012, in *Society of Photo-Optical Instrumentation Engineers (SPIE) Conference Series*, Vol. 8446, *Ground-based and Airborne Instrumentation for Astronomy IV*, ed. I. S. McLean, S. K. Ramsay, & H. Takami, 84460T
- Diaz, A. I., Terlevich, E., & Terlevich, R. 1989, *MNRAS*, 239, 325
- Dicenzo, B. & Levesque, E. M. 2019, *AJ*, 157, 167
- Dorda, R., González-Fernández, C., & Negueruela, I. 2016a, *A&A*, 595, A105
- Dorda, R., Negueruela, I., & González-Fernández, C. 2018, *MNRAS*, 475, 2003
- Dorda, R., Negueruela, I., González-Fernández, C., & Taberner, H. M. 2016b, *A&A*, 592, A16
- Ekström, S., Georgy, C., Eggenberger, P., et al. 2012, *A&A*, 537, A146
- Elias, J. H., Frogel, J. A., & Humphreys, R. M. 1985, *ApJS*, 57, 91
- Fawley, W. M. & Cohen, M. 1974, *ApJ*, 193, 367
- Feltzing, S., Fohlman, M., & Bensby, T. 2007, *A&A*, 467, 665
- Figer, D. F., MacKenty, J. W., Robberto, M., et al. 2006, *ApJ*, 643, 1166
- Gaia Collaboration, Brown, A. G. A., Vallenari, A., et al. 2020, *arXiv e-prints*, arXiv:2012.01533
- Gazak, J. Z., Davies, B., Bastian, N., et al. 2014a, *ApJ*, 787, 142
- Gazak, J. Z., Davies, B., Kudritzki, R., Bergemann, M., & Plez, B. 2014b, *ApJ*, 788, 58
- Gazak, J. Z., Kudritzki, R., Evans, C., et al. 2015, *ApJ*, 805, 182
- Gehrz, R. 1989, in *IAU Symposium*, Vol. 135, *Interstellar Dust*, ed. L. J. Allamandola & A. G. G. M. Tielens, 445
- Ginestet, N., Carquillat, J. M., & Jaschek, C. 1999, *A&AS*, 134, 473
- Gonneau, A., Lyubenova, M., Lançon, A., et al. 2020, *A&A*, 634, A133
- Halliday, I. 1955, *ApJ*, 122, 222
- Hinkle, K., Wallace, L., & Livingston, W. 1995, *PASP*, 107, 1042
- Humphreys, R. M. 1978, *ApJS*, 38, 309
- Humphreys, R. M., Helmel, G., Jones, T. J., & Gordon, M. S. 2020, *AJ*, 160, 145
- Ivanov, V. D., Rieke, M. J., Engelbracht, C. W., et al. 2004, *ApJS*, 151, 387
- Jonsson, J., Launila, O., & Lindgren, B. 1992, *MNRAS*, 258, 49P
- Joyce, R. R., Hinkle, K. H., Wallace, L., Dulick, M., & Lambert, D. L. 1998, *AJ*, 116, 2520
- Jura, M. & Kleinmann, S. G. 1990, *ApJS*, 73, 769
- Keenan, P. C. & McNeil, R. C. 1989, *ApJS*, 71, 245
- Kervella, P., Arenou, F., Mignard, F., & Thévenin, F. 2019, *A&A*, 623, A72
- Kharchenko, N. V., Scholz, R. D., Piskunov, A. E., Röser, S., & Schilbach, E. 2007, *Astronomische Nachrichten*, 328, 889
- Kleinmann, S. G. & Hall, D. N. B. 1986, *ApJS*, 62, 501
- Koornneef, J. 1983, *A&A*, 500, 247
- Lançon, A. & Wood, P. R. 2000, *A&AS*, 146, 217
- Lançon, A., Hauschildt, P. H., Ladjal, D., & Mouhcine, M. 2007, *A&A*, 468, 205
- Lardo, C., Davies, B., Kudritzki, R. P., et al. 2015, *ApJ*, 812, 160
- Levesque, E. M., Massey, P., Olsen, K. A. G., et al. 2005, *ApJ*, 628, 973
- Limongi, M. 2017, *Supernovae from Massive Stars*, ed. A. W. Alsabti & P. Murdin, 513
- López-Corredoira, M., Garzón, F., Beckman, J. E., et al. 1999, *AJ*, 118, 381
- Maíz Apellániz, J., Trigueros Páez, E., Negueruela, I., et al. 2019, *A&A*, 626, A20
- Massey, P., Neugent, K. F., Levesque, E. M., Drout, M. R., & Courteau, S. 2021, *AJ*, 161, 79
- Medhi, B. J., Messina, S., Parihar, P. S., et al. 2007, *A&A*, 469, 713
- Meisel, D. D. 1968, *AJ*, 73, 350
- Messineo, M. & Brown, A. G. A. 2019, *AJ*, 158, 20
- Messineo, M., Habing, H. J., Menten, K. M., et al. 2005, *A&A*, 435, 575
- Messineo, M., Menten, K. M., Churchwell, E., & Habing, H. 2012, *A&A*, 537, A10
- Messineo, M., Zhu, Q., Ivanov, V. D., et al. 2014, *A&A*, 571, A43
- Messineo, M., Zhu, Q., Menten, K. M., et al. 2017, *ApJ*, 836, 65
- Meyer, M. R., Edwards, S., Hinkle, K. H., & Strom, S. E. 1998, *ApJ*, 508, 397
- Moravvej, E., Guinan, E. F., Khosroshahi, H., & Wasatonic, R. 2013, *AJ*, 146, 148
- Morelli, L., Ivanov, V. D., Pizzella, A., et al. 2020, *A&A*, 641, A44
- Nassau, J. J. & Macrae, D. A. 1955, *ApJ*, 121, 32
- Negueruela, I., González-Fernández, C., Marco, A., & Clark, J. S. 2011, *A&A*, 528, A59
- Negueruela, I., González-Fernández, C., Marco, A., Clark, J. S., & Martínez-Núñez, S. 2010, *A&A*, 513, A74
- Negueruela, I., Marco, A., González-Fernández, C., et al. 2012, *A&A*, 547, A15
- Neugent, K. F., Massey, P., Georgy, C., et al. 2020, *ApJ*, 889, 44
- Origlia, L., Moorwood, A. F. M., & Oliva, E. 1993, *A&A*, 280, 536
- Origlia, L., Oliva, E., Sanna, N., et al. 2016, *A&A*, 585, A14
- Park, S., Lee, J.-E., Kang, W., et al. 2018, *The Astrophysical Journal Supplement Series*, 238, 29
- Patrick, L. R., Evans, C. J., Davies, B., et al. 2017, *MNRAS*, 468, 492
- Patrick, L. R., Evans, C. J., Davies, B., et al. 2015, *ApJ*, 803, 14
- Perraud, H. 1961, *Journal des Observateurs*, 44, 247
- Prugniel, P., Vauglin, I., & Koleva, M. 2011, *A&A*, 531, A165
- Ramírez, S. V., Depoy, D. L., Frogel, J. A., Sellgren, K., & Blum, R. D. 1997, *AJ*, 113, 1411
- Rayner, J. T., Cushing, M. C., & Vacca, W. D. 2009, *ApJS*, 185, 289
- Rayner, J. T., Toomey, D. W., Onaka, P. M., et al. 2003, *PASP*, 115, 362
- Reid, M. J., Menten, K. M., Brunthaler, A., et al. 2014, *ApJ*, 783, 130
- Reid, M. J., Menten, K. M., Zheng, X. W., et al. 2009, *ApJ*, 700, 137
- Sharma, S., Hayden, M. R., Bland-Hawthorn, J., et al. 2020, *arXiv e-prints*, arXiv:2011.13818
- Shetye, S., Van Eck, S., Goriely, S., et al. 2020, *A&A*, 635, L6
- Shetye, S., Van Eck, S., Jorissen, A., et al. 2019, in *IAU Symposium*, Vol. 343, *IAU Symposium*, ed. F. Kerschbaum, M. Groenewegen, & H. Olofsson, 69–72
- Skiff, B. A. 2014, *VizieR Online Data Catalog*, B/mk
- Skrutskie, M. F., Cutri, R. M., Stiening, R., et al. 2006, *AJ*, 131, 1163
- Soubiran, C., Le Campion, J.-F., Brouillet, N., & Chemin, L. 2016, *A&A*, 591, A118
- Stevens, D. J., Stassun, K. G., & Gaudi, B. S. 2017, *AJ*, 154, 259
- Stock, S., Reffert, S., & Quirrenbach, A. 2018, *A&A*, 616, A33
- Straniero, O., Chieffi, A., & Limongi, M. 1997, *ApJ*, 490, 425
- Taberner, H. M., Dorda, R., Negueruela, I., & González-Fernández, C. 2018, *MNRAS*, 476, 3106
- Taniguchi, D., Matsunaga, N., Jian, M., et al. 2020, *arXiv e-prints*, arXiv:2012.07856
- Thorsbro, B., Ryde, N., Rich, R. M., et al. 2020, *ApJ*, 894, 26
- Villaume, A., Conroy, C., Johnson, B., et al. 2017, *ApJS*, 230, 23
- Vollmann, K. & Eversberg, T. 2006, *Astronomische Nachrichten*, 327, 862
- Wilson, R. E. & Joy, A. H. 1950, *ApJ*, 111, 221
- Wright, N. J., Barlow, M. J., Greimel, R., et al. 2009, *MNRAS*, 400, 1413
- Yamashita, Y. 1967, *Publications of the Dominion Astrophysical Observatory Victoria*, 13, 47

We are thankful to the IRTF staff for helping us with the observations. MM is thankful to Dr. Anthony Brown for the catalog of RSGs. **We thank the anonymous referee for her/his careful reading and constructive comments.** This work has made use of data from the European Space Agency (ESA) mission *Gaia* (<http://www.cosmos.esa.int/gaia>), processed by the *Gaia* Data Processing and Analysis Consortium (DPAC, <http://www.cosmos.esa.int/web/gaia/dpac/consortium>). Funding for the DPAC has been provided by national in-

stitutions, in particular the institutions participating in the *Gaia* Multilateral Agreement. This publication makes use of data products from the Two Micron All Sky Survey, which is a joint project of the University of Massachusetts and the Infrared Processing and Analysis Center/California Institute of Technology, funded by the National Aeronautics and Space Administration and the National Science Foundation. This research has made use of the VizieR catalog access tool, CDS, Strasbourg, France, and SIMBAD database. This research has made use of NASA's

Astrophysics Data System Bibliographic Services. R.P.K. acknowledges support by the Munich Excellence Cluster Origins Funded by the Deutsche Forschungsgemeinschaft (DFG, German Research Foundation) under the German Excellence Strategy EXC-2094 390783311. This work was partially supported by the National Natural Science Foundation of China (NSFC-11773025, 11421303), and USTC grant KY2030000054.

**Table A**  
Parameters of known RSGs collected from literature.

| 2MASS            | Alias      | [Fe/H] | Ref. | log(g) | Ref. | log(g)*   |
|------------------|------------|--------|------|--------|------|-----------|
| 00511639+6148196 | HD 4817    | 0.0    | 7    | 0.6    | 8    | 0.3± 0.2  |
| 01195361+5818308 | HD 236697  | 0.0    | 9    | 0.4    | 10   | 0.1± 0.1  |
| 01333316+6133296 | BD+60 265  | 0.2    | 1    | ..     | 0    | -0.0± 0.0 |
| 01431110+4831002 | HD 10465   | -0.1   | 1    | ..     | 0    | -0.0± 0.1 |
| 02214241+5751460 | HD 14404   | 0.1    | 2    | 0.2    | 3    | -0.1± 0.1 |
| 02220690+5636148 | HD 14469   | 0.1    | 2    | -0.1   | 10   | -0.1± 0.1 |
| 02222428+5706340 | HD 14488   | ..     | 0    | -0.3   | 10   | -0.2± 0.1 |
| 05271022+2955158 | HD 35601   | 0.1    | 1    | 0.2    | 10   | 0.0± 0.0  |
| 05551028+0724255 | HD 39801   | 0.2    | 1    | 0.4    | 4    | 0.0± 0.0  |
| 06121911+2254305 | HD 042543  | 0.2    | 1    | 0.0    | 10   | -0.1± 0.2 |
| 06224788+2759118 | HD 44391   | 0.0    | 4    | 1.1    | 4    | 0.7± 0.6  |
| 06300229+0755159 | HD 045829  | 0.1    | 1    | 0.8    | 5    | 0.4± 0.3  |
| 07410262-3140591 | CD-31 4916 | -0.2   | 1    | 0.2    | 4    | -0.0± 0.0 |
| 07473853-1559263 | HD 63302   | 0.0    | 1    | 0.2    | 4    | -0.1± 0.2 |
| 18082651-1833078 | HD 165782  | 0.2    | 6    | 0.9    | 6    | 0.1± 0.0  |
| 18375890-0652321 | RSGC1-F13  | -0.2   | 3    | ..     | 0    | 0.0± 0.0  |
| 18392036-0601426 | RSGC2-14   | -0.2   | 3    | ..     | 0    | 0.0± 0.0  |
| 19392533+1634163 | HD 185622  | 0.1    | 1    | ..     | 0    | 0.2± 0.1  |
| 19461557+1036475 | gam Aql    | -0.2   | 7    | 1.5    | 8    | 0.5± 0.4  |
| 19481183+2245463 | HD 187238  | 0.0    | 1    | 0.7    | 8    | 0.3± 0.2  |
| 19501193+2455240 | HD 339034  | 0.3    | 1    | ..     | 0    | -0.3± 0.4 |
| 20185752+3900151 | BD+38 4003 | -0.2   | 8    | 0.2    | 8    | 0.3± 0.3  |
| 20285059+3958543 | RW Cyg     | 0.3    | 1    | ..     | 0    | -0.2± 0.3 |
| 21433045+5846480 | HD 206936  | 0.1    | 7    | ..     | 0    | 0.0± 0.0  |
| 22230701+5557477 | HD 212466  | 0.2    | 1    | ..     | 0    | -0.7± 0.8 |
| 22562598+4944006 | HD 216946  | -0.2   | 1    | 0.5    | 8    | 0.3± 0.2  |

**References:** 1=Davies et al. (2010), 2=Davies et al. (2009), 3=Gazak et al. (2015), 4= Arentsen et al. (2019), 5=Prugniel et al. (2011), 6=Stevens et al. (2017), 7=Anderson & Francis (2012), 8=Soubiran et al. (2016), 9=Ivanov et al. (2004), 10=Dicenzo & Levesque (2019).

\* **log(g) are estimated** with the tracks of Bertelli et al. (2009).

## APPENDIX

### A. RELATION BETWEEN LUMINOSITIES, TEMPERATURES, AND GRAVITIES OF RSG STARS.

The fundamental theoretical quantities of stellar astrophysics are the effective temperature  $T_{\text{eff}}$ , the gravity  $\log(g)$ , the luminosity  $\log(L/L_{\odot})$ , and the initial chemical composition.

The  $T_{\text{eff}}$  values can be estimated using dereddened colors and/or spectral types (assuming a temperature scale). We have used *HK* atomic lines (Ca I, Na I, Si I, Mg I) as well as the CO band heads at  $1.62 \mu\text{m}$  to estimate the  $T_{\text{eff}}$  values (Sect. 6). Luminosities have been estimated by photometric measurements and by assuming a distance (e.g. the Gaia parallactic distances). For Galactic RSGs, which span a small range of metallicity (mostly between  $-0.5$  and  $+0.5$ ), the stellar gravity can be estimated quite straightforwardly by establishing a relation between  $T_{\text{eff}}$  or  $\log(L/L_{\odot})$  and  $\log(g)$  with stellar tracks.

We used the RSG portions of the stellar tracks from 8 to  $25 M_{\odot}$  with solar metallicity by Bertelli et al. (2009) and by Chieffi & Limongi (2013). In Fig. A1, the  $\log(g)$  values are plotted versus the  $\log(L/L_{\odot})$  values, as well as versus the  $T_{\text{eff}}$  values. During the RSG phase, while the star ascends the red part of the track, there is one linear relation between  $\log(L/L_{\odot})$  and  $\log(g)$  for any given initial mass. By increasing the initial mass we shift this relation (segment) to a higher luminosity and lower gravity. By simply considering the average locations of these segments for stars from 8 to  $20 M_{\odot}$ , we derived an average relation between the  $\log(L/L_{\odot})$  (estimated with observable quantities) and  $\log(g)$  (the theoretical quantity to be measured). Similar equations are derived from the  $\log(g)$  values and the  $T_{\text{eff}}$  values.

The obtained  $\log(g)$  values from Bertelli et al. (2009) are accurate to within 0.5 dex (the span expected due to different initial masses), and independent of the knowledge of the initial mass of the star (which is not an observable quantity). These are the derived equations:

$$\log g = 4.91(\pm 0.13) - 1.04(\pm 0.03) \times \log L;$$

$$\log g = -6.61(\pm 0.08) + 1.86(\pm 0.02) \times \log T_{\text{eff}}.$$

We found gravity estimates from stellar spectra for 17 RSGs included in this work (Table A). The equations from the Bertelli et al. (2009) well describe the observed data points; when using the average relations inferred from the tracks of Bertelli et al. (2009), we found a general offset of  $-0.28$  and a  $\sigma$  of 0.28 dex.

The theoretical relations ( $\log(g)$ ,  $T_{\text{eff}}$ ,  $\log(L/L_{\odot})$ ) depend on the assumed code, for example, on the opacities, the mixing length scale  $\alpha$ , the inclusion of overshooting. Tracks become cooler for larger value of  $\alpha$  (e.g., Chun et al. 2018). Bertelli et al. (2009) adopted  $\alpha = 1.68$ , while Chieffi & Limongi (2013) use  $\alpha=2.3$  (Straniero et al. 1997).

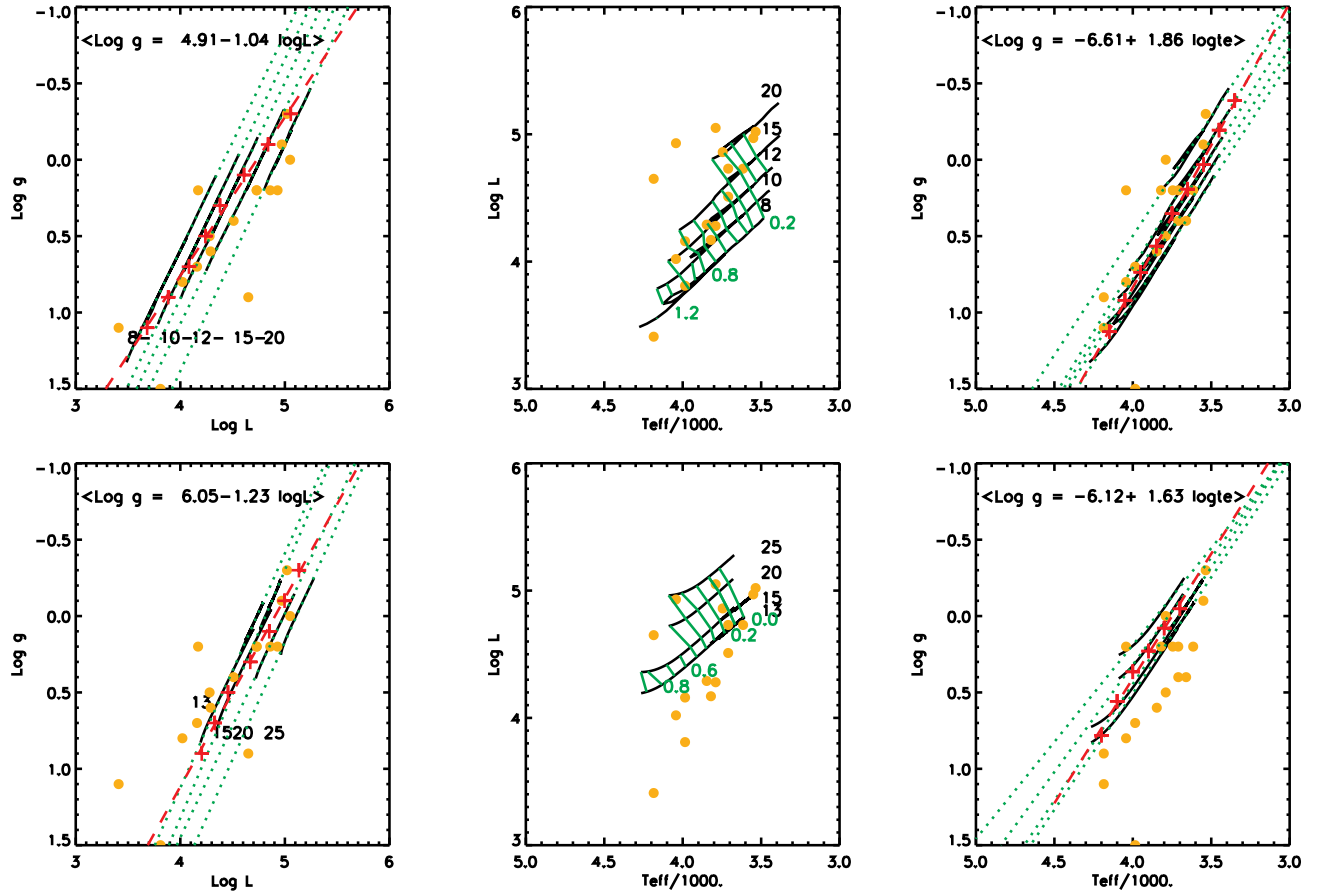


**Figure A.** 1. *Top Panels:* For stars of 8, 10, 12, 15, and 20  $M_{\odot}$ , the RSG portions of the stellar tracks with solar metallicity by Bertelli et al. (2009) were extracted. *In the top left panel,* their  $\log g$  values are plotted vs. the  $\log L$  values (black segments). They can be approximated with linear curves (green dotted lines). The red crosses represent the average locus per bin of luminosities and the red dashed line is their fit. Orange filled circles mark parameters of RSGs collected from literature and listed in Table A. *In the top middle panel,* The  $\log L$  values are plotted vs. the  $T_{\text{eff}}$  values. In black the stellar track segments, and in green the connecting segments of points at constant gravity. Orange filled circles are data points from Table A. *In the top right panel,* the  $\log g$  values are plotted vs. the  $T_{\text{eff}}$  values (black segments). They are approximated with linear curves (green dotted lines). The red crosses represent the average locus per bin of temperatures, which are fitted with the red dashed line. Orange filled circles are data points from Table A. *Bottom panels:* For stars of 13, 15, 20, and 25  $M_{\odot}$ , the RSG portions of the stellar tracks with solar metallicity by Chieffi & Limongi (2013) were extracted. Plotted diagrams are as above.

## B. MOLECULAR DIAGNOSTICS FOR LATE-TYPES AND CONTAMINATION OF O-RICH MIRA AGB

Infrared spectra of RSGs may display broad features in absorption due to molecular absorption, for example from TiO, VO, ZrO, H<sub>2</sub>O, and CN molecules. A list of identified molecules in the SpeX spectra is provided in the catalog of Rayner et al. (2009). For the VO bands, we used the list of Joyce et al. (1998). An illustrative work is also that of Alvarez et al. (2000), where the authors describe the occurrence of molecular features with stellar types, chemistry type, and envelope types. Here we only annotate molecular diagnostics that are useful for spectral classification and luminosity classification of RSGs.

- *In our sample, there is no contamination of C-rich AGB stars.*  
C-rich AGBs are easily discernible at infrared wavelengths because of their strong CN, C<sub>2</sub>, and CO lines. For example, typically the [J10] (CN band head) values of RSGs range from 1-4 Å, while ranges from 5 to 10 Å in C-rich stars (Rayner et al. 2009). There are no C-rich stars among our targets.
- *Contamination: O-rich Mira AGBs and S-type AGBs*  
The [Mg I, 1.71] versus [CO, 2.29] diagram effectively distinguishes RSGs from normal giant stars. However, it maintains large contamination of O-rich Mira AGBs and hybrid S-type AGB stars, which are stars that go from O- to C-rich composition (Wright et al. 2009; Joyce et al. 1998; Rayner et al. 2009). Mira AGBs have very broad [CO, 2.29], but they do not obey the [CO]-temperature relation (Blum et al. 2003). O-rich Mira AGBs are usually identified by the strength of the water absorption.

The SpeX spectra with their large baseline provide us with further additional molecular considerations useful for distinguishing RSGs and O-rich Mira stars and S-type AGBs.

- Independently of their temperature, the atmospheres of RSGs are rich in CN molecules; for example, strong CN band

heads appear around  $0.91 \mu\text{m}$  and  $1.09 \mu\text{m}$ .

The four CN band heads at  $1.0875 \mu\text{m}$ ,  $1.0929 \mu\text{m}$ ,  $1.0966 \mu\text{m}$ , and  $1.0999 \mu\text{m}$  appear distinguishable in the spectra of any RSG – also in the spectra of the rare M7.5I 2MASS J22543171+6049388 (MY-Cep) – with band heads significantly stronger than those in O-rich Mira stars ([J8+J9+J10]), as shown in Fig. 5 and already described in Sec. 4.2.

- Absorption bands of water vapor are a strong feature of O-rich Mira stars, but are weak and rare in RSGs. A list of the spectral regions with water absorption is given by Rayner et al. (2009). We measured the strength of the water absorption in the region 1.75-2.05 as done by Blum et al. (2003) and Messineo et al. (2017), and the results are listed in Table C. In the spectrum of RSGC1-F13 (M2 I) we measured 0.%, in 2MASS J22543171+6049388 (MY-Cep, M7.5 I) 5.7%, in 2MASS J05551028+0724255/HD 39801 (M2 I) 5.9%, and in 2MASS J22495897+6017567/PER406 (K2 I) 7.3%. However, in the spectra of 2MASS J18345133–0713162 ( $\text{Sp}_{\text{combi}} = \text{M5.5}$ ) and 2MASS J18345840–0714247 ( $\text{Sp}_{\text{combi}} = \text{M5}$ ), we measure 10.4%, 18.2%, which are particularly high values, typically found in Mira AGBs.

Spectra of late-type stars with continuum absorption higher than 6.6% should be considered as possible O-rich Mira AGBs and are marked with a flag in Tables 1, 2, and 3. A small percentage (6.5%) of spectra of known RSGs shows water absorption.

A steep absorption, likely due to water (Jonsson et al. 1992; Joyce et al. 1998), also appears at  $\approx 1.34 \mu\text{m}$  in the spectra of MY-Cep (M7.5I), 2MASS J18375890–0652321/RSGC1-F13 (M2I), and 2MASS J22495897+6017567/PER406 (K1I).

- TiO bands ( $0.82\text{-}0.86$ ,  $0.88\text{-}0.90$ ,  $0.92\text{-}0.94 \mu\text{m}$ ) are seen in the spectra of M-type RSGs, as well as in those of O-rich Mira AGB stars.

The TiO band heads at  $0.88\text{-}0.90 \mu\text{m}$  start to be visible in the spectra of M0-type RSGs, and are strong in stars later than M2.5. TiO at  $0.8859 \mu\text{m}$  is often used to infer spectral types of M-type RSGs (e.g. Dorda et al. 2016a).

In late-M RSGs TiO bands at  $0.92\text{-}0.94 \mu\text{m}$  are usually weak, the dominant feature in this range being the ZrO absorption. On the contrary, TiO bands at  $0.92\text{-}0.94 \mu\text{m}$  are strong in Mira AGB stars, as shown in Figs. B1 and B2.

Sharp TiO band heads at  $1.103$  and  $1.116 \mu\text{m}$  appear in the spectra of all but one O-rich Mira AGB star (Rayner et al. 2009; Joyce et al. 1998). In the late Mira AGB (IRAS 14303-1042, M8-9III), the TiO feature is no longer visible because there is strong water absorption. On the contrary, TiO band heads around  $1.1 \mu\text{m}$  do not appear in the spectra of known RSGs.

- Continuum absorption due to ZrO at  $0.930\text{-}0.936 \mu\text{m}$  appears to be visible in the spectra of all RSG with spectral type M3 and is strong in M5-M6, as shown in Fig. B.

The spectrum of 2MASS J17143885+1423253/HD 156014 (M5 Ib-II AGB) shows strong ZrO band heads.<sup>9</sup>

Unfortunately, absorption by ZrO also characterizes the spectra of all S-type AGBs (Rayner et al. 2009; Wright et al. 2009; Joyce et al. 1998). However, in contrast to S-type stars, RSGs with late spectral types (M3-M7.5) have ZrO along with strong TiO at  $0.82\text{-}0.86$ ,  $0.88\text{-}0.90 \mu\text{m}$ , as shown in Fig. B.

- If the ZrO and TiO regions are not covered, the spectra of S-type AGB stars and RSGs can be distinguished by using the ratios of their CO band heads at  $1.57 \text{ \AA}$  and Si I absorption lines at  $1.59 \text{ \AA}$ . Indeed, the Si I line at  $1.59 \mu\text{m}$  is visibly weaker in S-type AGBs than in RSGs (see Fig. 6). High-resolution studies of Si I lines can open new frontiers in Galactic spectroscopy as shown by Thorsbro et al. (2020). The J2, J4, and J8 lines have similar behavior to the Si I line at  $1.59 \mu\text{m}$ .
- VO absorption at  $1.046\text{-}1.056 \mu\text{m}$  with a strong round signature of the continuum occurs in the spectra of O-rich Mira AGBs, as well as in the spectrum of 2MASS J18375890–0652321/RSGC1-F13 (M2I), 2MASS J18451939–0324483/RSGC3-S6 (M4.5 I). More typically, in the spectra of known RSGs with spectral type M3 or later, a weak VO mark appears (as a change of the stellar continuum slope).

### C. SPECTRAL ATLAS AND INDICES

The figures with the obtained spectra are available only electronically (Figs. C1, C2, C3, C4). Only the wavelength range where the signal-to-noise of the stellar trace is above 50 is plotted.

In Table C we list the measured EWs of the 72 stars in our observational program and 24 from the IRTF libraries of Rayner et al. (2009) and Villaume et al. (2017). Only indices relative to spectral segments with a signal to noise larger than 50 are retained.

<sup>9</sup> The star, however, falls in the giant sequence in the [Mg I, 1.71] versus [CO, 2.29] diagram and in the [J8+J9+J10] versus [CO, 2.29]. Its TiO bands are displayed in Fig. B.

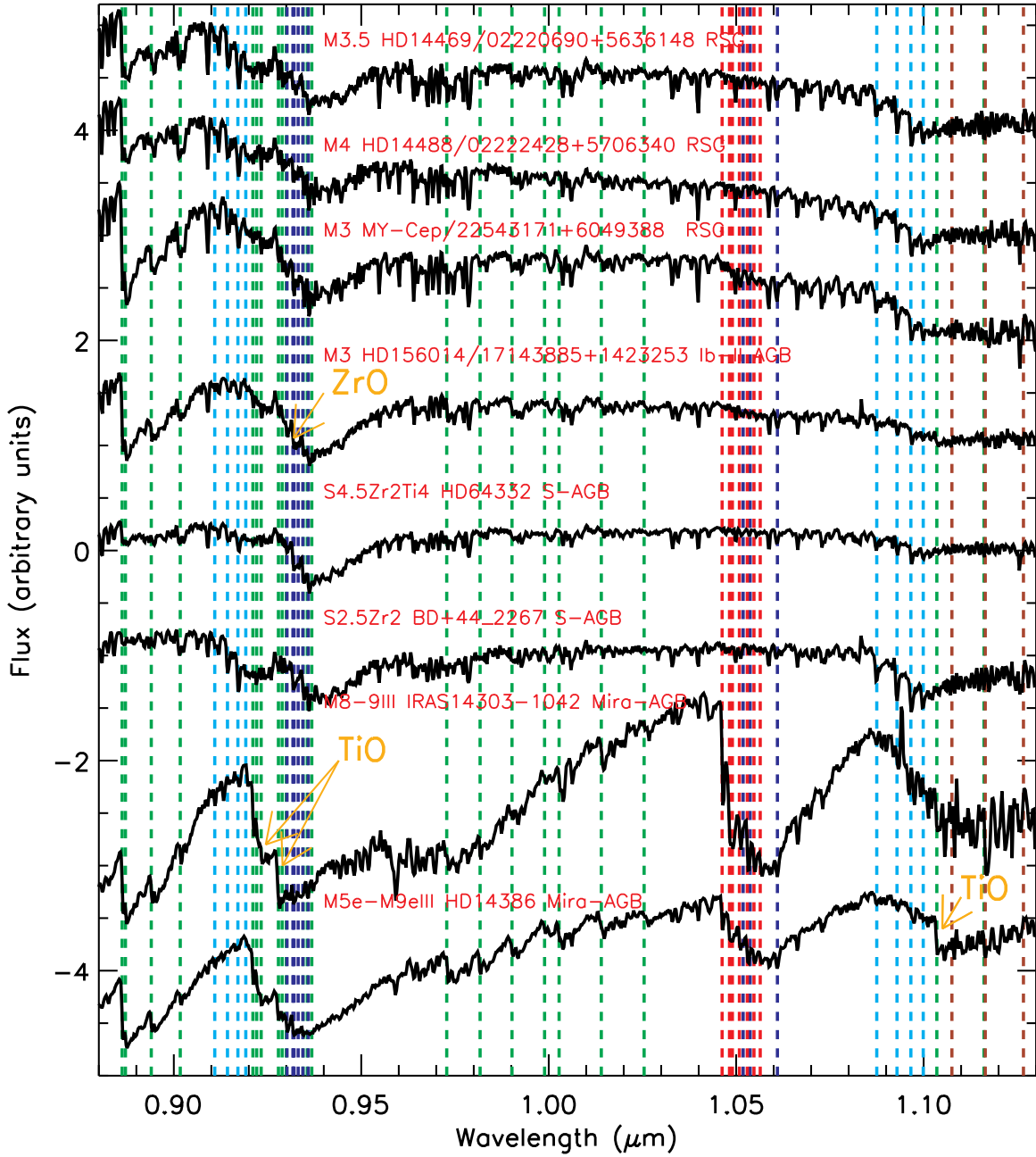


**Figure B. 1.** Examples of spectra taken from the IRTF library from 0.88 to 1.2  $\mu\text{m}$  showing the TiO band heads (green vertical lines), CN band heads (cyan vertical lines), and ZrO band heads (blue vertical lines), VO band heads (in red). The source names, spectral types, and classes are annotated above each spectrum. For RSGs, our spectral types from *H*-band and *K*-band and those from optical literature are marked, as in Table 1. ZrO band heads are evident in late-type RSGs and S-type AGBs (see orange arrow), but not in O-rich Miras. TiO band heads are strong in Miras (see orange arrow).



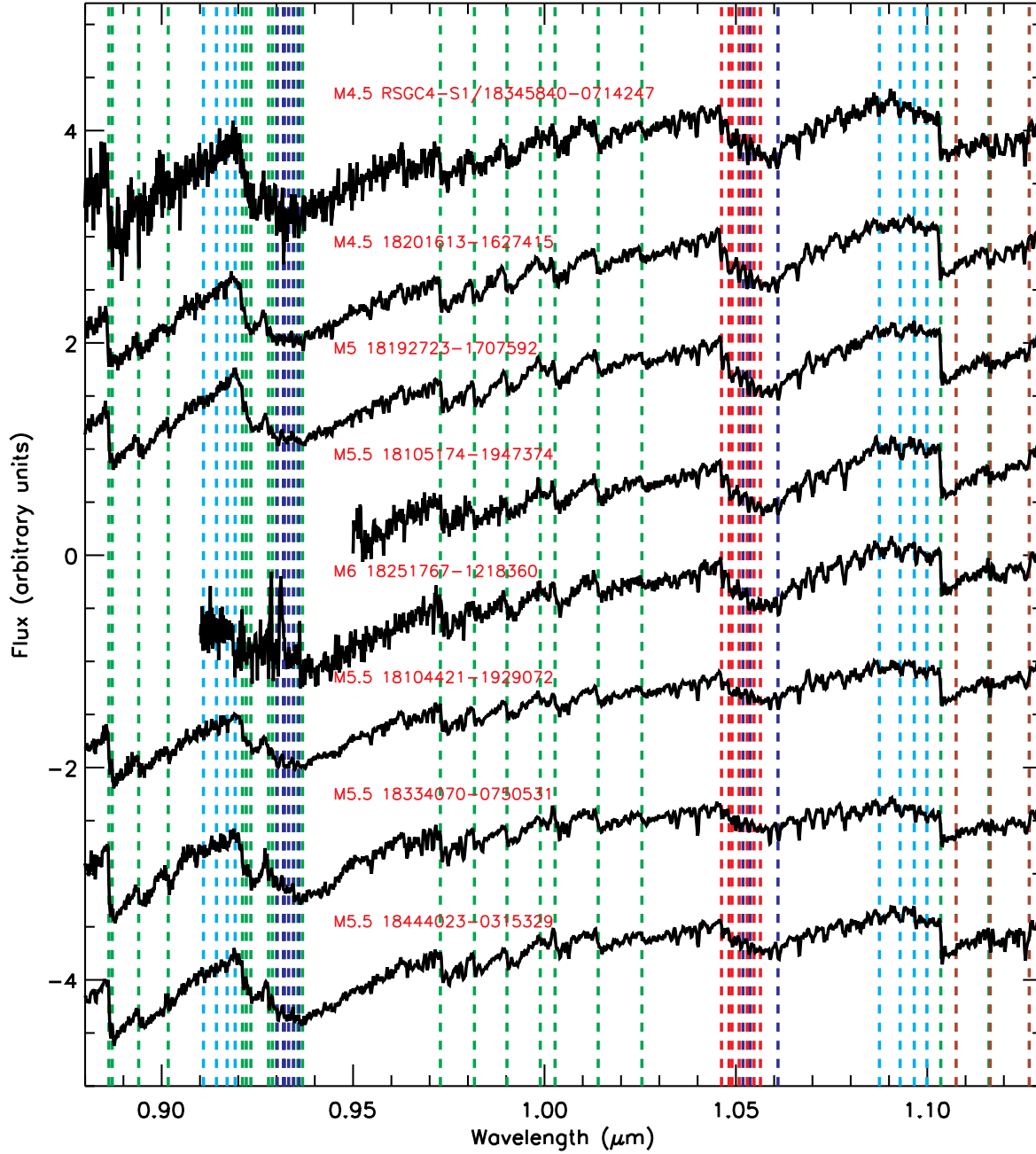


**Figure B. 2.** Spectrum from 0.88 to 1.2  $\mu\text{m}$  of 2MASS J18345840-0714247 from Table 1 and similar spectra of targets from Table 2. All but 2MASS J18104421-1929072, 2MASS J18334070-0750531, and 2MASS J18444023-0315329 have water absorption. These spectra resemble those of O-rich Mira AGBs. Vertical lines mark molecular band heads. TiO band heads are in green, CN band heads in cyan, ZrO band heads in blue, and the VO band heads in red. The source names and spectral types are annotated above each spectrum. The spectral types are those adopted in Table 1.

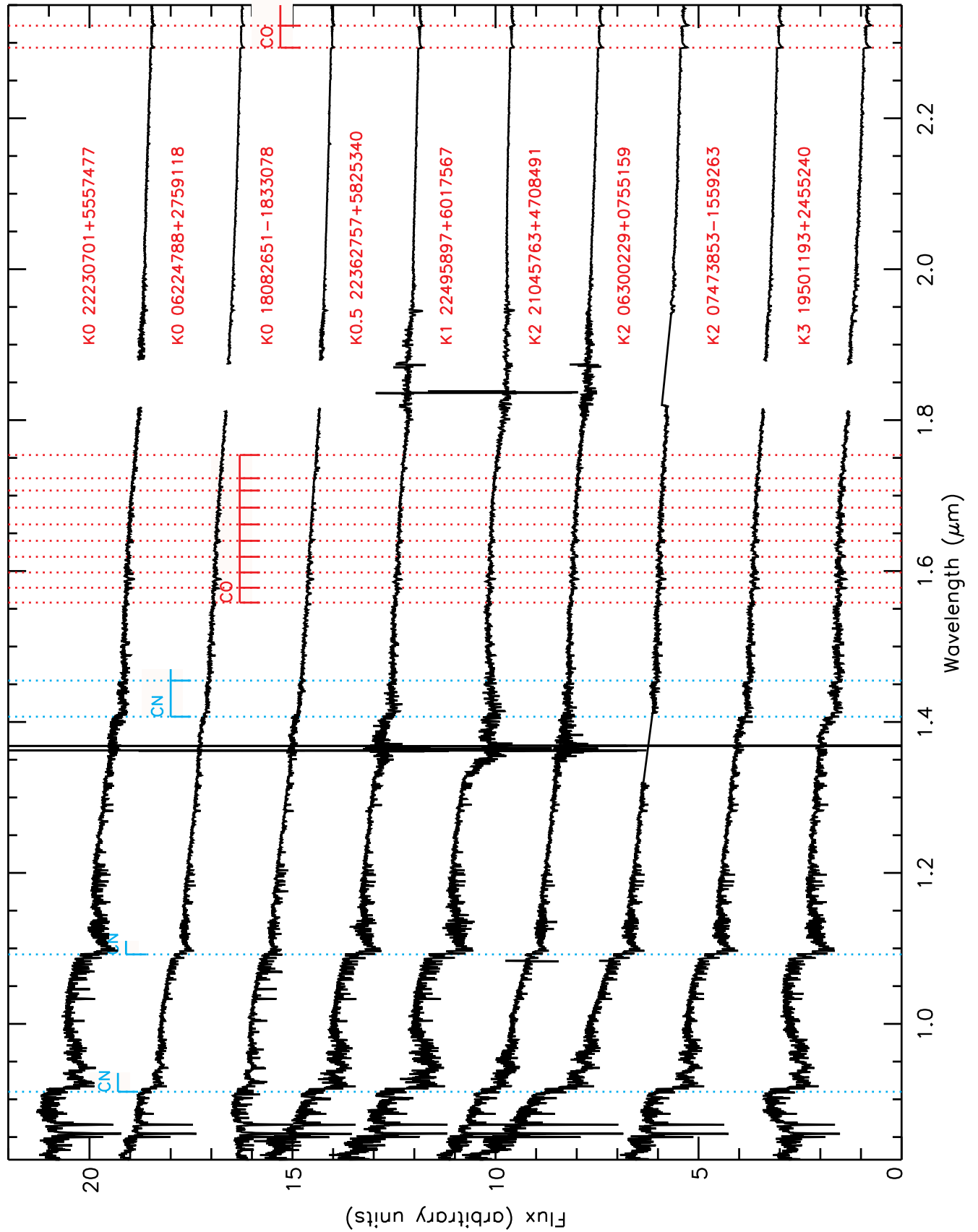


**Figure C. 1.** IRTF spectra of known RSGs from Table 1. 2MASS J17143885+1423253/HD 156014/ $\alpha$  Her (M5 Ib-II, AGB) is also plotted. The spectra are sorted by adopted spectral type.

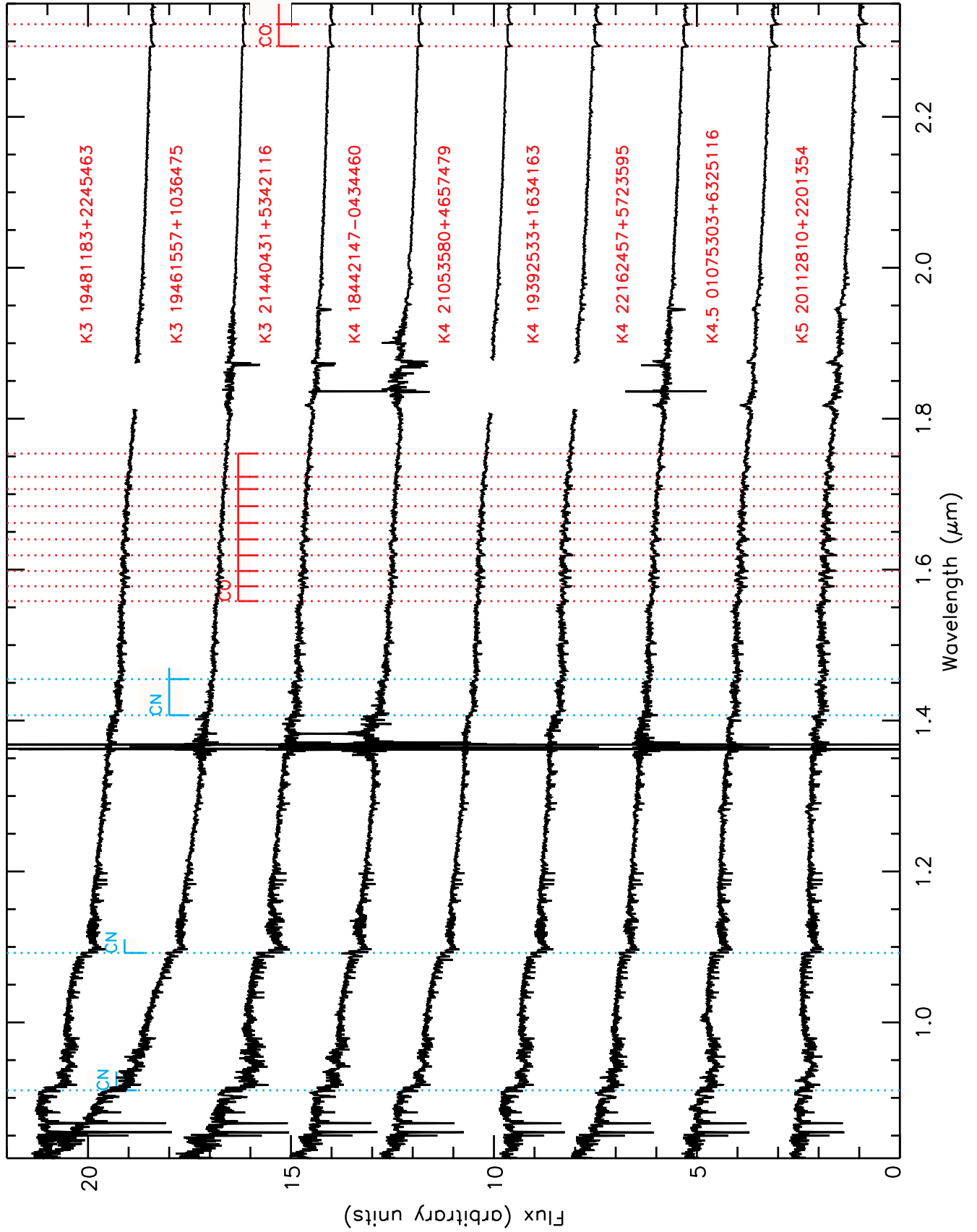


Figure C. Continuation of Fig. C 1. IRTF spectra of known RSGs.

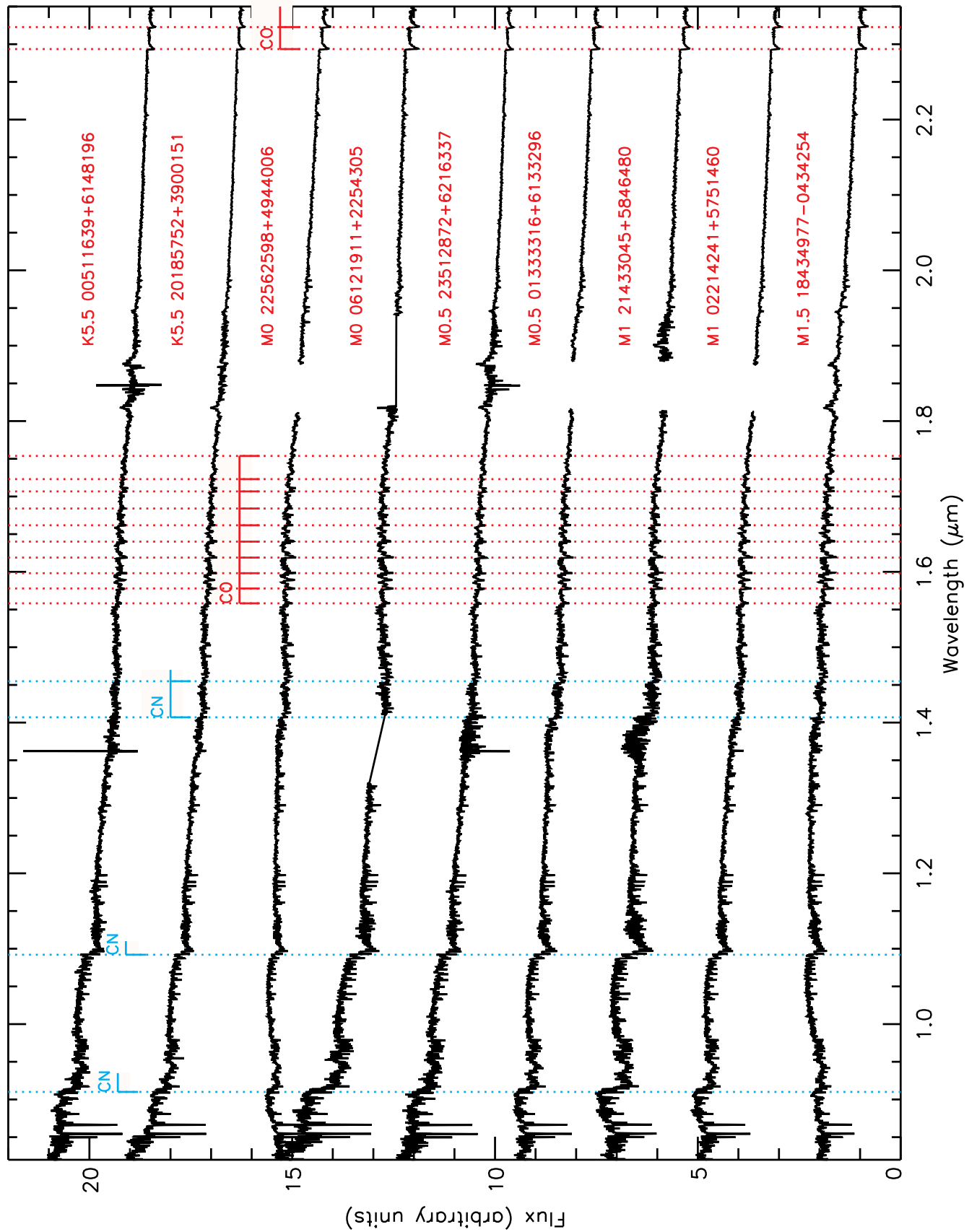


Figure C. Continuation of Fig. C 1. IRTF spectra of known RSGs.

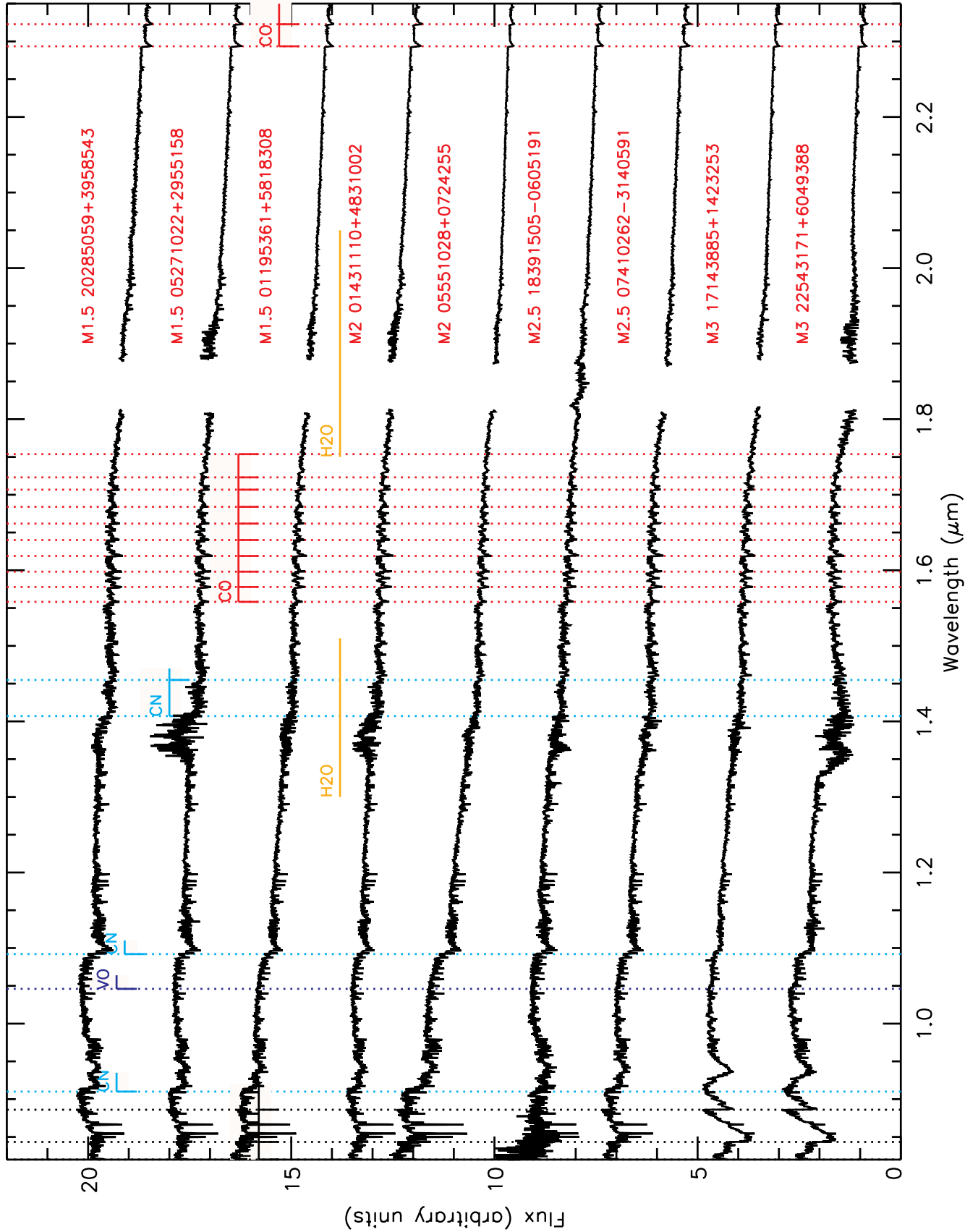


Figure C. Continuation of Fig. C 1. IRTF spectra of known RSGs.

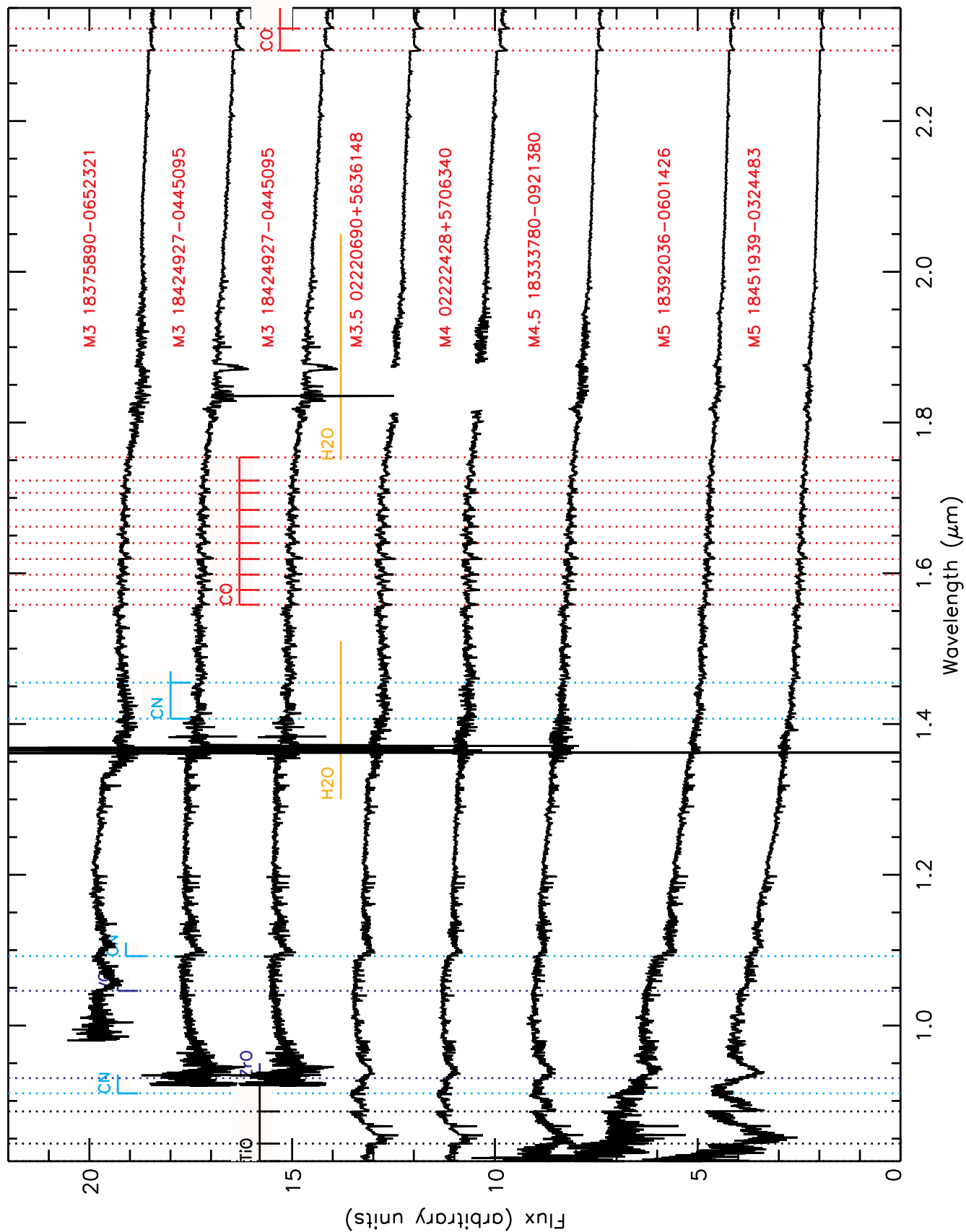
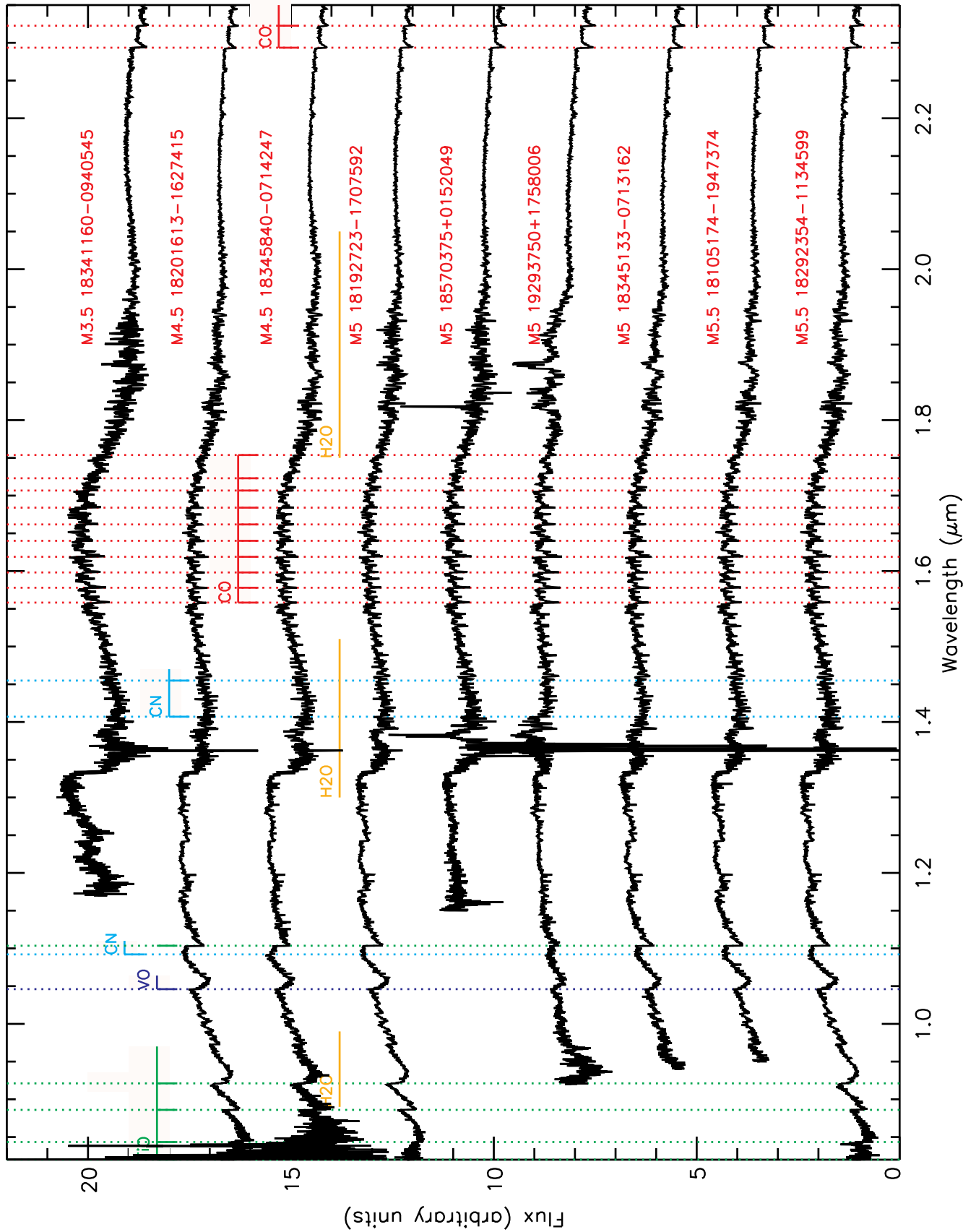


Figure C. Continuation of Fig. C 1. IRTF spectra of known RSGs.



**Figure C.** 2. IRTF spectra where the measured water absorption was found above 6%. 13 from Table 2 and two from Table 1 (2MASS J18345133-0713162 and 2MASS J18345840-0714247). The spectra are sorted by adopted spectral type.

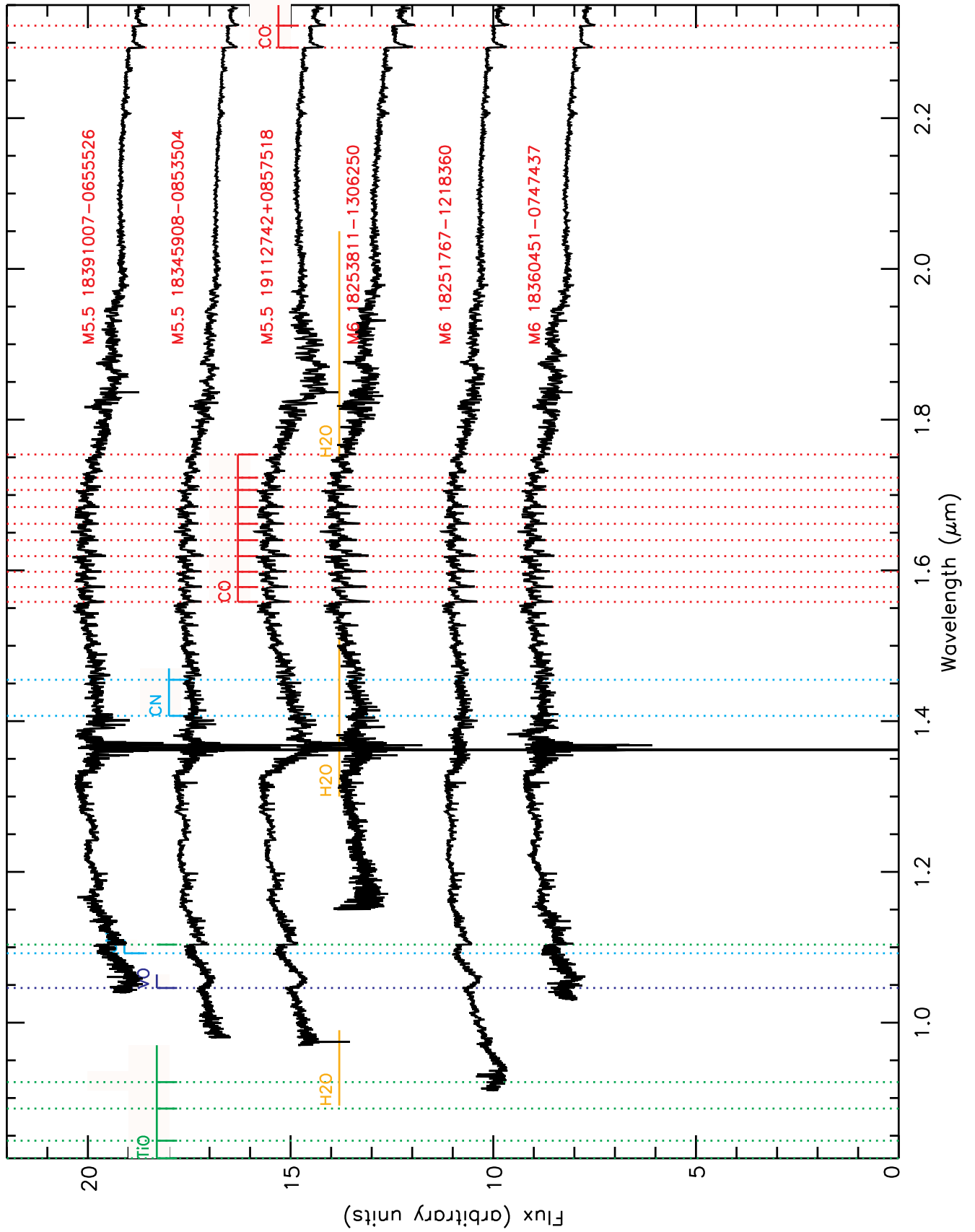


Figure C. Continuation of Fig. C 2. Spectra with water absorption.



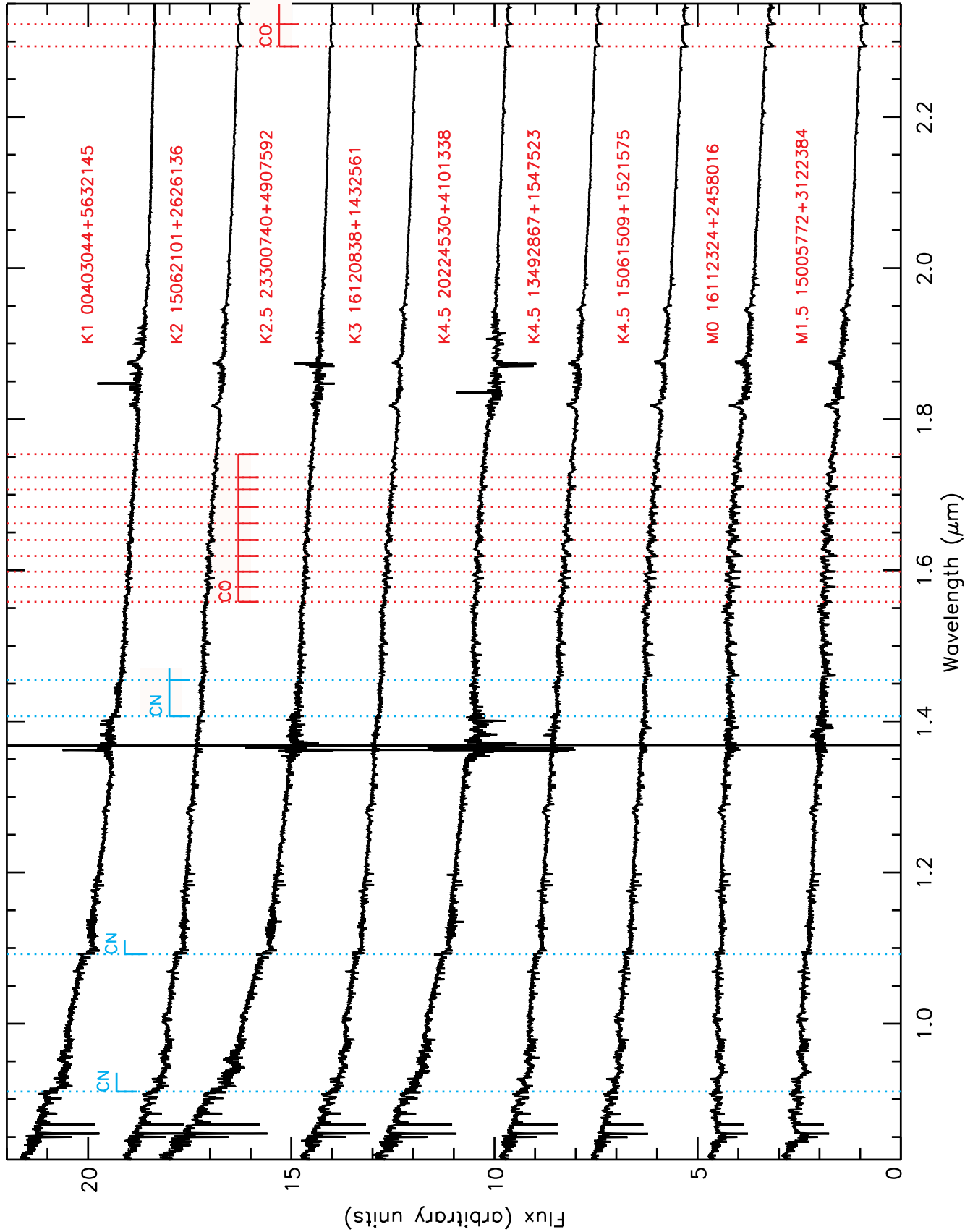
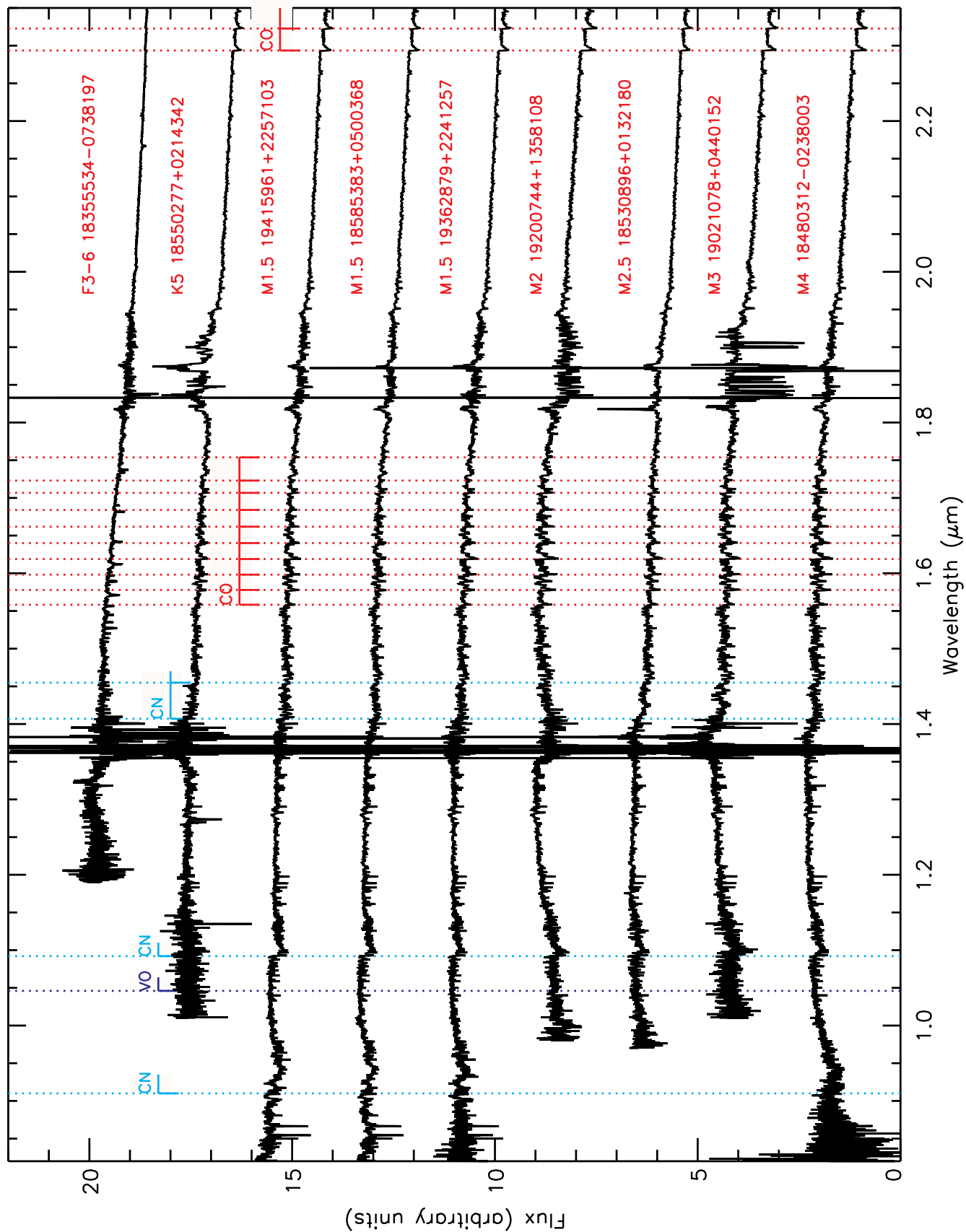


Figure C. 3. IRTF spectra of giant stars from Table 3. The spectra are sorted by adopted spectral type.



**Figure C. 4.** IRTF spectra of observed unknown targets with  $\text{ind}_{\text{H}_2\text{O}}$  smaller than 6% from Table 2. The spectra are sorted by adopted spectral type

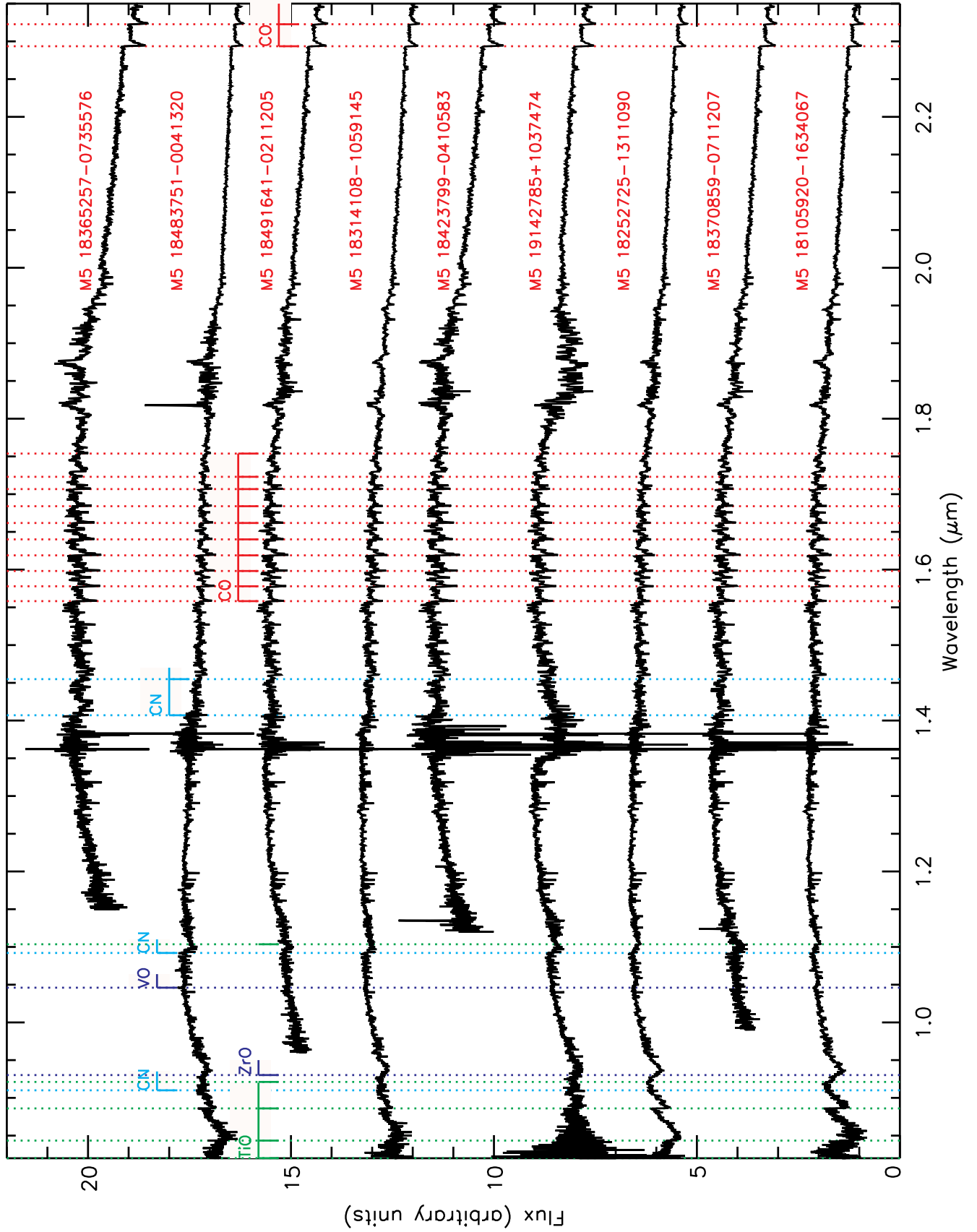


Figure C. Continuation of Fig. C 4 (new targets).

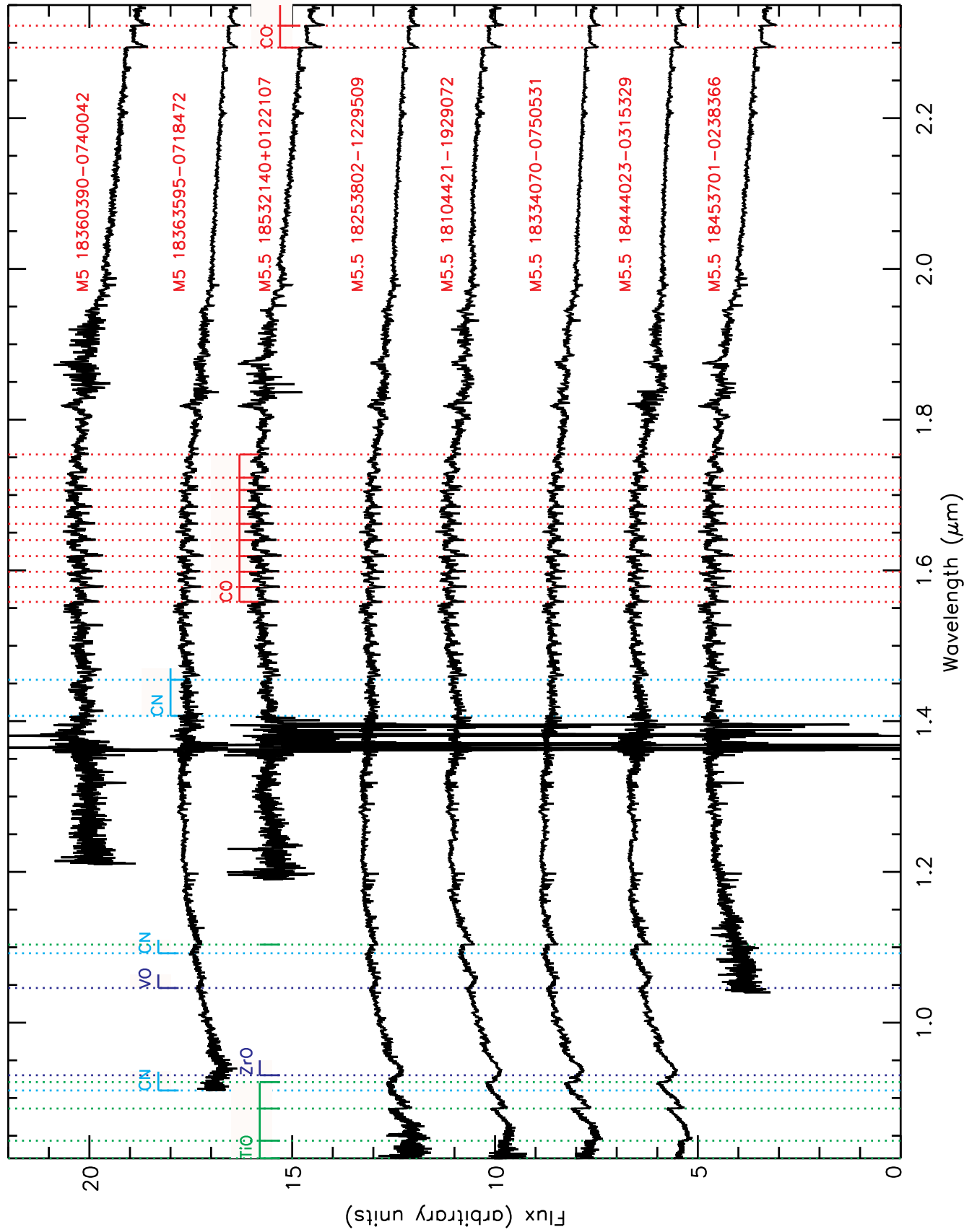


Figure C. Continuation of Fig. C 4 (new targets).

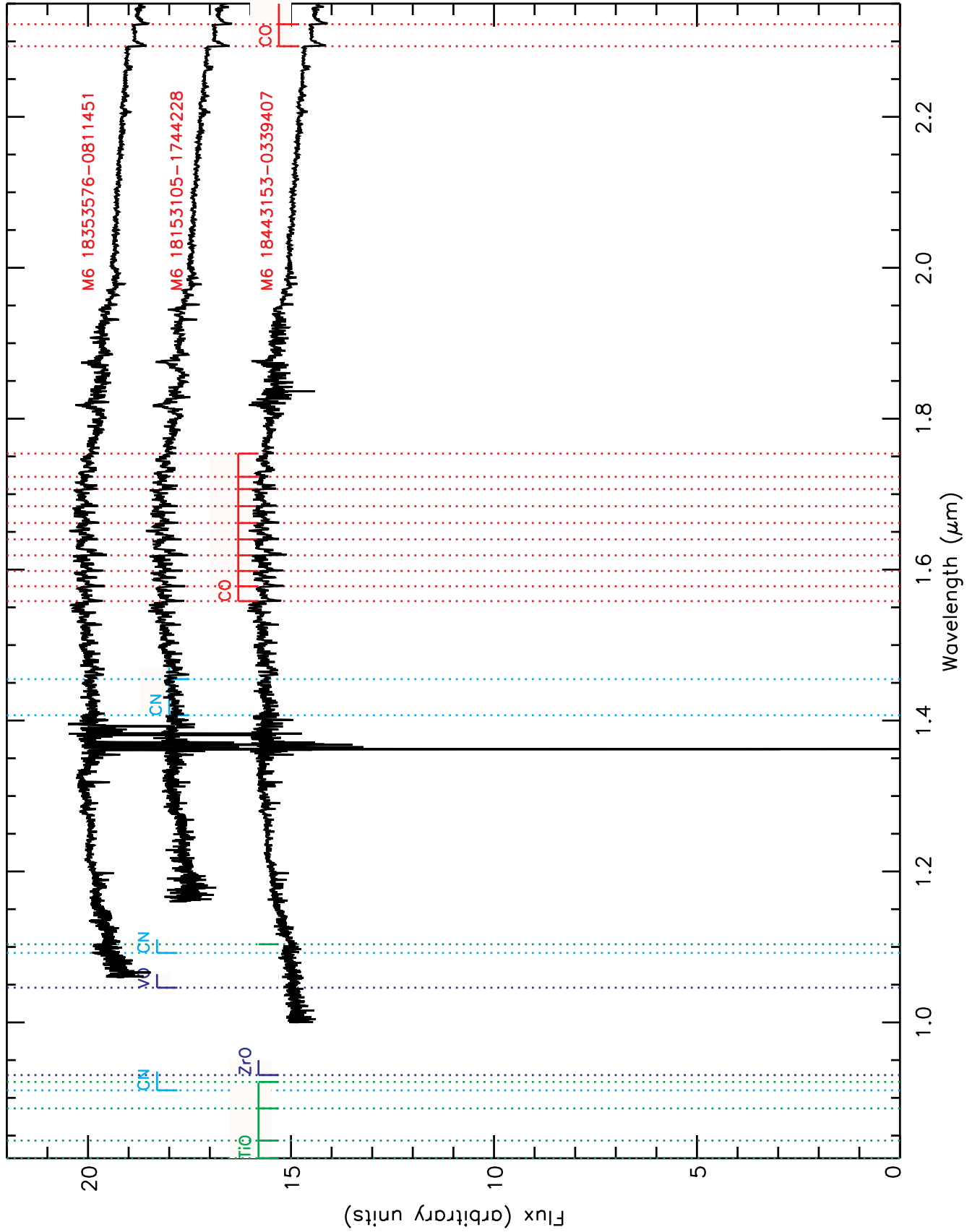


Figure C. Continuation of Fig. C 4 (new targets).



INFRARED SPECTRAL INDICES FOR COLD STARS

Table C
Continuation of Table C.

Table with 13 columns: ID, Date-obs, [J10] [Å], [J11] [Å], [J12] [Å], [J13] [Å], [J14] [Å], [J15] [Å], [J16] [Å], [J17] [Å], [J18] [Å], [J19] [Å], [J20] [Å], [J21] [Å], [J22] [Å]. Each cell contains a numerical value with error bars.

